Nanoscale Studies of Energy Band Gaps and Band Offsets in Compound Semiconductor Heterostructures

by

Alexander S. Chang

A dissertation submitted in partial fulfillment
of the requirements for the degree of
Doctor of Philosophy
(Materials Science and Engineering)
in The University of Michigan
2016

Doctoral Committee:

Professor Rachel S. Goldman, Chair
Professor Roy Clarke
Associate Professor Emmanouil Kioupakis
Professor Çağlıyan Kurdak

Acknowledgements

First of all, I would like to thank Professor Goldman, my thesis advisor, for her support, teaching, and guidance throughout my graduate studies at the University of Michigan. I would also like to thank Professor Roy Clarke, Professor Çağlıyan Kurdak, and Professor Emmanouil Kioupakis for their valuable comments and discussions.

I would also like to thank my fellow group members, especially Jenna Walrath, Yen-Hsiang Lin, Eric Zech, and Chris Greenhill, who I have spent a majority of my time together in the STM lab. I am also thankful for their valuable comments and discussions.

Furthermore, I would like to acknowledge my collaborators, TaeWan Kim in Professor Luke Mawst's group at University of Wisconsin, Thomas Frost and Arnab Hazari in Professor Bhattacharya's group at the University of Michigan, and Brian McGuigan in Professor Harley T. Johnson's group at the University of Illinois.

Supports from the National Science Foundation through the Materials Research Science and Engineering Center (MRSEC) at the University of Wisconsin, Grant No. DMR-1121288 and at the University of Michigan, under grant No. DMR-1120923. are gratefully acknowledged.

Finally, I would like to thank my twin brother Andrew Chang and my parents for their love and support, which have enabled the completion of my thesis study.

Table of Contents

Acknowledgements ii

List of Tables vii

List of Figures viii

List of Appendices xviii

Abstract xix

Chapter 1 Introduction 1

1.1 Overview 1

1.2 Examination of Structural and Electronic Properties of Materials 3

1.3 Type I and Type II Band Alignments 5

1.4 Dissertation Organization 6

1.5 References 10

Chapter 2 Experimental Procedures 17

2.1 Overview 17

2.2 Molecular Beam Epitaxy 17

2.3 Metalorganic Vapour Phase Epitaxy 18

2.4 High Resolution X-ray Diffraction 18

2.5 Atom Probe Tomography (APT) 20

2.5.1 APT Sample Tip Preparation Procedure 20

2.5.2 Voltage and Laser modes of APT 22

2.6 Cross-sectional Scanning Tunneling Microscopy (XSTM) 23
2.6.1 Scanning Tunneling Microscopy Overview 24
2.6.2 Sample Polishing 24
2.6.3 Sample Scribing 25
2.6.4 STM Tip Preparation 27
2.6.5 UHV Sample Preparation 27
2.6.6 Heterostructure Design 29
2.7 Variable-Separation Scanning Tunneling Spectroscopy (VS-STS) 30
2.8 References 36
Chapter 3 Influence of Sb Incorporation on the InGaAs(Sb)N/GaAs Band Alignment 38
3.1 Overview 38
3.2 Background 39
3.3 Growth of InGaAs(Sb)N Quantum Well Structures 40
3.4 Characterization of InGaAs(Sb)N Quantum Well Structures 41
3.4.1 Experimental Details 41
3.4.2 HRXRD and RADS 42
3.4.3 XSTM and SIMS of InGaAs(Sb)N 43
3.4.4 STS of InGaAs(Sb)N Layers 45
3.5 Conclusions 47
3.6 References 55
Chapter 4 Influence of Strain on InGaN/GaN Quantum Dot Formation and Properties 57
4.1 Overview 57
4.2 Background 58

4.3 Experimental Details 60
4.4 HRXRD data on InGaN/GaN QDs 62
4.5 Influence of Starting Substrate on Dot Dimensions, Density 63
4.6 Influence of Starting Substrate on Band Gap 64
4.7 Band Alignment of InGaN/GaN QDs 66
4.8 Conclusions 67
4.9 References 77
Chapter 5 Influence of Strain and Dislocation on the GaSb/GaAs Band Offsets 80
5.1 Overview 80
5.2 Background 81
5.3 Type I and Type II GaSb/GaAs Interfaces: Predictions and Power-Dependent PL 82
5.4 Experimental Methods 85
5.4.1 MBE Growth 85
5.4.2 XSTM, XTEM, and APT on GaSb/GaAs Band Alignment 86
5.5 Influence of Strain and Dislocations on GaSb/GaAs Quantum Dots 87
5.5.1 GaSb/GaAs QDs Band Alignment near Misfit Dislocations 87
5.5.2 IMF and SK GaSb/GaAs QDs Band Alignment 88
5.6 Conclusions 93
5.7 References 105
Chapter 6 Summary and Suggestions for Future Work 109
6.1 Summary 109
6.1.1 Influence of Sb Incorporation on InGaAs(Sb)N/GaAs Band Alignment 109

6.1.2 Influence of Substrate on InGaN/GaN Quantum Dot Formation and Properties 110

6.1.3 Influence of Strain, Dislocation, and Dislocation Charging on the GaSb/GaAs Band Alignment 111

6.2 Suggestions for Future Work 112

6.2.1 High Resolution XTEM of GaSb/GaAs Quantum Dots 112

6.2.2 XSTM on Multi-layer InGaN/GaN QDs 113

6.2.3 Si Dopant and Indium Distribution within InAs QDs 114

6.3 References 120

Appendices 122

List of Tables

Table 4.1: Table summarizing reported band gap energies of InGaN quantum wells (QWs) and quantum dots (QDs) of various x_{In}.[15-23] Photoluminescence is denoted as PL. Variations in the InGaN QD band gap energies for similar indium mole fractions and QD dimension have been reported. In general, the InGaN QDs grown on free-standing GaN substrates had smaller band gap energies compared to those grown on GaN/sapphire.……...69

Table C.1: Material parameters of the GaAs and GaSb used for the computational work in Chapter 5.[7-12]……148

Table C.2: Material parameters of the Semiconductor compounds used in RADS.[13].....149

Table C.3: Material parameters of the Semiconductor compounds used for STS analysis.[13-16]……..…….149

Table E.1: Material parameters of GaAs, GaSb, and InAs used for the 1D Poisson-Schrödinger calculation.[17-19]…….……..……153

Table F.1: InGaAs(Sb)N /GaAs quantum well samples……..155

Table F.2: InGaN /GaN quantum dot XSTM sample cleavage history……...156

Table F.3: InGaN /GaN quantum dot plan-view STM samples…….……..156

Table F.4: GaSb /GaAs quantum dot XSTM samples …….……...157

List of Figures

Fig. 1.1: Calculated band offsets relative to the Fermi energy levels of unstrained semiconductors using the electronic transition level of hydrogen in semiconductors.[38,39] The solid lines represent the valence and conduction band edges and the dashed lines represent the Fermi energy level. The stabilized Fermi energy level energies are indicated as (a) red lines or (b) filled circles. The opened circles in (b) correspond to the Fermi energy level on pinned semiconductor surfaces……8

Fig. 1.2: Schematic diagrams of a (a) type I and (b) type II band alignments. The conduction and valence band edges are labeled as ECB and EVB, respectively. For a type I band alignment, conduction and valence band edges of semiconductor B are lower in energy than those of semiconductor A. For a type II band alignment, the conduction and valence edges of semiconductor C are lower and higher in energy than those of semiconductor A, respectively..……..……..9

Fig. 2.1: Schematic of atom probe tomography (APT). The laser or voltage pulses are applied to the conical section of the sample, i.e. APT tip, such that semiconductor nanostructures in the APT tip are evaporated. The ionized atoms are accelerated to the position-sensitive detector and the time of flight is recorded. The collection of ionized atoms can be reconstructed in 3D to reveal the atomic structure of the nanostructures……31

Fig. 2.2: Scanning electron microscopy images of the (a)-(d) lift out procedure and (e)-(h) the tip shaping procedures. 5 (a) Pt protection layer is deposited on the surface to avoid ion beam damages. (b) A sharp needle is attached to the sample wedge with Pt deposition, and the wedge shaped sample is being lifted out. (c)-(d) Wedge shaped sample is mounted on a Si post. (e)-(h) While the sample stage is tilted to 52^{o}, tip shaping procedure is performed with focused ion beam with various voltage and current settings. The interface between the sample and Pt protection layer is indicated with an arrow in each images. ..……32

Fig. 2.3: (a) XSTM topographical image of InGaN dots in a GaN matrix. Schematics of the tunneling process between a tip and a sample under positive sample bias are shown.[11] The electrons tunnel from the tip into the energy levels above the Fermi level (E_F) of either (b) InN or (c) GaN. Since there are more states available to tunnel in InGaN than GaN, the InGaN layers will appear brighter in a constant-current STM image.[6]……..…….33

Fig. 2.4: Diagram showing the orientations of the (001)-oriented III-V samples.[11] Samples with lengths larger than 12 mm and widths of approximately 1-2 mm were prepared by making a scribe mark 7 mm away from one of the edge. For samples with length from 10 to 12 mm, the scribe mark was made 5 mm away from one of the edge. For all cases, the scribe mark length was 1/3 of the sample width.[6]……...34

Fig. 2.5: Schematic of an ideal cleaved surface as seen from the telescope.[11] Observing through the telescope, the exposed cleaved surface is usually rough near the scribe mark, containing parallel fracture lines. On the opposite end of the cleaved surface, away from

the scribe mark, the surface is usually free of the fracture lines. STM tips are approached to regions far away from these fracture marks. Representative tip positions are indicated by filled circles.[6]…..…….…35

Fig. 3.1: (a) Proposed InGaAsSbN based laser heterostructucre.[13] (b) The subcell efficiency is predicted based on different band gap values assumed for the InGaAsSbN subcell. A highest subcell efficiency is predicted for InGaAsSbN layers with a band gap of approximately 1 eV....……...……48

Fig. 3.2: Band anti-crossing model and the predicted band structure at (a)-(b) InGaAsN/InGaAs and (d)-(e) GaAsSbN/GaAsN interfaces. (b), (d) The red and blue lines corresponds to the nitrogen and antimony impurity state, which leads to band splitting of conduction and valence band edges, respectively. Incorporation of (c) N and (d) Sb leads to a decrease in the effective band gap energy due to the conduction and valence band splitting, respectively.[15,16] ……49

Fig. 3.3: Cross-section of the InGaAs(Sb)N heterostructure grown by TaeWan Kim at the University of Wisconsin. AlAs/GaAs superlattices would serve as a marker for locating the InGaAs(Sb)N layers during an XSTM experiment……..……50

Fig. 3.4: Plots of (004) ω-2θ scans of the (a) InGaAsN and (b) InGaAsSbN based structures, in comparison with RADS simulations, with and without the InGaAs(Sb)N layers. The measured XRD spectra are plotted as solid lines, labeled “data” for both (a) InGaAsN and (b) InGaAsSbN-based structures. RADS simulations in the absence of the (a) InGaAsN and (b) InGaAsSbN layers are plotted as dotted lines, labeled “AlAs/GaAs only.” Finally, plots of RADS simulations, using the concentration profiles shown in Fig. 3.5 (b) and (d), are plotted as dashed lines, labeled “simulations” in (a) and (b).

Further details of the RADS simulations are discussed in Appendix D……..……51

Fig. 3.5: (a) and (c) are large-scale cross-sectional XSTM images, and (b) and (d) are the compositional profiles used as input for RADS simulations of the GaAs/InGaAsN/GaAs and GaAs/ InGaAsSbN/GaAs structures, shown in Figs. 3.4 (a) and (b), respectively. The large-scale XSTM images were acquired at sample bias voltages of (a) -2.1 V and (c) +2.1 V, and the gray-scale ranges displayed are (a) 25Å and (c) 6 Å. The composition profiles include (b) indium fractions of x_{In} = 0.01, 0.02, and 0.06 and nitrogen fractions of x_N = 0.02 and 0.025 within the InGaAsN layer and (d) indium fractions of x_{In} = 0.04, nitrogen fractions of x_N = 0.015, and antimony fractions of x_{Sb} = 0.01 within the InGaAsSbN layer……..…….52

Fig. 3.6: (a) and (c) are large-scale cross-sectional XSTM images, and (b) and (d) are the secondary ion mass spectroscopy data of the GaAs/InGaAsN/GaAs and GaAs/ InGaAsSbN/GaAs structures, shown in Figs. 3.4 (a) and (b), respectively. The large-scale XSTM images were acquired at sample bias voltages of (a) -2.1 V and (c) +2.1 V, and the gray-scale ranges displayed are (a) 25Å and (c) 6 Å. In gradient in the SIMS profile is observed for both (b) InGaAsN and (d) InGaAsSbN layers is revealed…..…53

Fig. 3.7: Plots of normalized conductance versus sample bias voltage, collected from GaAs (solid line) and InGaAs(Sb)N (dotted line), for the (a) InGaAsN/GaAs, and (b) as-grown and (c) annealed InGaAsNSb/GaAs structures. The sample voltages correspond to the energy relative to the Fermi level. The effective band edges of InGaAsN are lower than those of GaAs, revealing a “nested” Type I band alignment. For both as-grown and

annealed InGaAsSbN, the conduction (valence) band edges are higher (lower) than those of GaAs, revealing a “staggered” Type II band alignment.....54

Fig. 4.1: Schematic band structure of GaN/InGaN/GaN interfaces (a) with and (b) without piezoelectric polarization. For InGaN/GaN interfaces with strong polarization, spatial separation of electron and hole wave functions are expected. For InGaN/GaN interfaces with no polarization, the electron and hole wave functions are spatially overlapped, leading to an increase in electron-hole recombination rate.[5]……73

Fig. 4.2: Calculated island positions and sizes in multi-layer QDs. Unit L represents the QD spacer thickness. The number of QD layers are indicated within the figure. Heights of vertical lines represent the relative island volumes. Sequences begin with (a) closely spaced islands and (b) widely spaced islands.[6] The strain field from the buried QDs reduces the local misfit at the surface, leading to vertical stacking of QDs and an increase in the regularity of the spacing between the QDs.……...……..……71

Fig. 4.3: Reported InGaN QD density as a function of number of QD stacks. Conflicting trends of a constant or an increase in QD density with increasing number of QD SLs have been reported, depending on the starting substrate.[12-16] Increase in the QD density with increasing number of QD stacks agrees with the Tersoff’s model, which predicts dot nucleation due to strain field from the buried QDs.[12,15,16] On the other hand, few experimental reports present a constant QD density with increasing number of QD stacks, most likely due to QD nucleation by other sources, such as phase separation of indium and residual stress from threading dislocations.[13,14]…….72

Fig. 4.4: Diffraction intensity plotted as a function of Δω for (a) QD-GaN, (b) QD-GaN/sapphire, and (c) multi-QD-GaN/sapphire collected near the GaN (002) reflection

during X-ray diffraction measurements, in comparison with RADS simulations. For all cases, the measured XRD spectra are plotted as black line, labeled “data”. RADS simulations are labeled as “sim”, respectively…….……..73

Fig. 4.5: Large-scale STM images of (a) QD-GaN, (b) QD-GaN/sapphire, and (c) multi-QD-GaN/sapphire. The images were acquired at a sample bias voltage of -3.5 V; the greyscale ranges displayed are (a) 15 nm, (b) 8 nm, and (c) 5 nm, respectively……..……..……74

Fig. 4.6: Plots of normalized conductance versus sample bias voltage, collected from GaN and around InGaN QDs from (a) QD-GaN, (b) QD-GaN/sapphire, and (c) multi-QD-GaN/sapphire. STS reveals effective band gaps of 3.4 eV for GaN, which agrees well with the reported value. The effective band gaps at the center of the QD are significantly smaller than the band gaps at the edge of the QD. (b) For QD-GaN/sapphire, STS reveals an effective band gap of 1.2 eV around the InN QDs due to quantum confinement…….…...……...……75

Fig. 4.7: (a) schematic and (b) STM image of QD-GaN surface. Plots of valence and conduction band edges versus (c) lateral and (d) vertical distances across the InGaN nanostructure, as indicated within the figure, are plotted as red and black dots, respectively. Across the lateral direction of the InGaN nanostructure, the valence band edge is similar to that of GaN, while a decreasing gradient in the conduction band edge towards the center of the dot is observed. In addition, a significant change in the conduction band edge across the vertical direction of the InGaN QD is observed, suggesting the nanostructure to be two adjacent large InGaN QDs……..……...……...76

Fig. 5.1: Plots of the calculated band edges (solid lines), ground state energies of confined carriers (dashed lines), and corresponding wave functions (dotted lines) for partial (blue) and full (green) dopant ionization. (a) For type I band alignment, the upward shift of electron and hole ground state energies does not alter the energy separation between the ground state energies. (b) For type II band alignment, the upward (downward) shift of electron (hole) ground state energy leads to an increase in energy separation between the electron and hole ground states. Band edge calculations were carried out by the author using a 1D Poisson/Schrödinger solver.[17-19]……94

Fig. 5.2: Logarithm of the PL energy shift vs. the logarithm of the laser power for various GaSb/GaAs quantum structures.[17-31] The solid green, solid blue, and opened black data points correspond to GaAsSb quantum wells, strained GaSb quantum dots, and unstrained GaSb quantum dots, respectively. Furthermore, band bending, capacitive charging, and both band bending and capacitive charging are claimed to be the cause of the power dependent PL blue-shift, which are plotted as circles, squares, and triangles, respectively……..…..95

Fig. 5.3: Bright-field <110> zone-axis TEM images, which contain GaSb/GaAs QD SLs grown on (a) Sb-terminated and (b) As-terminated GaAs surfaces; [220] 2-beam bright field TEM images of clustered GaSb QDs grown on (c) Sb-terminated and (d) As-terminated GaAs surfaces.[36] The high magnification insets reveal semi-coherent clusters in the vicinity of the GaSb QDs. Misfit dislocations ("M"), coherent clusters ("C"), and semi-coherent ("S") clusters are indicated in (c) and (d)……..……96

Fig. 5.4: High-magnification XSTM topographic images of GaSb/GaAs QD SLs grown on (a) Sb-terminated and (b) As-terminated GaAs surfaces.[36] The images were obtained at

a sample bias voltage of ±2.4 V; the greyscale ranges displayed are (a) 0.4nm, and (b) 0.5 nm.……..……..97

Fig. 5.5: Plots of normalized conductance versus sample bias voltage, collected from the GaAs (solid line), the GaSb/GaAs QD edge (dashed line), and the GaSb/GaAs QD core (dotted line), grown on (a) Sb-terminated and (b) As-terminated GaAs surfaces. The sample voltages correspond to the energy relative to the Fermi level.[36]……98

Fig. 5.6: XSTM image of (a) SK and (b) IMF GaSb QD samples. The SK QDs were not nucleated and only Sb wetting layers are present. The IMF QDs are clearly observed near the line labeled as 3ML GaSb……99

Fig. 5.7: (a) cross-sectional scanning tunneling microscopy (XSTM) image, acquired in the vicinity of a GaSb/GaAs quantum dot (QD) using a constant tunneling current of 0.25 nA and a sample bias -2.6 V. The tip height color-scale range displayed is 1.23 nm, with bright and dark regions corresponding to GaSb QD and the GaAs matrix, respectively. Pixels with tip height up to 4.9 ± 0.5 Å above the GaAs background in (a) are displayed in (b) with bright and dark-gray scales corresponding to increasing GaSb fractions, xSb. The removal of atomic planes in the GaSb QDs is represented by the dislocation core symbols in (b), and the associated in-plane hydrostatic strain contours are shown in (c). The net in-plane hydrostatic strain contours, including both the misfit and dislocation-induced strain, are shown in (d). The red dotted lines in (b) indicate paths along which band structure profiles will be presented……..……100

Fig. 5.8: Band profiles for the cases of (a) unstrained, (b) lattice mismatch strain, (c) dislocation strain, (d) dislocation charging of sf=0.1, and (e) dislocation charging of

sf=0.4 across paths 1 – 4 from Fig. 1(b). The black dotted lines denote volume-averaged band energies across the QD., with the GaAs matrix band energies at 1.43 eV (CB) and 0 eV (VB) as reference levels. For (a) the unstrained case, a weak type-I alignment is observed for paths across the QD center (paths 1 and 2), with smaller band-edge variations across paths above and below the QD (paths 3 and 4). In (b), with the introduction of misfit strain, the CB along paths 1 and 2 is raised, leading to type II band alignment; meanwhile, negligible changes to both CB and VB are observed along paths 3 and 4. In (c), with the inclusion of both misfit and dislocation strain, the band alignment is again type I across paths 1 and 2, with minimal change along paths 3 and 4. In (d), for sf=0.1, the CB and VB values are similar to those in (c). Finally, in (e), for sf=0.4, both CB and VB are lowered across paths 1-4, resulting in type II band alignments……...101

Fig. 5.9: (a) Reconstruction of APT data and (b) the interpolated 3D composition profile of IMF GaSb QDs. Isosurface plots detailing Sb concentrations > 20% are indicated as yellow spheres……..…102

Fig. 5.10: (a),(c) Conduction band and (b),(d) Valence band charge density isosurfaces (Blue) detailing electron/hole confinement for IMF and SK grown sample, respectively. The isosurface for Sb concentration >20% is shown for reference (Yellow). Spatial separation of electrons and holes suggest a type II band alignment for SK QDs……..…103

Fig. 5.11: PL measurement on (a) SK and (b) IMF GaSb QD samples. For the SK GaSb QD sample, only photoemission from GaAs was observed. For the IMF GaSb QD sample, GaSb peaks were observed at 1.35 eV….....104

Fig. 6.1: Cross-sectional scanning tunneling microscopy (XSTM) image of In0.24Ga0.76N / GaN QDs, grown in (a) Vecco Gen 2 and (b) Veeco Gen 930 by T. Frost in Prof. Bhattacharya's group at the University of Michigan. …..……116

Fig. 6.2: STS measurement on InGaN QD and GaN matrix. The STS data suggests a band gap of 3.4 eV for GaN and 1.5 eV for InGaN QD. …….…….....…117

Fig. 6.3: (a) Reconstructed atom probe tomography data of InAs/GaAs QDs collected in Laser mode. Indium atoms are plotted as blue dots and isosurfaces of xIn > 0.1 are plotted as yellow dots. A cross-section of the reconstructed data of (a) top, (b) middle, and (c) bottom InAs QD layer. Isosurfaces of x_{In} > 0.1, plotted as yellow dots, reveal the InAs QDs of ~ 6 nm diameter……..……..……..118

Fig. 6.4: Reconstructed atom probe tomography data of InAs/GaAs QDs collected in Voltage mode. Indium atoms are plotted as blue dots and isosurfaces of x_{In} > 0.1 are plotted as yellow dots…….……..119

List of Appendices

Appendix A Scanning Tunneling Spectroscopy Data Analysis 123

Appendix B Quantum Dot Size Analysis 146

Appendix C Materials Parameters 148

Appendix D Rocking Curve Analysis by Dynamical Simulation 150

Appendix E Materials Databas for Poisson-Shrodinger Calculations…….....153

Appendix F List of Samples ..……...……..155

Abstract

Nanoscale Studies of Energy Band Gaps and Band Offsets in Compound Semiconductor Heterostructures
by

Alexander S. Chang

Chair: Rachel S. Goldman

Over the past few decades, advances in semiconductor thin film growth lead to the fabrication of semiconductor heterostructures with nanometer-scale structures. For semiconductor heterostructures, carrier confinement or redistribution at semiconductor interfaces can be used to control the electronic and optical properties of the material. Furthermore, the identification of the precise band offsets at semiconductor interfaces is crucially important for the successful development of electronic and optoelectronic devices. However, issues at the interfaces, such as strain or defects, needs to be investigated for precise band tuning of semiconductor heterostructures. In this dissertation, the nanometer-scale structural and electronic properties of InGaAs(Sb)N/GaAs interfaces, InGaN/GaN QDs, and GaSb/GaAs QDs are investigated using a combination of cross-sectional scanning tunneling microscopy (XSTM) and variable separation scanning tunneling spectroscopy (STS).

The influence of Sb incorporation on the InGaAs(Sb)N/GaAs band alignment is investigated. Heterostructures with and without Sb incorporation are grown by MOVPE and cleaved to examine InGaAs(Sb)N QWs cross-sectionally. XSTM and STS reveal 1.2 eV (1.1 eV) effective bandgaps of InGaAs(Sb)N alloys. At the InGaAsN/GaAs (InGaAsSbN/GaAs) interfaces, type II (type I) band offsets are observed, due to strain-

induced splitting of the valence band and the incorporation of Sb. Contrary to literature report of valence band edge tuning by Sb incorporation, the observed Sb-induced variation in the conduction and valence band offsets is significantly larger than predicted values, suggesting the possibility of both the conduction and valence band offset tuning at InGaAs(Sb)N/GaAs interfaces, with minimal Sb incorporation. The band tuning of both conduction and valence band edges with the incorporation of Sb can be used to engineer the band structure with strong confinement of electrons and holes in the InGaAsSbN quantum well layer, which is promising for light emitting applications.

The influence of the growth substrate on InGaN/GaN QD formation and properties is examined. The QD density, dimension, and band gaps are compared for different InGaN QDs on free-standing GaN or GaN/AlN/sapphire substrates. We present different sources using nucleation on different substrates, and discuss their influences on the electronic band structure. Our work suggests that a wide variety of InGaN QD dimension, density, and band structure can be achieved by using different starting substrate and number of layers of InGaN QD stacks. Our work suggests that a wide variety of InGaN QD dimension, density, and band structure can be achieved by varying starting substrate and number of layers of InGaN QD stacks.

Furthermore, the influence of strain and dislocation on the GaSb/GaAs QD band alignment is investigated using both experimental and computational tools. A combination of cross-sectional transmission electron microscopy (XTEM), XSTM, and STS reveals the formation of misfit dislocations and both coherent and semi-coherent clustered QDs, independent of Sb- vs. As-termination of the GaAs surface. STS collected across the GaSb/GaAs QD interfaces reveals type I band offsets. Furthermore, finite element analysis

simulation on GaSb/GaAs QD band alignment reveal that the dislocation and misfit strains in the vicinity of GaSb/GaAs QD interfaces lead to a transition from type I to type II band offsets. Thus, the strong strain dependence of the GaSb/GaAs QDs allows the achievement of both type I and type II band structures within a single heterostructure, providing design flexibility promising for optical device applications.

Chapter 1

Introduction

1.1 Overview

Over the past few decades, advances in semiconductor thin film growth have enabled the fabrication of semiconductor heterostructures of nanometer sizes.[1-26] Using growth techniques such as molecular beam epitaxy (MBE), precise growth of monolayers of semiconductors has become possible.[25-33] Using heterostructures of semiconductors with different band structures, carrier confinement and redistribution at different band alignments influence the electronic properties of the material.[27-33] Additionally, strain fields can be used to influence the structural properties of semiconductor heterostructures, which may enhance their optoelectronic properties.[34-37] Furthermore, the identification of the precise band offsets at semiconductor interfaces is crucially important for the successful development of electronic and optoelectronic devices. For example, shown in Fig. 1.1 are the calculated relative band offsets of unstrained semiconductors using the electronic transition level of hydrogen in semiconductors.[38,39] Since the predicted band offsets are based on the energy levels of hydrogen in unstrained semiconductors, the band offsets at compound semiconductor interfaces in the vicinity of strain fields and defects are not

predicted. Thus, nanoscale studies of the band structure near semiconductor interfaces are necessary for predicting the functionality of semiconductor devices.

Typically, the active regions of heterostructures used in optoelectronic devices are near the interfaces. However, the atomic-scale structural and electronic properties of the interfaces within a given heterostructure are still not very well understood. For example, it has been proposed that long-wavelength lasers can be achieved by growing highly strained InGaAsN or InGaAsSbN layers on GaAs substrates.[40-43] However, the influence of Sb incorporation on the band alignment on InGaAs(Sb)N/GaAs interfaces remains unknown.

Furthermore, strain-induced self-assembled InGaN/GaN quantum dots (QDs) have enabled significant advances in a variety of devices including light emitters and detectors. In the simplest model, InGaN QD nucleation occurs preferentially at positions of local strain minima.[44] For multilayers of QDs, the strain field from the buried QDs reduces the local misfit at the surface, leading to vertical stacking of QDs and an increase in the regularity of the spacing between the QDs.[44] In the case of InGaN/GaN QDs, conflicting trends of a constant or an increase in QD density with increasing number of QD superlattices (SLs) have been reported, depending on the starting substrate.[45-47] Furthermore, variations in the QD dimensions and their band gap energies for similar In mole fractions have been reported.[45-50]

Band alignment across heterostructure interfaces may be type I ("nested") or type II ("staggered") band offsets.[51,52] GaSb QD systems have been identified as promising systems for a variety of optoelectronic applications, including light emitters (requiring type I offset) and photovoltaics and photodetectors (requiring type II offset). Although type I

band offsets have been demonstrated for GaAsSb/GaAs quantum wells,[51] type II band offsets are usually reported for GaSb/GaAs QDs.[52–56] Furthermore, band-edge calculations have predicted type I (type II) band offsets for unstrained (strained) GaSb/GaAs QDs.[57–59] However, the influence of strain on the band alignment within GaSb/GaAs QDs still remains unknown.

In addition, the band structure of a semiconductor can be tuned by alloying solute atoms into thin films. The addition of few percent of alloy species may dramatically change the optical and electronic properties of highly mismatched semiconductors. The Band anti-crossing (BAC) model predicts that this addition of solute atoms leads to a formation of localized impurity states near the band edges, whose interaction with the delocalized states of the crystal will lead to band splitting. In other words, the BAC model predicts that the addition of a few solute atoms may decrease or increase the energy of the effective conduction or valence band edges of a semiconductor alloy, respectively.

Therefore, a need exists to obtain nanometer-scale spatially resolved structural and electronic information from low-dimensional heterostructures. This chapter is organized as follows. First, methods typically used for examining the structural and electronic properties of heterostructures are described, with an emphasis on cross-sectional scanning tunneling microscopy and spectroscopy. Next, type I and type II band alignments are discussed. The chapter concludes with an outline of the dissertation.

1.2 Examination of Structural and Electronic Properties of Materials

Widely-used scanning techniques for investigating crystal and band structure of semiconductor heterostructures include high-resolution transmission electron microscopy (TEM), cross-sectional scanning tunneling microscopy (XSTM), scanning tunneling spectroscopy (STS), and photoluminescence (PL) spectroscopy. Although high resolution TEM can achieve a lateral resolution on the order of angstroms, the data is averaged from materials of tens of nm's in thickness.[60] The energy difference between lowest energy states of charges can be measured by PL experiments.[61-64] However, PL measurements are typically limited by the fast decay times of the excited carriers and provides information only on the energy difference between the ground states of the carriers.[65] Interpretation of PL data require several assumptions, such as interface abruptness, alloy composition, and film quality, leading to a spectra with a spatial average.[65,66] Furthermore, a blue shift in the PL emission peak with increasing illumination intensity has often been attributed to a type II band alignment, which will be discussed in more detail in Section 1.3. However, the blue shift in the PL emission peak only indirectly suggests a type II band alignment and does not provide any quantitative information about the valence and conduction band offsets. For example, a blue shift in the PL emission peak is reported for unstrained GaSb/GaAs interfaces, which are often reported to be type I.[57]

Cross-sectional scanning tunneling microscopy (XSTM) allows one to probe individual atoms of the top layer of a cleaved surface. The direct observations of the non-reconstructed surfaces can provide information about the spatial distribution of individual atoms and defects of the crystal structure.[66-71] Additionally, differences in the electronic properties, i.e. density of states at a given bias, of different semiconductors or nanostructures can be imaged via XSTM. After identifying a semiconductor interface or

nanostructure, scanning tunneling spectroscopy (STS) enables the spatially-resolved measurement of the band structure of single layers of semiconductors, which is not possible with PL measurements. Furthermore, the energy states of confined charges within a nanostructure can also be probed via STS.

In this dissertation, the structural and electronic properties of InGaN/GaN and GaSb/GaAs quantum dot heterostructures were examined using XSTM and STS. The STS measurements were performed using a variable-separation STS technique, which will be discussed in Chapter 2.5.

1.3 Type I and Type II Band Alignments

Due to the difference in conduction and valence band edges of semiconductors, semiconductor interfaces can facilitate spatial confinement of charges. A schematic diagram of electron and hole confinement at idealized (a) type I and (b) type II interfaces is presented in Fig. 1.2 for (a) A/B/A and (b) A/C/A semiconductor interfaces. When both the conduction and valence band edges of semiconductor B are lower in energy than those of semiconductor A, a type I, "nested", band alignment forms at the interface. On the other hand, when one of the conduction and valence band edges of semiconductor B is lower and the other is higher than those of semiconductor A, a type II, "staggered", band alignment forms at the interface and facilitates spatial separation of charge carriers. A possible applications of a type I band alignment is InGaN/GaN lasers, where carrier confinement in InGaN quantum well layers results in recombination of electron and hole pairs with an emission wavelength of 630 nm.[72] A possible application of a type II band alignment is

GaSb/GaAs quantum dot photovoltaic devices, which facilitates the generation of carrier charges by photon energy.[73] Carrier charges are spatially separated due to the type II band alignment and can be used to generate electric energy.

1.4 Dissertation Organization

This dissertation is organized as follows. In Chapter 2, the experimental procedures used for the fabrication and characterization of InGaAs(Sb)N QW, InGaN QD, and GaSb QD heterostructures are described. Details about film growth by the metalorganic vapour phase epitaxy (MOVPE) and molecular beam epitaxy (MBE) are presented. Furthermore, details about the characterization tools used, especially XSTM and variable separation STS, are also presented.

In Chapter 3, our investigations of the influence of Sb incorporation on the InGaAs(Sb)N/GaAs band alignment are presented. Heterostructures with and without Sb incorporation are grown by MOVPE and examined using secondary ion mass spectrometry (SIMS), high-resolution X-ray diffraction (HRXRD), cross-sectional scanning tunneling microscopy (XSTM), and scanning tunneling spectroscopy (STS) techniques. HRXRD of the heterostructures reveal that the InGaAs(Sb)N QW layers are both coherently compressively strained. Furthermore, SIMS measurements reveal the alloy composition of the InGaAs(Sb)N layers. XSTM and STS reveal effective band gaps of 1.2 eV (1.1 eV) for InGaAs(Sb)N alloys. At the InGaAsN/GaAs (InGaAsSbN/GaAs) interfaces, type II (type I) band offsets are observed, due to strain-induced splitting of the valence band and the incorporation of Sb. The Sb-induced variation in band alignment is significantly larger than

predicted values, suggesting the possibility of both VBO and CBO tuning at InGaAs(Sb)N/GaAs interfaces, with minimal Sb incorporation.

Chapter 4 presents investigations of the influence of the starting substrate on InGaN/GaN QD formation and properties. The QD density, dimension, and band gaps are compared for InGaN QDs grown on free-standing GaN or GaN/AlN/sapphire substrates. We propose residual stress around threading dislocation and strain field from buried QDs as QD nucleation sources of different starting substrates, and discuss their influences on the electronic band structure.

In Chapter 5, our investigations of the influence of GaAs termination on the GaSb/GaAs QD band alignment are presented. GaSb QDs grown on different termination surfaces are examined via XSTM and STS. The chapter also discusses formation of clustered QDs consisting of both coherent clusters and semi-coherent clusters with misfit dislocations, independent of GaAs surface termination. GaSb/GaAs QD band alignment is presented for various GaSb QDs. Computational predictions reveal that dislocation charging leads to a band alignment transition from type I to type II.

Finally, a summary and suggestions for future work are presented in Chapter 6.

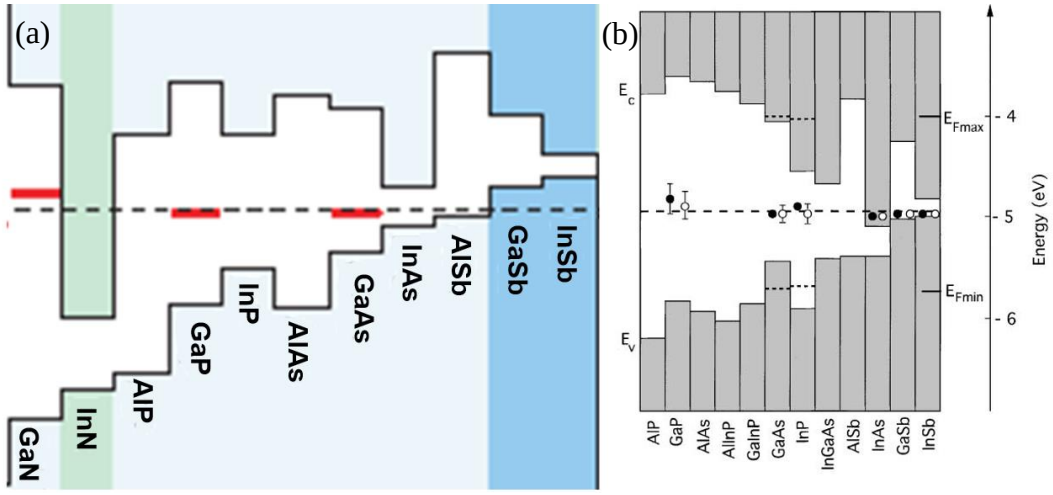

Fig. 1.1: Calculated band offsets relative to the Fermi energy levels of unstrained semiconductors using the electronic transition level of hydrogen in semiconductors.[38,39] The solid lines represent the valence and conduction band edges and the dashed lines represent the Fermi energy level. The stabilized Fermi energy level energies are indicated as (a) red lines or (b) filled circles. The opened circles in (b) correspond to the Fermi energy level on pinned semiconductor surfaces.

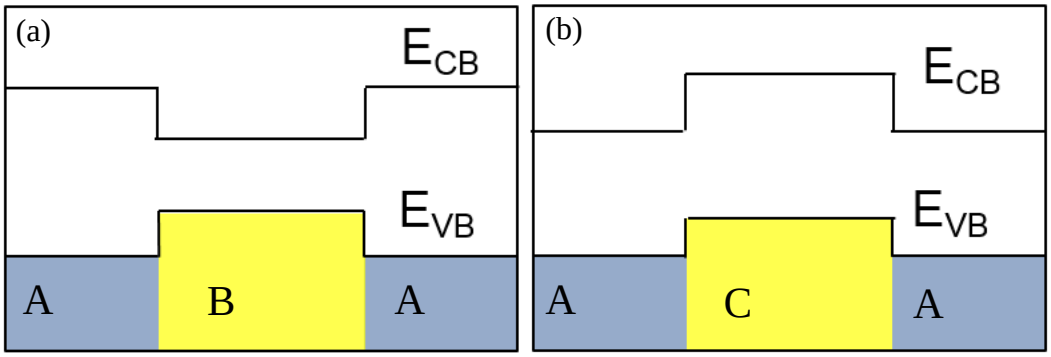

Fig. 1.2: Schematic diagrams of a (a) type I and (b) type II band alignments. The conduction and valence band edges are labeled as E_{CB} and E_{VB}, respectively. For a type I band alignment, conduction and valence band edges of semiconductor B are lower in energy than those of semiconductor A. For a type II band alignment, the conduction and valence edges of semiconductor C are lower and higher in energy than those of semiconductor A, respectively.

1.5 References

[1]H. Y. Liu, M. Hopkinson, C. N. Harrison, M. J. Steer, R. Frith, I. R. Sellers, D. J. Mowbray, and M. S. Skolnick, *J. of Appl. Phys.* **93**, 2931 (2003).

[2]A. Stintz, G. T. Liu, A. L. Gray, R. Spillers, S. M. Delgado, and K. J. Malloy, *J. of Vac. Sci. & Technol.* B **18**, 1496 (2000).

[3]J.-I. Chyi, T.-E. Nee, C.-T. Lee, J.-L. Shieh, and J.-W. Pan, *J. of Crys. Growth* **175-176**, 777 (1997).

[4]R. Songmuang, S. Kiravittaya, and O. G. Schmidt, *J. of Crys. Growth* **249**, 416 (2003).

[5]G. Costantini, A. Rastelli, C. Manzano, P. Acosta-Diaz, R. Songmuang, G. Katsaros, O. Schmidt, and K. Kern, *Phys. Rev. Lett.* **96** (2006).

[6]J. M. Ulloa, C. Celebi, P. M. Koenraad, A. Simon, E. Gapihan, A. Letoublon, N. Bertru, I. Drouzas, D. J. Mowbray, M. J. Steer, and M. Hopkinson, *J. of Appl. Phys.* **101**, 081707 (2007).

[7]Y. Horikoshi, M. Kawashima, and H. Yamaguchi, *Japan. J. of Appl. Phys.* **25**, L868 (1986).

[8]G. M. Guryanov, G. E. Cirlin, V. N. Petrov, N. K. Polyakov, A. O. Golubok, S. Y. Tipissev, V. B. Gubanov, Y. B. Samsonenko, N. N. Ledentsov, V. A. Shchukin, M. Grundmann, D. Bimberg, and Z. I. Alferov, *Surf. Sci.* **352**, 651 (1996).

[9]G. E. Cirlin, V. N. Petrov, V. G. Dubrovskii, A. O. Golubok, S. Y. Tipissev, G. M. Guryanov, M. V. Maximov, N. N. Ledentsov, and D. Bimberg, Czechoslovak, *J. of Phys.* **47**, 379 (1997).

[10]A. Bosacchi, P. Frigeri, S. Franchi, P. Allegri, and V. Avanzini, Journal of Crystal Growth **175-176**, 771 (1997).

[11]W. Cheng, Z. Zhong, Y. Wu, Q. Huang, and J. Zhou, *J. of Crys. Growth* **183**, 279 (1998).

[12]Y. Horikoshi, *J. of Crys. Growth* **201**, 150 (1999).

[13]J. D. Song, Y. M. Park, J. C. Shin, J. G. Lim, Y. J. Park, W. J. Choi, I. K. Han, J. I. Lee, H. S. Kim, and C. G. Park, *J. of Appl. Phys.* **96**, 4122 (2004).

[14]T. Haga, M. Kataoka, N. Matsumura, S. Muto, Y. Nakata, and N. Yokoyama, *Japan. J. of Appl. Phys.* **36**, L1113 (1997).

[15]P. B. Joyce, T. J. Krzyzewski, G. R. Bell, B. A. Joyce, and T. S. Jones, *Phys. Rev. B* **58**, R15981 (1998).

[16]A. Rosenauer, D. Gerthsen, D. V. Dyck, M. Arzberger, G. Böhm, and G. Abstreiter, *Phys. Rev. B* **64**, 245334 (2001).

[17]C. Heyn and W. Hansen, *J. of Crys. Growth* **251**, 140 (2003).

[18]D. Loss and D. P. DiVincenzo, *Phys. Rev. A* **57**, 120 (1998).

[19]E. Biolatti, R. C. Iotti, P. Zanardi, and F. Rossi, *Phys. Rev. Lett.* **85**, 5647 (2000).

[20]G. Yusa and H. Sakaki, *Appl. Phys. Lett.* **70**, 345 (1997).

[21]J. O. Winter, T. Y. Liu, B. A. Korgel, and C. E. Schmidt, *Adv. Mater.* **13**, 1673 (2001).

[22]I. R. Sellers, H. Y. Liu, K. M. Groom, D. T. Childs, D. Robbins, T. J. Badcock, M. Hopkinson, D. J. Mowbray, and M. S. Skolnick, *Electronics Lett.* **40**, 1412 (2004).

[23]H. C. Yu, J. S. Wang, Y. K. Su, S. J. Chang, F. I. Lai, Y. H. Chang, H. C. Kuo, C. P. Sung, H. P. D. Yang, K. F. Lin, J. M. Wang, J. Y. Chi, R. S. Hsiao, and S. Mikhrin, I*EEE Photon. Techn. Lett.* **18**, 418 (2006).

[24]A. D. Stiff, S. Krishna, P. Bhattacharya, and S. Kennerly, *Appl. Phys. Lett.* **79**, 421 (2001).

[25]J. Phillips, P. Bhattacharya, S. W. Kennerly, D. W. Beekman, and M. Dutta, *IEEE J. of Quantum Electonics* **35**, 936 (1999).

[26]J. D. Phillips, K. Kamath, and P. K. Bhattacharya, *Appl. Phys. Lett.* **73**, 1937 (1998).

[27]D. M. Bruls, J. W. A. M. Vugs, P. M. Koenraad, M. S. Skolnick, M. Hopkinson, and J. H. Wolter, *Appl. Phys. A* **72**, S205 (2001).

[28]A. Urbieta, B. Grandidier, J. P. Nys, D. Deresmes, D. Stievenard, A. Lemaitre, G. Patriarche, and Y. M. Niquet, *Phys. Rev. B* **77**, 155313 (2008).

[29]T. Yamauchi, Y. Ohyama, Y. Matsuba, M. Tabuchi, and A. Nakamura, *Appl. Phys. Lett.* **79**, 2465 (2001).

[30]T. Maltezopoulos, A. Bolz, C. Meyer, C. Heyn, W. Hansen, M. Morgenstern, and R. Wiesendanger, *Phys. Rev. Lett.* **91**, 196804 (2003).

[31]T. K. Johal, R. Rinaldi, A. Passaseo, R. Cingolani, A. Vasanelli, R. Ferreira, and G. Bastard, *Phys. Rev. B* **66** (2002).

[32]B. Legrand, B. Grandidier, J. P. Nys, D. Stievenard, J. M. Gerard, and V. Thierry-Mieg, *Appl. Phys. Lett.* **73**, 96 (1998).

[33]O. Millo, D. Katz, Y. W. Cao, and U. Banin, *Phys. Rev. B* **61**, 16773 (2000).

[34]H. Jiang and J. Singh, *Phys. Rev. B* **56**, 4696 (1997).

[35]H. Shin, Y. H. Yoo, and W. Lee, *J. of Phys. D* **36**, 2612 (2003).

[36]L. He, G. Bester, and A. Zunger, *Phys. Rev. B* **70**, 235316 (2004).

[37]H. Shin, E. Yoon, Y. H. Yoo, and W. Lee, *J. of the Phys. Soc. of Jap.* **73**, 3378 (2004).

[38]C. G. Van De Walle and J. Neugebauer, *Nature* **423**, 626 (2003).

[39]W. Walukiewicz, *Physica B* **123**, 302 (2001).

[40]S. Sato and S. Satoh, *Jpn. J. Appl. Phys.* **38**, 1990 (1999).

[41]N. Tansu, J. Y. Yeh, and L. J. Mawst, *Appl. Phys. Lett.* **82**, 4038 (2003).

[42]M. Kondow, T. Kitatani, S. Nakatsuka, M. C. Larson, K. Nakahara, Y. Yazawa, M. Okai, and K. Uomi, *IEEE J. Sel. Topics Quantum Electron.* **3**, 719 (1997).

[43]S. Sato and S. Satoh, *IEEE J. Sel. Topics Quantum Electron.* **5**, 707 (1999).

[44] J. Tersoff, C. Teicher, and M. G. Lagally, *Phys. Rev. Lett.* **76**, 1675 (1996).

[45] F. A. Ponce, S. Srinivasan, A. Bell, L. Geng, R. Liu, M. Stevens, J. Cai1, H. Omiya, H. Marui, and S. Tanaka, *J. Mater. Sci.* **48**, 1196 (2013).

[46]W.B. Lv, L. Wang, J. X. Wang, Z. B. Hao, , and Y. Luo, *Chin. Phys. Lett.* **28**, 128101 (2011).

[47]J. K. Rouviere, J. Simon, N. Pelekanos, B. Daudin, and G. Feuillet, *Appl. Phys. Lett.* **75**, 2632 (1999).

[49]T. D. Moustakas, T. Xu, C. Thomidis, A. Y. Nikiforov, L. Zhou, and D. J. Smith, *Phys. Stat. Sol. (a)* **205**, 2560 (2008).

[50]S. R. Meher, A. Subrahmanyam, and Mahaveer K. Jain, *J. Mater. Sci.* **48**, 1196 (2013).

[51]S. C. Davies, D. J. Mowbray, F. Ranalli, and T. Wang, *Appl. Phys. Lett.* **96**, 251904 (2010).

[52] T. S. Wang, J. T. Tsai, K. I Lin, J. S. Hwang, H. H. Lin, and L. C. Chou, *Mater. Sci. Eng., B* **147**, 131 (2008).

[53]J. Tatebayashi, B. Liang, D. A. Bussian, H. Htoon, S. Huang, G. Balakrishnan, V. Klimov, L. R. Dawson, and D. L. Huffaker, *IEEE Trans. Nanotechnol*. **8**, 269 (2009).

[54]B. Liang, A. Lin, N. Pavarelli, C. Reyner, J. Tatebayashi, K. Nunna, J. He, T. J. Ochalski, G. Huyet, and D. L. Huffaker, *Nanotechnology* **20**, 455604 (2009).

[55]N. N. Ledentsov, J. B€ohrer, M. Beer, F. Heinrichsdorff, M. Grundmann, D. Bimberg, S. V. Ivanov, B. Ya. Meltser, S. V. Shaposhnikov, I. N. Yassievich, N. N. Faleev, P. S. Kop'ev, and Z. I. Alferov, *Phys. Rev. B* **52**, 14058 (1995).

[56]R. J. Young, E. P. Smakman, A. M. Sanchez, P. Hodgson, P. M. Koenraad, and M. Hayne, *Appl. Phys. Lett.* **100**, 082104 (2012).

[57]K. Suzuki, R. A. Hogg, and Y. Arakawa, *J. Appl. Phys.* **85**, 8349 (1999).

[58] M. E. Rubin, H. R. Blank, M. A. Chin, H. Kroemer, and V. Narayanamurti, *Appl. Phys. Lett.* **70,** 1590 (1997).

[59] R. Timm, H. Eisele, A. Lenz, L. Ivanova, V. Vosseb€urger, T. Warming, D. Bimberg, I. Farrer, D. A. Ritchie, and M. D€ahne, *Nano Lett.* **10**, 3972 (2010).

[60]A. Ourmazd, F. H. Baumann, M. Bode, and Y. Kim, *Ultramicroscopy* **34**, 237 (1990).

[61]M. Arzberger and M. C. Amann, *Phys. Stat. Solid. B* **224**, 655 (2001).

[62]V. M. Apalkov, T. Chakraborty, N. Ulbrich, D. Schuh, J. Bauer, and G. Abstreiter, *Phys. E* 24, **272** (2004).

[63]M. Bayer and A. Forchel, *Phys. Rev. B* **65** (2002).

[64]D. J. Mowbray and M. S. Skolnick, *J. of Phys. D* **38**, 2059 (2005).

[65]A. Kaneta, T. Izumi, K. Okamoto, Y. Kawakami, S. Fujita, Y. Narita, T. Inoue, and T. Mukai, *Japan. J. of Appl. Phys.* **40**, 110 (2001).

[66]T. H. Gfroerer, *in Encyclopedia of Analytical Chemistry* (John Wiley & Sons Ltd, 2000), pp. 9209.

[67]R. S. Goldman, Journal of Physics D **37**, 163 (2004).

[68]R. M. Feenstra, Semiconductor Science and Technology **9**, 2157 (1994).

[69]R. B. Laghumavarapu, A. Moscho, A. Khoshakhlagh, M. El-Emawy, L. F. Lester, and D. L. Huffaker, *Appl. Phys. Lett.* **90**, 173125 (2007).

[70]B. Lita, Ph.D. Thesis, University of Michigan, 2002.

[71]T. Tsuruoka and S. Ushioda, *J. of Elect. Microscopy* **53**, 169 (2004).

[72]T. Frost, A. Banerjee, S. Jahangir, and P. K. Bhattacharya, *Appl. Phys. Lett.* **104**, 081121 (2014).

[73]P. J. Carrington, A. S. Mahajumi, M. C.Wagener, J. R. Botha, Q. Zhuang, A. Krier, *Physica B* **407**, 1493 (2012).

Chapter 2

Experimental Procedures

2.1 Overview

This chapter describes the experimental procedures used for the fabrication and characterization of the III-V and III-nitride heterostructures examined in this thesis. Molecular beam epitaxy (MBE) and metalorganic vapour phase epitaxy (MOVPE) growth tehcniques, which were used for the the growth of the III-V structures, are described. In addition, high-resolution X-ray diffraction (HRXRD), atom probe tomography (APT), ultra-high vacuum (UHV) cross-sectional scanning tunneling microscopy (XSTM) and plan-view STM (STM) techniques, which were used to examine the atomic-to-nanoscale structure of the III-V semiconductor heterostructure, are presented. Finally, the variable separation scanning tunneling spectroscopy (VS-STS) technique, used for measuring the effective bandgaps and band alignments, is described in detail.

2.2 Molecular Beam Epitaxy

Molecular Beam Epitaxy (MBE) facilitates molecular beams to produce high quality epitaxial films.[1] MBE growth occurs first by the sublimation or evaporation of solid sources, followed by the deposition of atoms or molecules on the growth surface via

reaction and condensation of the molecular beams.[2] Shutters of effusion cells, containing sources, are opened and closed in a controlled manner for depositing various atoms or molecules on the substrate surface. Furthermore, for the growth of GaN, an ultra-high purity N_2 plasma source is used. InGaN/GaN QD heterostructures were grown by T. Frost and A. Hazari in Prof. Bhattacharya's group at the University of Michigan. GaSb/GaAs QDs were grown by A. Martin in Prof. Millunchick's group at the University of Michigan and S. Clark in Prof. G. Balakrishnan's lab at the University of New Mexico.

2.3 Metalorganic Vapour Phase Epitaxy

Metalorganic vapour phase epitaxy (MOVPE) involves the flow of reactants to produce epitaxial film growth. MOVPE growth is performed by flowing metal-organic sources, such as tri-methyl gallium, and hydrides, such as AsH_3, across the substrate at an elevated substrate temperature in a pressure regime of 10 to 750 Torr.[3] The transport of precursors are performed by the use of a carrier gas, typically hydrogen gas. The precursors and hydrides, which are stable at room temperature, decompose at an elevated temperature. Prior to the growth of epilayers, the flow rate of precursors and carrier gases are calibrated to achieve a correct stoichiometry during crystal growth. InGaAs(Sb)N/GaAs quantum well heterostructures were grown by T. W. Kim in Prof. L. Mawst's group at the University of Wisconsin.

2.4 High Resolution X-ray Diffraction

High resolution X-ray diffraction (HRXRD) measurements were performed on semiconductor heterostructures in order to determine the in-plane strains, composition profile, and thickness of the layers. HRXRD experiments on InGaAs(Sb)N/GaAs QW and InGaN/GaN QD heterostructures were performed by T. W. Kim at the University of Wisconsin and J. Occena in the lab of Prof. R. Goldman at the University of Michigan, respectively. HRXRD measurements at both Wisconsin and Michigan were carried out using a BEDE D1 system, which utilizes a 2.2 kW filament tube with a copper target. A vertical slit with a width of ~0.5 mm was inserted between the sample and the detector. Generator settings of 40 mA and 40 kV were used for the generation of direct beams with an intensity of ~ 200 k counts/s. Samples were mounted on a goniometer and rotated around three angles, rocking (ω), tilting (χ), and azimuthal rotation (Φ). Prior to X-ray diffraction measurements, the symmetric reflection, (004) for GaAs and (002) for GaN substrates, were measured. Furthermore, the sample position and orientation were aligned to achieve the highest intensity signal. This is done by rotating the sample or detector by small angles such that the X-ray source, sample, and detector are in a configuration that satisfies Bragg's equation. For InGaN/GaN QD heterostructures, X-ray rocking curve (XRC) measurements, where the diffraction intensity is measured as a function of X-ray incident angle ω, were performed prior to the XRD measurements. However, the XRC data only revealed the substrate peaks. For both the InGaAs(Sb)N QW and InGaN/GaN QD heterostructures, XRD measurements were performed by rotating the sample and the detector about the substrate Bragg angle, while the angles 2θ and ω were maintained equal. The diffraction intensities were measured as a function of ω. For the XRD measurements on InGaN/GaN

QD heterostructures, each set of measurements was carried out at azimuth angles of 0^o and 180^o, to average out any epilayer tilt.

2.5 Atom Probe Tomography (APT)

To investigate the atomic arrangements of nanostructures, atom probe tomography (APT) experiments were performed in a Cameca local electrode atom probe (LEAP) system on semiconductor heterostructures. APT is an ex-situ, destructive characterization technique, which enables 3D imaging with a few Angstrom resolution.[4] To prepare samples for APT, we use focused-ion-beam (FIB) milling to fabricate a conical section of sample (i.e. an "APT tip") which contains the layers of interest.

LEAP APT instruments are equipped with a conical electrode positioned < 100 μm from the specimen tip, as shown in Fig. 2.1. The electrode serves as a guide for the electric field generated by pulses of high voltage to the edge of the sharp specimen tips. Using laser or voltage pulsing, the field effect enables evaporation of atoms and projection onto a position-sensitive detector. The ion time-of-flight and its position on the detector enable precise determination of the m/q ratio and atom position within the tip. This sequence is repeated multiple times, thereby enabling 3D reconstruction of the atom positions within the tip.

2.5.1 APT Sample Tip Preparation Procedure

To prepare samples for APT, we use focused-ion-beam (FIB) milling in a Helios secondary electron microscopy (SEM) system to fabricate a conical section of sample, which will be referred as the "APT tip". The APT tip preparation procedures were performed in a FEI Helios SEM-FIB system. Sample wafers were loaded onto the stage of the system such that the normal of the growth surface was parallel to the SEM and had an angle of 52^{o} with the ion beam source. A small portion of the sample was "lifted out" from the wafer and mounted on commercially available Si posts from Cameca. A detailed description of the lift out procedure is described in the thesis of a previous group member.[5] The "APT tip shaping" procedure were performed to shape the mounted piece into a cone. SEM images of the APT tip preparation steps are shown in Fig. 2.2.

Prior to the lift out and tip shaping procedures, the eucentric height of the sample was calibrated. Once a feature was centered in the field of view, the eucentric height, the position where tilting the sample does not change the distance from the electron beam source, was calibrated by (1) tilting the sample by 5^{o} and (2) changing the stage height. The above step was repeated for sample tilts of 30^{o}, 45^{o}, and 52^{o}.

The lift out procedure began by first depositing a Pt layer on the surface. In order to minimize the ion beam induced surface damage, 20 x 5 μm Pt layers were put on as a protection layer. Pt layer deposition was performed first by electron beam, followed by the ion beam. Once 100 nm thick Pt was deposited, as shown in Fig. 2.2 (a), edges around the Pt protection layer were milled out using the ion beam. Tilting the stage by 22^{o}, ion beam milling formed 30^{o} wedge shaped edges, partially freeing the prepared material from the wafer. Once three edges were milled, a sharp W needle, called the Omniprobe, was placed in contact with the sample and attached using Pt deposition. The final edge was cut with

the ion beam, and the wedge-shaped sample portion, shown in Fig. 2.2 (b), was transferred to the Si posts. As shown in Fig. 2.2 (c), a portion of the sample was aligned above the Si posts. The sample portion was mounted on the Si post using Pt deposition. Finally, the sample portion mounted on the Si post was detached from the rest of the wedge sample using ion beam milling. These steps were repeated to generate 4-6 APT tips on Si posts, and an example of the resulting sample piece is shown in Fig. 2.2 (d).

Finally, the sample is formed into a conical shape by tilting the sample stage 52^{o} such that the Si posts and the sample piece were facing the ion beam source. Ion beam milling with a 30 kV voltage and 230 pA current was used to mill out a donut pattern with a 4.5 μm outer diameter (OD) and a 1.2 μm inner diameter (ID). The resulting APT tip is shown in Fig. 2.2 (e). Shown in Fig. 2.2 (f)-(h), the final tip shaping procedures were performed with the following voltage, current, OD, and ID: (f) 30 kV, 80 pA, 4 μm OD, 0.8 μm ID, (g) 30 kV, 60 pA, 4 μm, 0.4 μm ID, and (h) 5 kV, 60 pA, 3 μm OD, 0 μm ID.

2.5.2 Voltage and Laser modes of APT

Prepared APT sample tips were loaded into the UHV LEAP chamber through a buffer chamber and stored in an intro chamber, rather than in air, to avoid oxidization on the surface of the tips and minimize the chances of tip fracture during an APT experiment. All voltage and laser mode APT runs on GaSb/GaAs QD samples were performed at a temperature of 20 K.

At the start of an APT experiment, a starting voltage of 500 V was applied between the detector and sample tip, resulting in an electric field that decreases the effective binding

force of atoms at the edge of the tip. The voltage was slowly ramped up with a constant voltage or laser pulse rate of 200,000 pulses/min, inducing field evaporation. The electric energy or thermal energy from the voltage or laser pulse ionizes the atoms and free them from the specimen, respectively.[4] The specimen position was fine-adjusted such that ionized atoms are collected over the whole detector area. Experiments lasted until all layers of interest were found or an APT tip fracture occurred. APT tip fractures were found to be strongly correlated to the APT tip preparation procedures. For example, all APT tips prepared from a 45^{o} wedge shaped edges rather than a 30^{o} wedge shaped edges resulted in tip fractures during an APT run, presumably due to the 45^{o} slip planes of GaAs substrate. Furthermore, APT tips prepared with a higher voltage at the final step of tip shaping procedure, 30 kV, resulted in a more rounded edge due to the ion damage from the ion beam.

2.6 Cross-sectional Scanning Tunneling Microscopy (XSTM)

In this section, an overview of the fundamentals and experimental procedures of cross-sectional scanning tunneling microscopy (XSTM) is provided. Furthermore, sample preparation prior to XSTM experiments are discussed. The XSTM experiments were carried in an Omicron VT-STM. The procedures and XSTM system used in my studies are similar to those discussed in Section 2.3 of the PhD thesis of Dr. V. Dasika,[6] and the different procedures used for XSTM work presented in this dissertation will be noted in the text.

2.6.1 Scanning Tunneling Microscopy Overview

The semiconductor heterostructures are investigated by either cleaving them in ultra-high vacuum (UHV) chambers to expose an atomically flat surface or by looking at the growth surface in plan-view. Cross-sectional STM experiments were performed on InGaAs(Sb)N/GaN quantum well (QW) and GaSb/GaAs quantum dot (QD) samples. An example of an XSTM topographic image is shown in Fig. 2.3(a). The bright and dark regions visible in the image correspond to layers of InGaN and GaN, respectively. As shown in Fig. 2.3(b) and Fig. 2.3(c), the application of a positive sample bias voltage, V, results in electron tunneling from the STM tip into the empty conduction band states of GaN or InGaN. Quantum tunneling through empty states of the different energy band structure for InGaN and GaN yields different tunneling current due to the difference in the density of states at a fixed applied potential.[7] Thus, the STM tip must move closer to (away from) the GaN (InGaN) surface to maintain a constant tunneling current. Therefore, the GaN (InGaN) layer appears darker (brighter) in the XSTM image.

InGaN/GaN QD samples were investigated using plan-view STM. To avoid oxidation of the surface, the samples were transferred from the MBE chamber via a vacuum desiccator system (~ 10^{-2} Torr) to the STM chamber. During the transfers between the MBE or STM chambers to the mobile transfer system, the samples were exposed to air for less than a minute. A more detailed description is the transfer is described in Chapter 4.3.

2.6.2 Sample Polishing

InGaAs(Sb)N/GaAs quantum well and GaSb/GaAs quantum dot XSTM samples were prepared by the following procedures. The III-V heterostructures were grown on a quarter of a 2" wafer with a thickness of approximately 500 μm. Earlier XSTM studies of GaAs substrates showed highest cleavage success rate for the (110) surfaces.[8,9] Thus, samples were cleaved along the [110] and [1 $\overline{1}$ 0] directions using a diamond scriber and glass slides, such that each piece will have dimensions of ~ 20 mm x 2 mm.[8] For the InGaAs(Sb)N/GaAs samples, the longer edge of the sample pieces were cleaved along the [110] direction. For the GaSb/GaAs samples, the longer edge of the sample pieces were cut along the [1 $\overline{1}$ 0] direction. Sample pieces then were thinned to approximately 200 μm by mechanical polishing from the backside, as follows. Each piece was thinned to ~ 300 μm using 800 grit SiC paper with average particle size ~ 12 μm, to ~ 250 μm using 1000 grit SiC paper with average particle size ~ 7 μm, and to ~ 200 μm using 1200 grit SiC paper with average particle size ~ 5 μm). The final sample pieces were examined for scratches of the surface.

InGaN/GaN XSTM samples were thinned down using a lapping equipment in Lurie Nanofabrication Facility (LNF) in the University of Michigan. Samples were thinned down to approximately 80 μm thick by lapping with 3 μm Al_2O_3 grit. In order to uniformly lap the samples, the sample is continuously rotated at a speed of 25 rpm. A constant pressure of 2 N/m^2 was applied to the rotating sample against the Al_2O_3 particles.

2.6.3 Sample Scribing

Following polishing, a shallow scratch, called a scribe mark, was made with a machine-controlled diamond scriber at the LNF in Michigan along the width of the growth side of the sample. InGaAs(Sb)N QW samples were scribed along the [1 $\overline{1}$ 0] direction, while the GaSb QD samples were scribed along the [110] direction.[8] The machine-controlled diamond scriber applies a constant pressure to the sample piece, which sometime resulted in sample fracture. Thus, scribe marks were made on Si wafers with various pressure settings and the depth of the scribe marks were examined using an optical microscope in LNF. The pressure setting that resulted in a scribe depth of 1/3 of the Si wafer thickness was found, and half of the pressure setting was used for scribing the GaAs substrates as for the GaN substrates.

A schematic diagram of sample scribing is shown in Fig. 2.4.[6] Samples with lengths larger than 12 mm and widths of approximately 1-2 mm were prepared by making a scribe mark 7 mm away from one of the edges.[6,8,9] For samples with length from 10 to 12 mm, the scribe mark was made 5 mm away from one of the edge. For all cases, the scribe mark length was 1/3 of the sample width.[6,8] As will be discussed in the later chapters, flat cleaves were achieved from the InGaAs(Sb)N QW and GaSb QD samples with length-to-width ratios of approximately 7.

Scribed samples were mounted, held by rectangular jaws, in a cross-sectional sample holder, such that the scribe marks were parallel to the edge of the jaw. The epilayer side of the samples were loaded facing up with the scribed end resting directly on the back of the sample holder. Schematic photos are shown in Section 6.2.3 of the Ph.D. thesis of Dr. V. Dasika.[6] Once the samples were mounted onto the sample holder, the sample holder

was loaded into the load lock of STM system and pumped down with a turbo pump, for subsequent transfer into the STM chamber.

2.6.4 STM Tip Preparation

All the STM and STS experiments described in this dissertation were performed with commercially available Pt/Ir STM tips from Bruker AFM Probe. The STM tips were cleaned *in situ* by electron bombardment, emitted from a W filament.[6,10] Electron emission was achieved by applying a positive bias of 980 V to the tip relative to the W filament and running a current of 0.85 A through the filament. The voltage applied is higher and filament current lower compared to those reported in theses of earlier group members due to a larger distance between the filament and STM tip and usage of W filaments instead of Mo filaments.[6,9] The emitted electrons are accelerated towards the end of the positively biased STM tip, resulting in an emission current of 80 mA. The emission current is held constant for 2 minutes to ensure removal of contamination at the end of the STM tip. The STM tip cleaning procedure significantly increases the STM chamber pressure, up to 10^{-9} Torr, and STM tips are cleaned *in situ* at least 12 hours before an experiment.

2.6.5 UHV Sample Preparation

After the transfer of the sample from the load-lock to the chamber, there are several steps that are performed in UHV prior to the XSTM experiment. First, STM tips are cleaned via electron bombardment and the pressure of the chamber was ensured to be below

5×10^{-11} Torr. The ion gauge of the STM chamber is turned off 12 hours before the start of the experiment to avoid thermal drift of the STM tip. The sample is cleaved by mechanically lowering a 60° diamond tip into contact to the edge of the sample.

Following cleaving, the surface is visually examined using a telescope with a magnification of 40x. The sample is transferred to the STM scanning stage and the exposed cleavage surface is examined to ensure that the exposed surface does not have large cracks or rough topography. The cleaved surface features are recorded to keep track of the cleave success rate. Fig. 2.5 shows an example of a sketch of an ideal cleaved surface, where fracture lines are abundant near the scribe mark.[6] Away from the scribe mark, a flat area is shown on the cleaved surface. The initial STM tip approach is performed away from the scribe mark, as indicated by the filled circles in Fig. 2.5.[6]

Finally, the walk-off procedure is performed by the following procedures. The STM tip is brought near the sample surface using the coarse piezo motion of the tip. The tip is brought within the tunneling range of the sample by performing an auto-approach, where the tip was moved close to the sample surface in steps until a quantum tunneling current was detected. The STM tip was then retracted away from the surface by at least 1 μm and moved towards the growth edge of the sample by 300 nm. The STM tip was then auto-approached to the sample, and the tip height was recorded. The procedures were repeated until a tunneling current was not detected for a tip extension towards the surface of 2 μm. Once the edge of the sample was located, the STM tip was deflected back towards the substrate by at least 2 μm. The experiment proceeded after a 2 hour wait to prevent tip drift due to piezo creep.

2.6.6 Heterostructure Design

In order to increase the probability of achieving a successful cleavage with an atomically flat surface, it is necessary for the heterostructures to be strain-balanced. This can be achieved by growing a large capping layer above the heterostructures of interest, typically > 500 nm. Furthermore, in order to identify the layers of interest, marker layers, which are distinct in their appearance in the STM images, are grown below and above the heterostructures of interest. The marker layers used for the InGaAs(Sb)N/GaAs QW and GaSb/GaAs QD XSTM samples in this thesis are GaAs/AlAs superlattices. The growth and sample structure details of heterostructures can be found in Chapters 3 and 5.

Furthermore, the heterostructure and substrate of XSTM samples are highly doped, > 5 x 10^{18} cm^{-3}, in order to reduce the effects of tip-induced band bending. The tip-induced band bending causes the applied voltage bias between the STM tip and semiconductor to drop gradually across the vacuum gap, leading to shifts in the effective band edges.[11,12] For example, the expected shift for GaAs is expected to decrease from several tenths of an eV to ~ 0.1 eV as we increase the doping concentration from 1 × 10^{17} cm^{-3} to > 1 × 10^{18} cm^{-3}.[13]

InGaN/GaN QD heterostructures were designed for plan-view STM studies. The top layer of the InGaN QDs were uncapped, and grown on either a free-standing GaN substrate, which was grown on and separated from Si substrate, and GaN on AlGaN on sapphire substrates. For the plan-view STM samples, the GaN buffer layers were n+ Si-doped at ~5 x 10^{18}/cm^3.[14]

2.7 Variable-Separation Scanning Tunneling Spectroscopy (VS-STS)

For the research presented in this dissertation, a variable-separation scanning tunneling spectroscopy (VS-STS) technique was utilized which is described in detail in the theses of our previous group members.[6,9] However, for the VS-STS performed in this dissertation, a difference from the works of previous members is that the sample is grounded while a bias voltage was applied to the tip. Furthermore, VS-STS measurements were performed during STM imaging rather than after an image was completed. The feedback loop, which maintains a constant tunneling current, was turned off at the start of a VS-STS measurement. Therefore, different constant tunneling current settings used for STM imaging can result in different starting separation between the sample and STM tip. Thus, the constant tunneling current for STM imaging during VS-STS measurements of each experiment were unchanged.

Following the collection of the current and conductance spectra, the data are normalized and analyzed to determine the band edges of the semiconductor. The band edge determination procedures are described in Appendix A and were based on the prior work by A. Cummel, B. Lita, and R. M. Feenstra.[9,15,16]

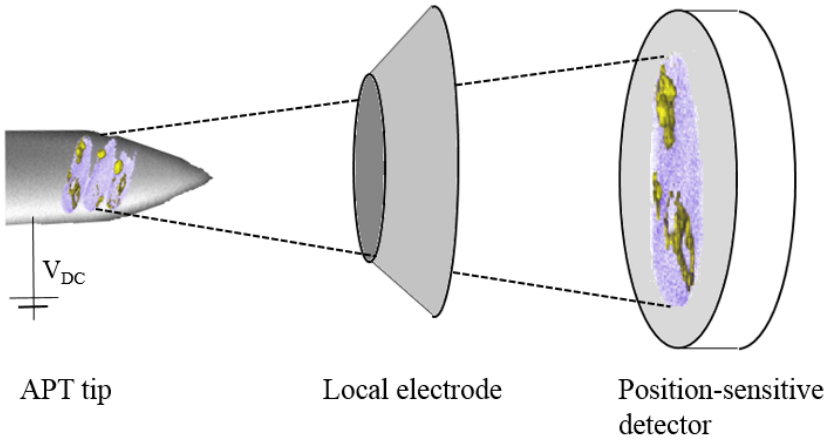

Fig. 2.1: Schematic of atom probe tomography (APT). The laser or voltage pulses are applied to the conical section of the sample, i.e. APT tip, such that semiconductor nanostructures in the APT tip are evaporated. The ionized atoms are accelerated to the position-sensitive detector and the time of flight is recorded. The collection of ionized atoms can be reconstructed in 3D to reveal the atomic structure of the nanostructures.

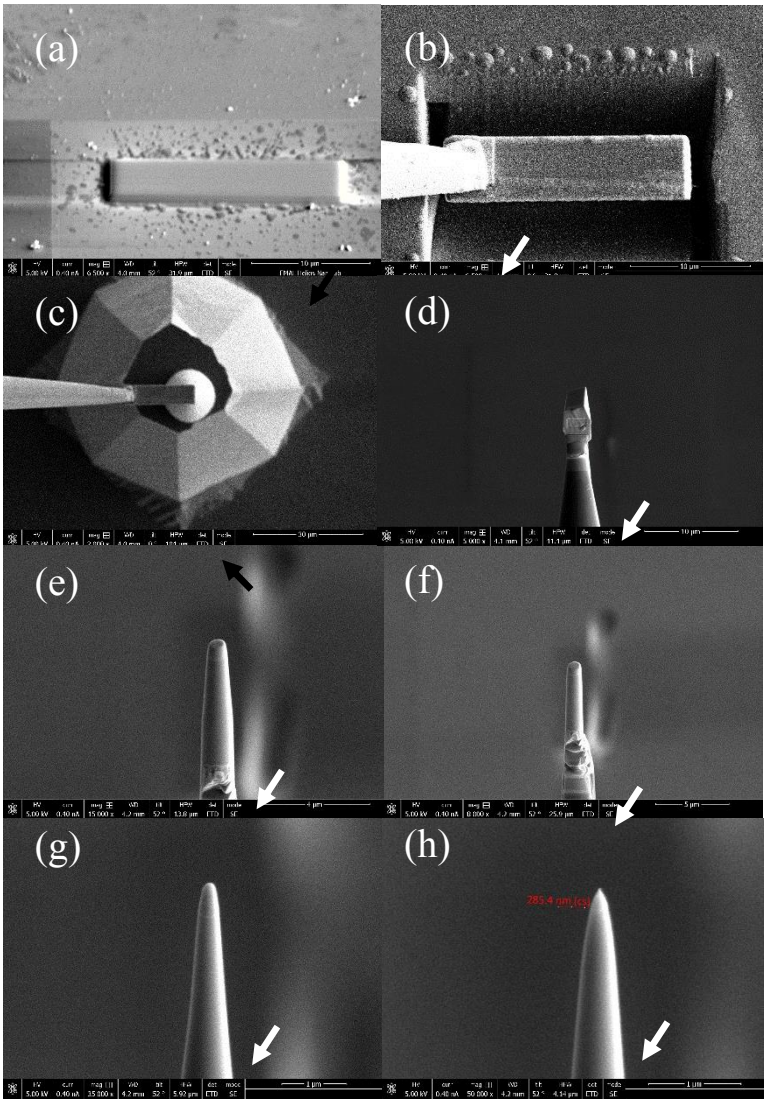

Fig. 2.2: Scanning electron microscopy images of the (a)-(d) lift out procedure and (e)-(h) the tip shaping procedures. [5] (a) Pt protection layer is deposited on the surface to avoid ion beam damages. (b) A sharp needle is attached to the sample wedge with Pt deposition, and the wedge shaped sample is being lifted out. (c)-(d) Wedge shaped sample is mounted on a Si post. (e)-(h) While the sample stage is tilted to 52^{o}, tip shaping procedure is performed with focused ion beam with various voltage and current settings. The interface between the sample and Pt protection layer is indicated with an arrow in each images.

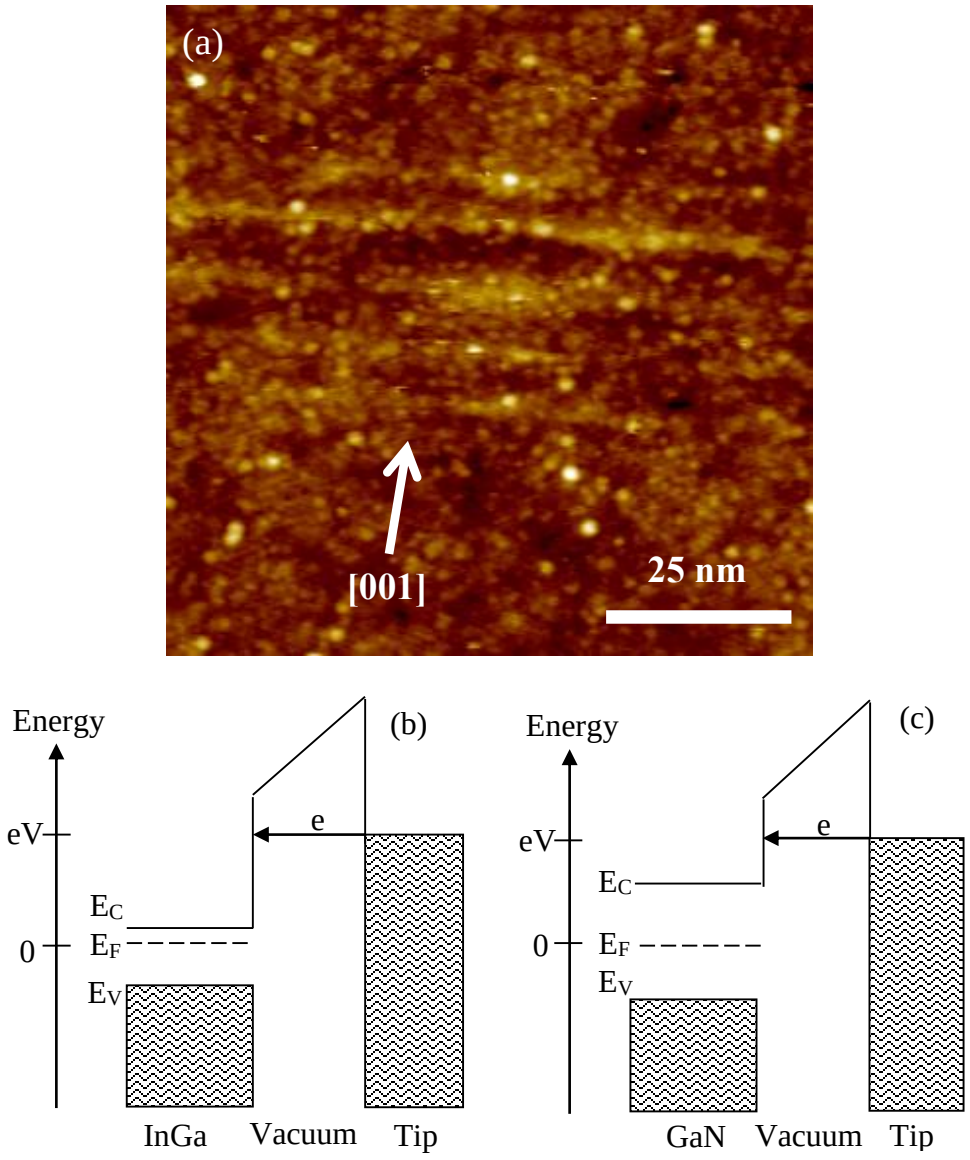

Fig. 2.3: (a) XSTM topographical image of InGaN dots in a GaN matrix. Schematics of the tunneling process between a tip and a sample under positive sample bias are shown.[11] The electrons tunnel from the tip into the energy levels above the Fermi level (E_F) of either (b) InGaN or (c) GaN. Since there are more states available to tunnel in InGaN than GaN, the InGaN layers will appear brighter in a constant-current STM image.[6]

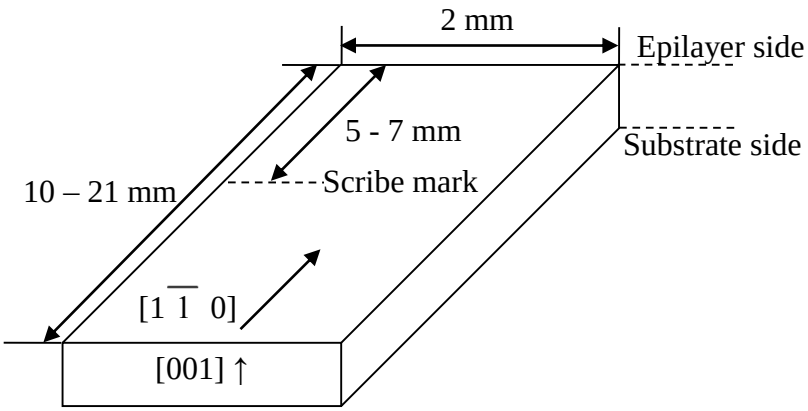

Fig. 2.4: Diagram showing the orientations of the (001)-oriented III-V samples.[11] Samples with lengths larger than 12 mm and widths of approximately 1-2 mm were prepared by making a scribe mark 7 mm away from one of the edge. For samples with length from 10 to 12 mm, the scribe mark was made 5 mm away from one of the edge. For all cases, the scribe mark length was 1/3 of the sample width.[6]

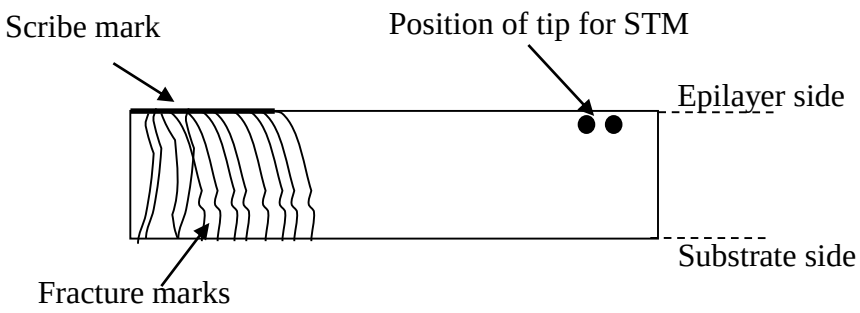

Fig. 2.5: Schematic of an ideal cleaved surface as seen from the telescope.[11] Observing through the telescope, the exposed cleaved surface is usually rough near the scribe mark, containing parallel fracture lines. On the opposite end of the cleaved surface, away from the scribe mark, the surface is usually free of the fracture lines. STM tips are approached to regions far away from these fracture marks. Representative tip positions are indicated by filled circles.[6]

2.8 References

[1]A. Y. Cho and S. E. Stokowsk, Solid State Communications **9**, 565 (1971).

[2]M. A. Herman, W. Richter, and H. Sitter, *Epitaxy Physical Principles and Technical Implementation*. (Springer, 2004).

[3]T. F. Kuech, *Proceed. of the IEEE* **80**, 1609 (1992).

[4]A. Cerezo, P. H. Clifton, M. J. Galtrey, C. J. Humphreys, T. F. Kelly, D. J. Larson, S. Lozano-Perez, E. A. Marquis, R. A. Oliver, G. Sha, K. Thompson, M. Zandbergen, and R. L. Alvis, *Materials Today* **10**, 36 (2007).

[5]R. Collino, Ph.D. Thesis, University of Michigan, 2010.

[6]V. Dasika, Ph.D. Thesis, University of Michigan, 2010.

[7]R. S. Goldman, *J. of Phys. D* **37**, 163 (2004).

[8]J. N. Gleason, Master's Thesis, University of Michigan, 2006.

[9]B. Lita, Ph.D. Thesis, University of Michigan, 2001.

[10]R. M. Feenstra, J. Y. Lee, M. H. Kang, G. Meyer, and K. H. Rieder, Physical Review B **73**, 035310 (2006).

[11]R. M. Feenstra, J. Y. Lee, M. H. Kang, G. Meyer, and K. H. Rieder, *Phys. Rev. B* **73**, 035310 (2006).

[12]B. Shin, B. Lita, R. S. Goldman, J. D. Phillips, and P. K. Bhattacharya, *Appl. Phys. Lett.* **81**, 1423 (2002).

[13]R. M. Feenstra, *Phys. Rev. B* **50** (1994).

[14]T. Frost, A. Banerjee, S. Jahangir, and P. K. Bhattacharya, *Appl. Phys. Lett.* **104**, 081121 (2014).

[15]J. G. McLean, P. Kruse, A. C. Kummel, *Surf. Sci.* **424**, 206 (1999).

[16]R. M. Feenstra, J. A. Stroscio, and A. P. Fein, *Surf. Sci.* **181**, 295 (1987).

Chapter 3

Influence of Sb Incorporation on the InGaAs(Sb)N/GaAs Band Alignment

3.1 Overview

This chapter discusses the influence of Sb incorporation on the effective bandgaps and band offsets at InGaAs(Sb)N/GaAs interfaces grown by metalorganic vapor phase epitaxy. Using cross-sectional scanning tunneling microscopy and spectroscopy, the band alignments across InGaAsN/GaAs and InGaAsSbN/GaAs interfaces were investigated. InGaAs(Sb)N based heterostructures were grown using metal organic vapour phase epitaxy by TaeWan Kim at Univ. of Wisconsin. The structural and electronic properties of InGaAs(Sb)N layers were investigated via high-resolution X-ray diffraction (HRXRD), secondary ion mass spectroscopy (SIMS), XSTM, and STS. We report that in the presence of Sb, the localized Sb energy level effectively shifts up both the valence and conduction bands of InGaAsSbN, leading to a type I alignment with larger (smaller) VBO (CBO). The Sb-induced variation in band alignment is significantly larger than predicted values, suggesting both VBO and CBO tuning of InGaAs(Sb)N/GaAs interfaces, with minimal Sb incorporation. This work was supported in part by the National Science Foundation through the Materials Research Science and Engineering Center (MRSEC) at the University of Wisconsin, grant DMR-1121288 and published in Applied Physics Letters.[1]

3.2 Background

Dilute nitride semiconductor heterostructures are promising for long-wavelength lasers due to its large reduction in band gap energy when only few percent of nitrogen is added to III-V semiconductors. It has been proposed that long-wavelength lasers can be achieved by growing highly strained InGaAs or InGaAsN layers on GaAs substrates.[2-4] For GaAsN/GaAs interfaces, a type II band alignment with a valence band offset of 20meV per nitrogen mole fraction has been observed.[5-7] As indium is added to GaAsN, the valence (conduction) band edges are predicted to increase (decrease), leading to the transformation from a "staggered" type II to a "nested" type I band alignment.[8] For $In_xGa_{1-x}As_{1-y}N_y$/GaAs interfaces with indium fraction (x_{In}) < 0.09, a type II band alignment is predicted.[9] In the case of $x_{In} \geq 0.09$, the strain induced splitting of the valence band maximum is expected to lead to the formation of a type I band offset.[10-12] Recently, as shown in Fig. 3.1, it has been proposed that lasers with wavelength longer than 1.5 μm can be achieved by incorporating small fraction of Sb into InGaAsN layers.[13,14] Band anti-crossing model predicts that incorporation of N or Sb to GaAs leads a decrease in the band gap energy, as shown in Fig. 3.2, due to the impurity state induced band splitting, respectively. As shown in Fig. 3.2 (a), the BAC model predicts a nitrogen impurity state near the conduction band edge, leading to a decrease in the effective band gap as x_N increases.[15] As shown in Fig. 3.2 (b), the antimony impurity state is localized near the valence band edge, leading to an increase in the effective valence band edge as x_{Sb} increases.[16] As Sb is added to InGaAsN(Sb), experiments report a band gap decrease of 24 meV per Sb mole fraction with a type I InGaAsN(Sb)/GaAs band offset.[9,10,14,17-20] It has been proposed that the addition of Sb to

InGaAsN would enable VBO tuning without significant changes to the conduction band offset (CBO).[10] On the other hand, the band anti-crossing (BAC) model predicts variation in both the VBO and CBO as Sb is incorporated into InGaAsN.[11] Thus, the influence of Sb incorporation on the VBO and CBO on the InGaAs(Sb)N/GaAs band alignment still remains unknown.

3.3 Growth of InGaAs(Sb)N Quantum Well Structures

InGaAs(Sb)N samples were prepared by MOVPE at a reactor pressure of 100 Torr (150 Torr), using trimethyl indium, trimethyl gallium, tertiary butyl arsine, dimethyl hydrazine, and trimethyl antimony as source gases.[13,14] The InGaAs(Sb)N layers were grown at 525 °C on p+ GaAs (001) substrates. The 110 nm InGaAs(Sb)N layers were surrounded by 100 nm p+ GaAs buffer and 110 nm p+ GaAs cap both grown at 630 °C. In addition, the heterostructures included two sets of AlAs/GaAs short-period (Λ=4nm) superlattices (SL), which serve as marker layers. During the growth of InGaAsN (InGaAsSbN), the gas phase molar flow rates were In/III=0.0205 and DMHy/TBA=7.51 (In/III=0.0067, DMHy/TBA=15.32, and Sb/(Sb+As)=0.0886).[13,14] Following growth, part of the InGaAsSbN sample was annealed in the MOVPE chamber under constant As overpressure at 790 °C for 45 minutes, followed by N_2 overpressure at 700 °C for 15 minutes. We will refer to the InGaAs(Sb)N sample before and after post-growth *in situ* annealing as "as-grown" and "annealed" InGaAs(Sb)N, respectively.

3.4 Characterization of InGaAs(Sb)N Quantum Well Structures

The goal of these studies was to investigate the band-offsets at InGaAs(Sb)N/GaAs interfaces at the nanometer-scale. As shown in Fig. 3.3, the heterostructure consists of InGaAs(Sb)N layers grown on a (001) GaAs substrate. The heterostructure also contains an AlAs/GaAs superlattice, which would serve as a marker layer.

3.4.1 Experimental Details

HRXRD measurements were performed using Cu $K_{\alpha 1}$ radiation monochromated by a four-reflection monochromator that employs Ge (220) reflections. Analysis of a series of ω-2θ scans collected near the GaAs (004) reflection suggests coherent compressive strains up to 0.38% (0.25%) at the InGaAs(Sb)N/GaAs interfaces. SIMS reveals a non-negligible In background (2×10^{-3}) for all grown layers, presumably due to an indium memory effect of the MOVPE growth system, with saturation compositions of $In_{0.07}Ga_{0.93}As_{0.98}N_{0.02}$ and $In_{0.043}Ga_{0.957}As_{0.975}Sb_{0.01}N_{0.015}$ apparent near the top interfaces with GaAs. Rocking Curve Analysis by Dynamical Simulation (RADS)[21] was also performed using the SIMS composition profiles, with constant In, N, and Sb fractions within the InGaAs(Sb)N layer, as input. Although SIMS suggests significant [In] interfacial transients, these are likely related to ion-sputtering induced intermixing.[22,23] The material database and details of the RADS simulation are discussed in Appendix C and D.

In preparation for XSTM, the samples were thinned to ~150 μm using conventional mechanical polishing from the backside. The samples were cleaved to expose a (110)

surface, in an ultra-high vacuum (UHV) chamber with base pressure < 4 x 10^{-11} Torr. Both STM and STS were performed with commercially available Pt/Ir tips, which were cleaned *in situ* by electron bombardment. STS measurements were performed using the variable tip-sample separation method.[24,25] All images were obtained with sample bias voltages of ± 2.1 V and constant tunneling currents ranging from 200 to 300 pA. We examined several XSTM images spanning > 0.8 μm^2 and acquired STS spectra across the interfaces between GaAs and InGaAsN, InGaAsSbN, and annealed InGaAsSbN layers.

3.4.2 HRXRD and RADS

For (a) InGaAsN and (b) InGaAsSbN-based structures, data from (004) ω-2θ scans, in comparison with RADS[21] simulations, with and without the InGaAsN (InGaAsSbN) layers, are shown in Figs. 3.4 (a) and 3.4 (b), respectively. The GaAs substrate peak position is arbitrarily set to $\Delta\theta$ =0 arcsec, thereby facilitating comparison of Bragg angle differences between the substrate and epilayers. For both the InGaAsN and InGaAsSbN-based structures, the XRD spectra, labeled "data" in Figs. 3.4 (a) and 3.4 (b), include InGaAs(Sb)N epilayer peaks at approximately $\Delta\theta$ < 0.4° and 1st order satellite peaks at approximately $\Delta\theta$ = ± 1.2°, which are associated with the 4.3 nm period AlAs/GaAs superlattices. To consider the contribution of the AlAs/GaAs SLs at low diffraction angles, RADS simulations in the absence of the InGaAsN and InGaAsSbN layers were performed. These are shown by the dotted lines labeled "AlAs/GaAs only," in Figs. 3.4 (a) and 3.4 (b). In addition, RADS simulations of both InGaAsN- and InGaAs(Sb)N-based structures (using the step-graded indium fraction as shown in Figs. 3.5 (b) and 3.5 (d)), are plotted as

dashed-dotted lines labeled "simulations" in Figure 3.4. For both structures, the "AlAs/GaAs only" RADS simulations suggest a minimal influence of the superlattices in the mid-angle region, $\pm 0.1° < |\Delta\theta| < \pm 0.4°$. For the InGaAsN based structure, both the HRXRD data and simulation reveal three epilayer peaks at $\Delta\theta = 0.13°$, 0.2°, and 0.33°, which correspond to indium fractions of $x_{In} = 0.01$, 0.02, and 0.06. For the InGaAsSbN layer, a single epilayer peak at $\Delta\theta = 0.16°$ is observed. Thus, these angular separations suggest the presence of coherent compressive strains up to 0.38% (0.25%) at the InGaAs(Sb)N/GaAs interfaces.

3.4.3 XSTM and SIMS of InGaAs(Sb)N

Figure 3.6 shows large-scale XSTM images and corresponding SIMS data for (a)-(b) GaAs/InGaAsN/GaAs and (c)-(d) GaAs/InGaAsSbN/GaAs structures. In the large-scale XSTM image shown in Fig. 3.5 (a), cleavage-induced surface steps (1nm height) are observed at the interface between the GaAs and InGaAsN layers, and within the AlAs/GaAs SLs, as indicated by arrows. In addition, in the XSTM image of the InGaAsSbN heterostructure, shown in Fig. 3.5 (c), cleavage-induced monolayer-height surface steps are apparent, as indicated by the arrows. The reduced step heights at the InGaAsSbN/GaAs interface in comparison to those at the InGaAsN/GaAs interface are likely due to a lower interfacial strain, consistent with the HRXRD data discussed earlier.

The SIMS data, shown in Fig. 3.6 (b) and 3.6 (d), consist of depth-dependent atomic concentrations, with the + y-axis corresponding to the film growth direction. Within the InGaAs(Sb)N structures, the SIMS data reveal regions with locally higher (lower) Al (Ga)

fractions, indicating the presence of AlAs/GaAs SL. For the InGaAsN structures, a non-zero background Al fraction (~1 x 10^{-6}) is observed, with an Al fraction gradient in the vicinity of the top InGaAsN/GaAs interface, ultimately reaching 3.5 x 10^{-5}. For the InGaAsSbN based structures, the background Al fraction remains constant at < 3.5 x 10^{-5}, suggesting that this value corresponds to the SIMS detection limit for Al. In addition, nearly constant N and Sb fractions are observed for the InGaAsSbN (InGaAsN) layers.

It is interesting to note that a non-negligible In background (~2 x 10^{-3}) is observed for all grown layers, as shown in Fig. 3.6 (b) and (d). At the interface between the GaAs substrate and the epitaxial GaAs buffer layer, the indium fraction increases from ~10^{-5} to 5 x 10^{-3}. In addition, a gradient in In fraction within InGaAs(Sb)N is apparent near the lower interface with GaAs. We note that saturation compositions of $In_{0.07}Ga_{0.93}As_{0.98}N_{0.02}$ and $In_{0.043}Ga_{0.957}As_{0.975}Sb_{0.01}N_{0.015}$ are apparent near the top interfaces with GaAs. The high background level of indium fraction during the growth of these structures is likely an indium memory effect of the MOVPE growth system. In addition, the indium fraction gradient at the bottom GaAs/InGaAs(Sb)N interface is likely due to a TMIn source transient during the initial stages of InGaAs(Sb)N layer growth. Indeed, as shown in Fig. 3.4, RADS simulations, using a constant indium fraction as input, as shown in Figs. 3.5 (b) and (d), predict distinct substrate and epilayer peaks, consistent with the HRXRD data. As mentioned above, the misfit strain calculated from the angular separation between these peaks suggest the presence of coherent compressive strains of 0.38% (0.25%) at the InGaAs(Sb)N/GaAs interfaces.

3.4.4 STS of InGaAs(Sb)N Layers

Figure 3.7 presents plots of normalized conductance versus sample voltage collected from the (a) as-grown GaAs/InGaAsN, (b) as-grown GaAs/InGaAsSbN, and (c) annealed GaAs/InGaAsSbN interfaces. In all cases, the data was collected near the top InGaAs(Sb)N/GaAs interfaces, as shown in Figs. 3.5 (b) and 3.5 (d). In all spectra, the sample voltage corresponds to the energy relative to the Fermi level. Indeed, the GaAs spectra, shown as the solid-line spectra in Figs. 3.7 (a) – 3.7 (c), display well-defined band edges, with effective GaAs bandgap values of 1.5 ± 0.5 eV, similar to that of bulk GaAs at room temperature. We note that the background In fraction, 2×10^{-3}, is expected to reduce the GaAs band gap by < 10 meV. The effective bandgaps of the InGaAsN(Sb) are lower than those of GaAs, consistent with literature reports of decreasing effective bandgaps with increasing indium and antimony fractions.[3,5-8,12-14] In Fig. 3.7 (a), the effective band gap of the as-grown $In_{0.07}Ga_{0.93}As_{0.98}N_{0.02}$ is 1.2 ± 0.1 eV, within 8 % of the values reported in the literature.[11,13,14] For the as-grown and annealed InGaAsNSb layers, in Fig. 3.7 (b) and 3.7 (c), the effective bandgaps are 1.1 ± 0.1 eV, within 3 % of literature reports.[5,13,14]

We now discuss the effective VBO and CBO at the InGaAs(Sb)N/GaAs interfaces. For the $In_{0.07}Ga_{0.93}As_{0.98}N_{0.02}$/GaAs interface, STS reveals InGaAsN effective conduction and valence band edges with lower energy values than those of GaAs, as shown in Fig. 3.7 (a). Thus, at the InGaAsN/GaAs interface, a type II band offset with VBO of 0.13 ± 0.1 eV and CBO of 0.30± 0.1 eV is apparent. For $x_{In} \geq 0.09$, there have been many experimental and theoretical reports of Type I band offsets, with ΔE_c and ΔE_v ~0.2 eV.[3] On the other hand, Type II band offsets have been predicted for InGaAsN/GaAs interfaces

with low misfit strain ($x_{In} < 0.09$).[4] In the absence of Sb, it has been predicted that the low misfit strain at the InGaAsN/GaAs interface would lead to minimal splitting of the valence band, resulting in a type II band alignment.[3] Since low indium fraction is predicted to have negligible influence on the valence band energy,[3] the InGaAsN/GaAs band alignment is likely to be similar to the $GaAs_{0.978}N_{0.022}$/GaAs band alignment, which is also predicted to be type II.[2]

For both the as-grown and annealed InGaAsSbN/GaAs interfaces, the InGaAsSbN effective band edges have lower energy values than those of GaAs, as shown in Figs. 3.7 (b) and 3.7 (c), suggesting a type I band alignment, consistent with both experimental and theoretical reports.[5,6,8,9,11] At the as-grown $In_{0.043}Ga_{0.957}As_{0.975}Sb_{0.01}N_{0.015}$/GaAs interface, a VBO of 0.26 ± 0.05 eV and a CBO of 0.11 ± 0.1 eV are revealed. In addition, at the annealed InGaAsSbN/GaAs interface, a type I band alignment with a VBO of 0.25 ± 0.1 eV and a CBO of 0.11 ± 0.01 eV is apparent. Although annealing-induced blue shift in photoluminescence emission is often observed in InGaAsSbN/GaAs heterostructures,[13,27] our STS data suggest minimal annealing-induced changes in VBO and CBO. Our experimental value of VBO (CBO) at the InGaAsSbN/GaAs interface is within 1% (8 %) of the experimental values reported in the literature.[5] Our data further indicates an Sb-induced increase (decrease) in the VBO (CBO) of ~350 meV (200 meV) at the InGaAsSbN/GaAs interface, leading to a transition from type II (InGaAsN/GaAs) to type I (InGaAsSbN/GaAs) band alignment. Similar trends are predicted by the BAC model, which considers the upward shift of both the valence and conduction bands induced by localized Sb energy levels. However, our Sb-induced band alignment variations occur with minimal Sb incorporation, suggesting new opportunities for both VBO and CBO tuning.

3.5 Conclusions

We investigated the influence of Sb incorporation on InGaAs(Sb)N/GaAs band alignment. A combination of XSTM and SIMS reveals InGaAs(Sb)N layers with compositions of $In_{0.07}Ga_{0.93}As_{0.98}N_{0.02}$ and $In_{0.043}Ga_{0.957}As_{0.975}Sb_{0.01}N_{0.015}$. STS collected across the InGaAsN/GaAs interface suggests a type II band offset, presumably due to low indium concentration and minimal strain-induced splitting of the valence band. In addition, STS reveals a type I band-offset at InGaAsSbN/GaAs interface, with VBO and CBO values consistent with those of earlier experimental reports.[11] Contrary to literature report of valence band edge tuning by Sb incorporation, the Sb-induced variation in conduction and valence band offsets is significantly larger than predicted values, suggesting the possibility of both conduction and valence band offset tuning at InGaAs(Sb)N/GaAs interfaces, with minimal Sb incorporation.

(a)

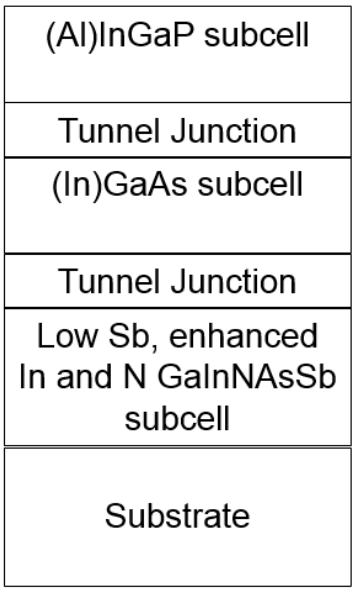

(b)

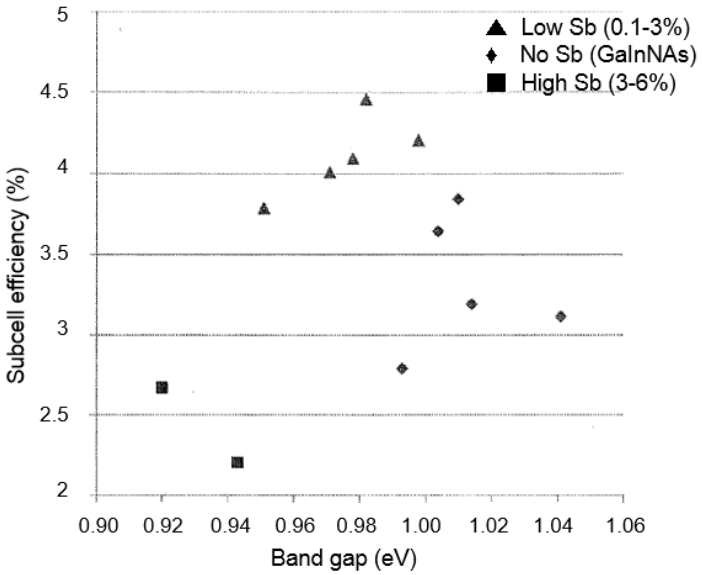

Fig. 3.1: (a) Proposed InGaAsSbN based laser heterostructucre.[13] (b) The subcell efficiency is predicted based on different band gap values assumed for the InGaAsSbN subcell. A highest subcell efficiency is predicted for InGaAsSbN layers with a band gap of approximately 1 eV.

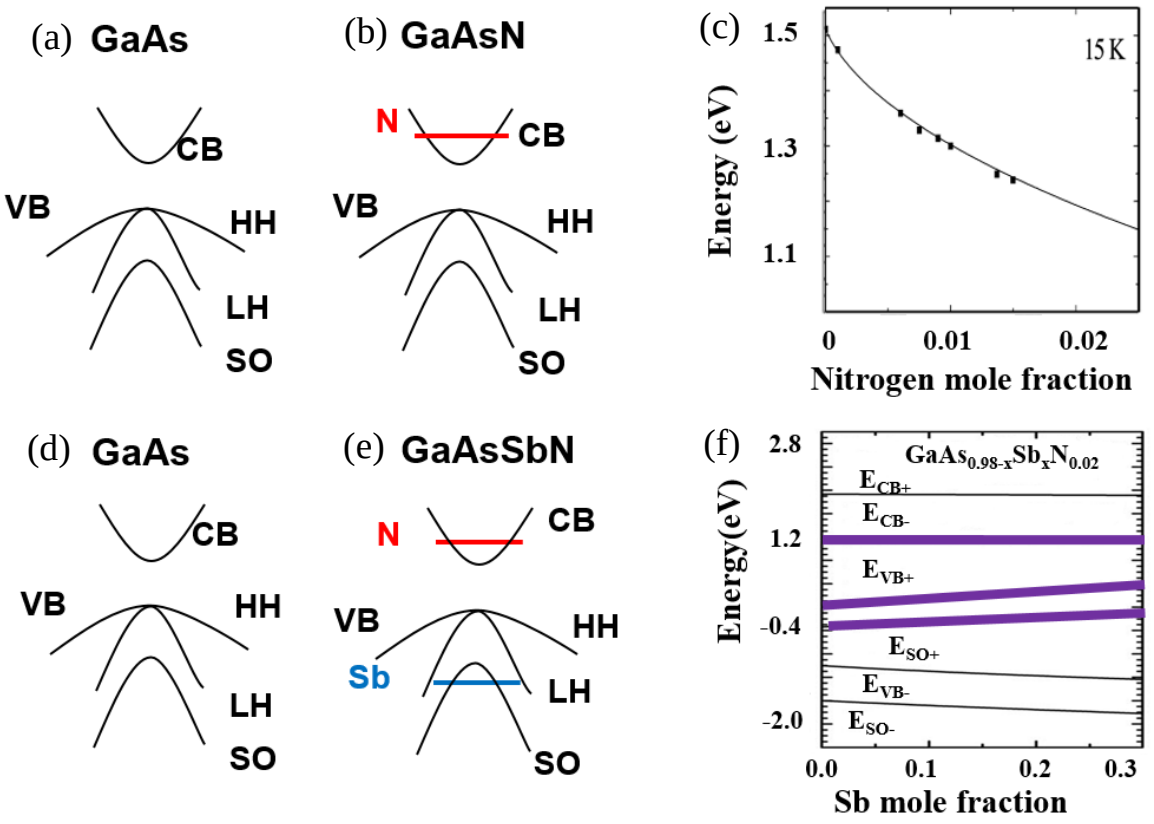

Fig. 3.2: Band anti-crossing model and the predicted band structure at (a)-(b) InGaAsN/InGaAs and (d)-(e) GaAsSbN/GaAsN interfaces. (b), (d) The red and blue lines corresponds to the nitrogen and antimony impurity state, which leads to band splitting of conduction and valence band edges, respectively. Incorporation of (c) N and (d) Sb leads to a decrease in the effective band gap energy due to the conduction and valence band splitting, respectively.[15,16]

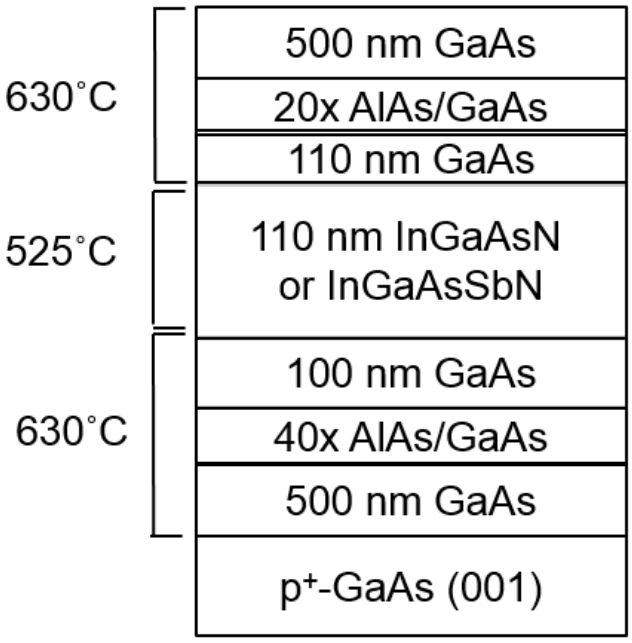

Fig. 3.3: Cross-section of the InGaAs(Sb)N heterostructure grown by TaeWan Kim at the University of Wisconsin. AlAs/GaAs superlattices would serve as a marker for locating the InGaAs(Sb)N layers during an XSTM experiment.

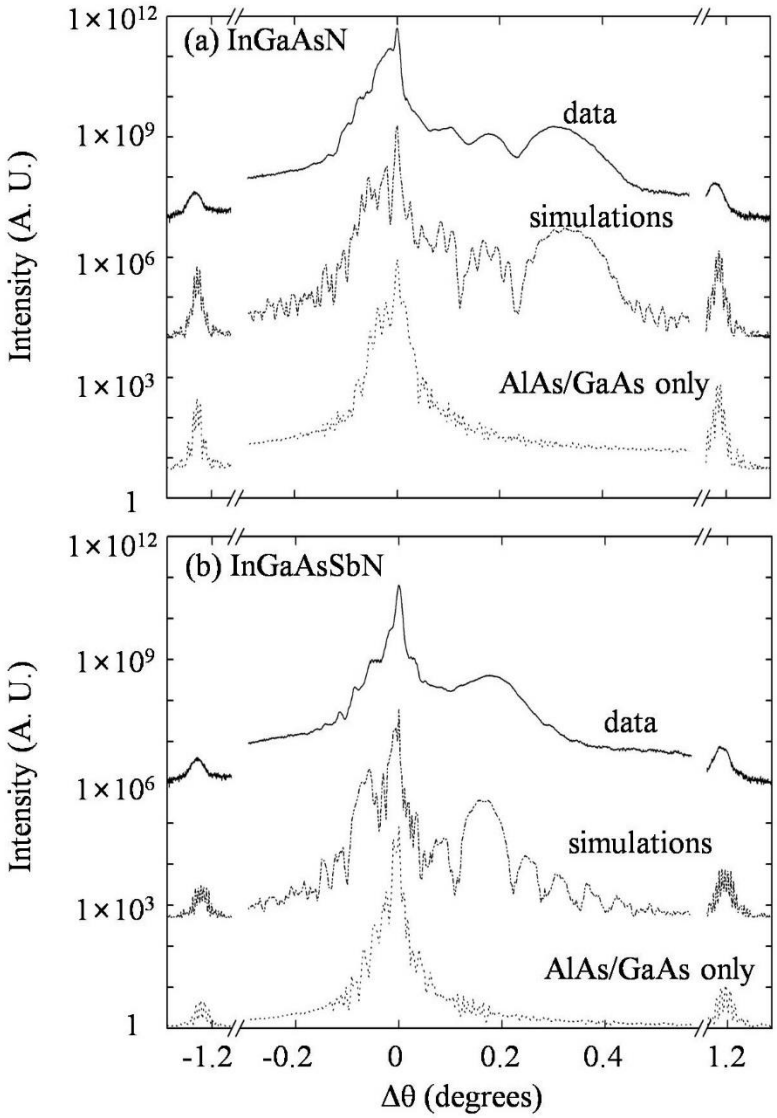

Fig. 3.4: Plots of (004) ω-2θ scans of the (a) InGaAsN and (b) InGaAsSbN based structures, in comparison with RADS simulations, with and without the InGaAs(Sb)N layers. The measured XRD spectra are plotted as solid lines, labeled "data" for both (a) InGaAsN and (b) InGaAsSbN-based structures. RADS simulations in the absence of the (a) InGaAsN and (b) InGaAsSbN layers are plotted as dotted lines, labeled "AlAs/GaAs only." Finally, plots of RADS simulations, using the concentration profiles shown in Fig. 3.5 (b) and (d), are plotted as dashed lines, labeled "simulations" in (a) and (b). Further details of the RADS simulations are discussed in Appendix D.

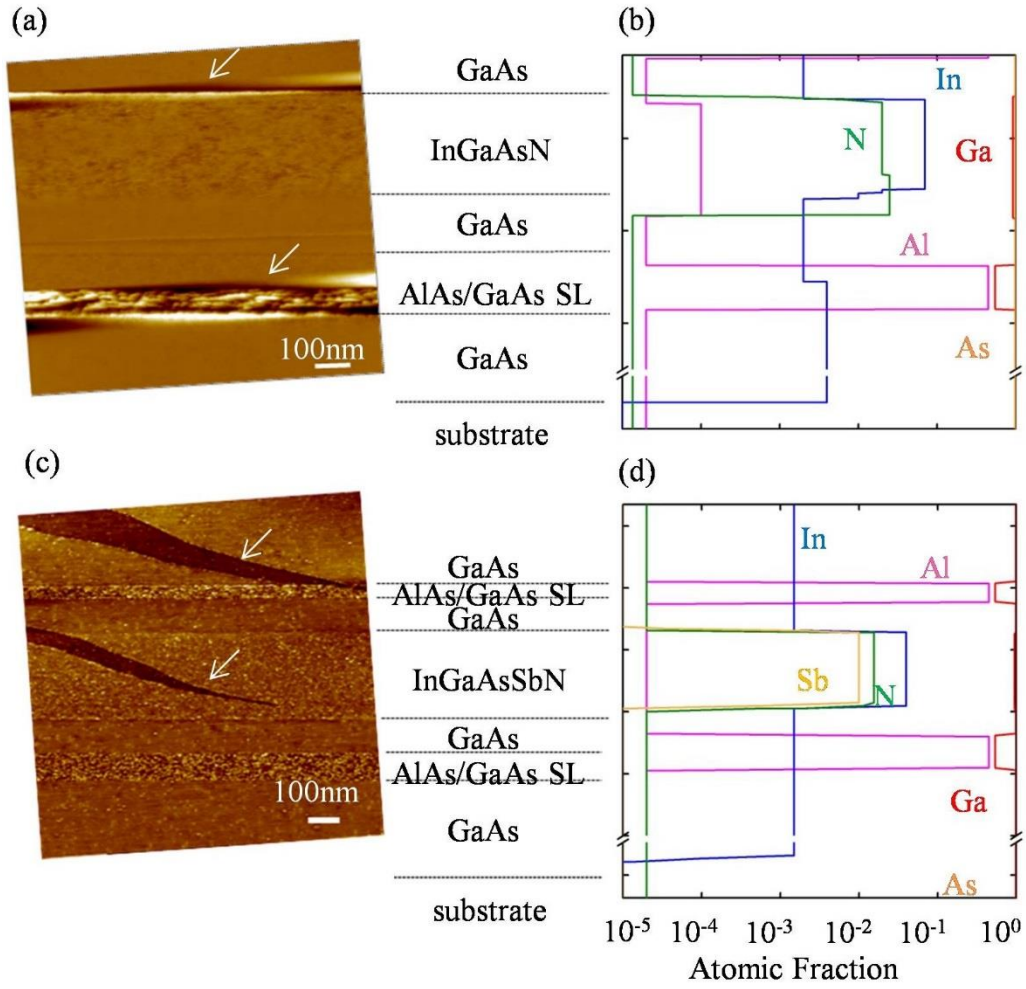

Fig. 3.5: (a) and (c) are large-scale cross-sectional XSTM images, and (b) and (d) are the compositional profiles used as input for RADS simulations of the GaAs/InGaAsN/GaAs and GaAs/ InGaAsSbN/GaAs structures, shown in Figs. 3.4 (a) and (b), respectively. The large-scale XSTM images were acquired at sample bias voltages of (a) -2.1 V and (c) +2.1 V, and the gray-scale ranges displayed are (a) 25Å and (c) 6 Å. The composition profiles include (b) indium fractions of x_{In} = 0.01, 0.02, and 0.06 and nitrogen fractions of x_N = 0.02 and 0.025 within the InGaAsN layer and (d) indium fractions of x_{In} = 0.04, nitrogen fractions of x_N = 0.015, and antimony fractions of x_{Sb} = 0.01 within the InGaAsSbN layer.

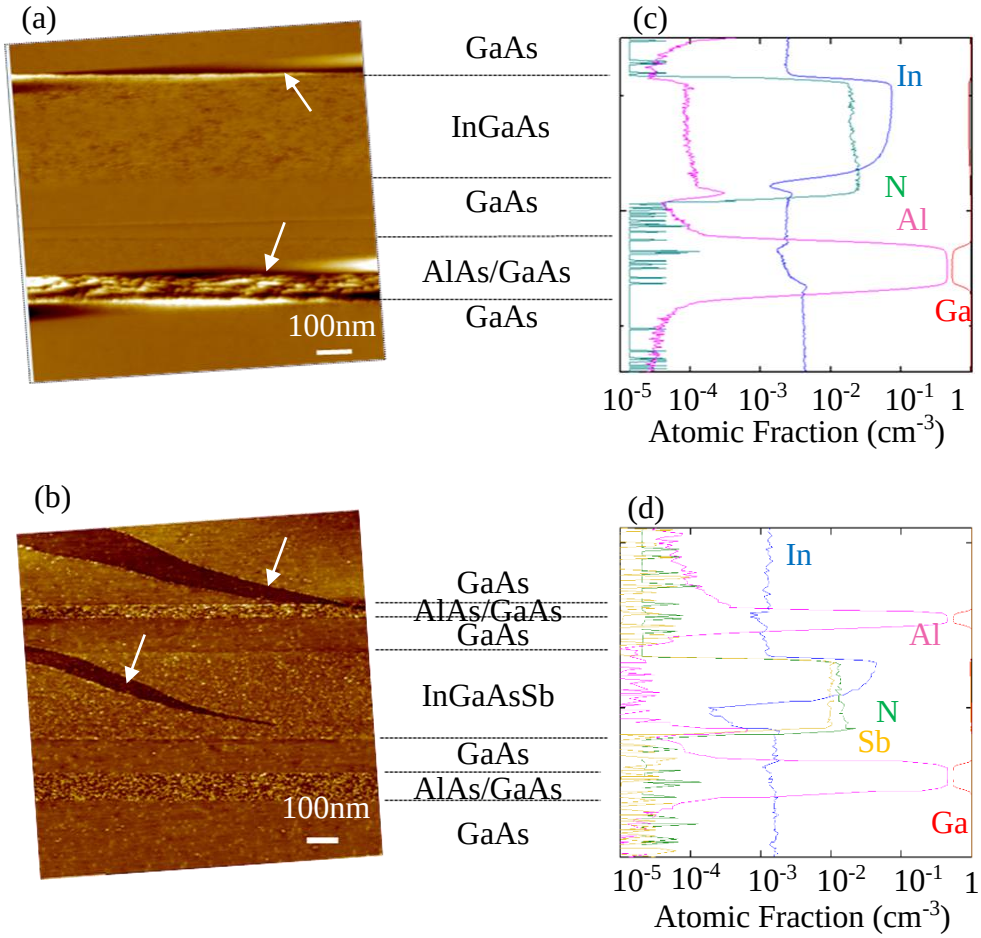

Fig. 3.6: (a) and (c) are large-scale cross-sectional XSTM images, and (b) and (d) are the secondary ion mass spectroscopy data of the GaAs/InGaAsN/GaAs and GaAs/ InGaAsSbN/GaAs structures, shown in Figs. 3.4 (a) and (b), respectively. The large-scale XSTM images were acquired at sample bias voltages of (a) -2.1 V and (c) +2.1 V, and the gray-scale ranges displayed are (a) 25Å and (c) 6 Å. In gradient in the SIMS profile is observed for both (b) InGaAsN and (d) InGaAsSbN layers is revealed.

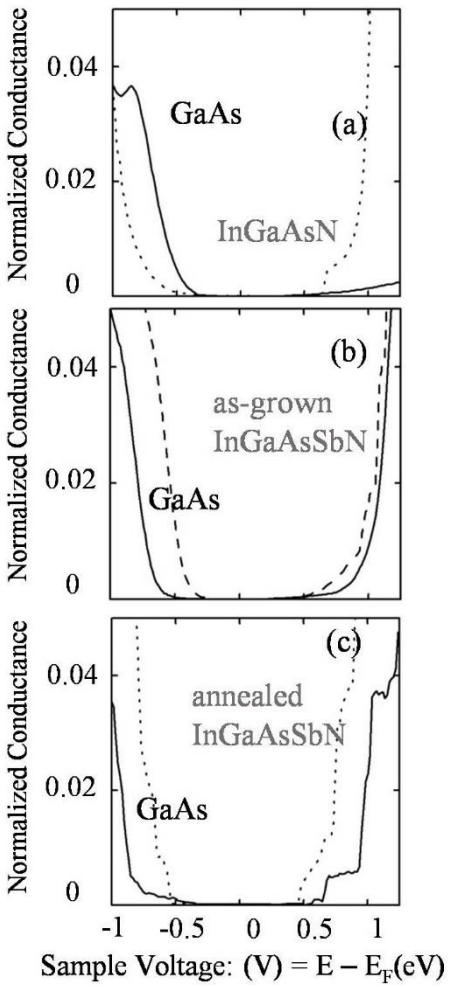

Fig. 3.7: Plots of normalized conductance versus sample bias voltage, collected from GaAs (solid line) and InGaAs(Sb)N (dotted line), for the (a) InGaAsN/GaAs, and (b) as-grown and (c) annealed InGaAsNSb/GaAs structures. The sample voltages correspond to the energy relative to the Fermi level. The effective band edges of InGaAsN are lower than those of GaAs, revealing a "nested" Type I band alignment. For both as-grown and annealed InGaAsSbN, the conduction (valence) band edges are higher (lower) than those of GaAs, revealing a "staggered" Type II band alignment.

3.6 References

[1] A. S. Chang, E. S. Zech, T. W. Kim, Y. H. Lin, L. J. Mawst, and R. S. Goldman, *Appl. Phys. Lett.* **105**, 142105 (2014).

[2]S. Sato and S. Satoh, *Jpn. J. Appl. Phys.* **38**, 1990 (1999).

[3]M. Kondow, T. Kitatani, S. Nakatsuka, M. C. Larson, K. Nakahara, Y. Yazawa, M. Okai, and K. Uomi, *IEEE J. Sel. Topics Quantum Electron.* **3**, 719 (1997).

[4]N. Tansu, J. Y. Yeh, and L. J. Mawst, *Appl. Phys. Lett.* **82**, 4038 (2003).

[5]T. Kitatani, M. Kondow, T. Kikawa, Y. Yazawa, M. Okai, and K. Uomi, Jpn. *J. Appl. Phys.* **38**, 5003 (1999).

[6]L. J. Mawst, J. Y. Huang, D. P. Xu, J. Yeh, G. Tsvid, T. F. Kuech, and N. Tansu, IEEE *J. Sel. Top.Quantum Electron.* **14**, 979 (2008).

[7]N. Tansu and L. J. Mawst, *IEEE J. Quantum Electron.* **39**, 1205 (2003).

[8]H.P. Komsa, E. Arola, and T. T. Rantala, *Appl. Phys. Lett.* **92**, 262101 (2008).

[9]T. Miyamoto, K. Takeuchi, F. Koyama, *IEEE Photon. Technol. Lett.* **9**, 11 (1997).

[10]R. Kudrawiec, H. B. Yuen, M. Motyka, M. Gladysiewicz, J. Misiewicz, S. R. Bank, H. P. Bae, M. A. Wistey, and J. S. Harris, *J. Appl. Phys.***101**, 013504 (2007).

[11]R. Kudrawiec, H. B. Yuen, S. R. Bank, H. P. Bae, M. A. Wistey, J.S. Harris, M. Motyka, and J. Misiewicz, *J. Appl. Phys.***102**, 113501 (2007).

[12]B. Gonul, K. Köksal, and E. Bakir, *Physica E* **31**, 148 (2006).

[13]R. E. Jones, H. B. Yuen, T. Liu, and P. Misra, US patent, US 2011/0232730 A1 (2011).

[14]L. J. Mawst, Juno Yu-Ting Huang, D. P. Xu, Jeng-Ya Yeh, Gene Tsvid, Thomas F. Kuech, and Nelson Tansu, *IEEE J. Sel. Topics Quantum Electron*. 14, 979 (2008).

[15]F. Bousbih, S. B. Bouzid, R. Chtourou, F. F. Charfi, J. C. Harmand, G. Ungaro, *Mater. Sci. and Engin. C* **21**, 251 (2002).

[16]Y. –T. Lin, T. –C. Ma, T. –Y. Chen, and H. –H. Lin, *Appl. Phys. Lett.* **93**, 171914 (2008).

[17]J. S. Harris, R. Kudrawiec, H. B. Yuen, S. R. Bank, H.P. Bae, M. A. Wistey, D. Jackrel, E. R. Pickett, T. Sarmiento, L. L. Goddard, V. Lordi, and T. Gugov, *Phys. Stat. Sol. (b)* **244**, 2707 (2007).

[18]R. Kudrawiec, M. Motyka, M. Gladysiewicz, J. Misiewicz, H. B. Yuen, S. R. Bank, H. Bae, M. A. Wistey, and J. S. Harris, *Appl. Phys. Lett.* **88**, 22113 (2006).

[19]S. R. Kurtz, A. A. Allerman, C. H. Seager, R. M. Sieg, and E. D. Jones, *Appl. Phys. Lett.* **77**, 400 (2000).

[20]A. Aissat, S. Naver, M. Seghilani, and J. P. Vilcot, *Physica E* **43**, 40 (2010).

[21]Rocking Curve Analysis by Dynamical Simulation, *Bede Scientific, Inc.*

[22]S. W. MacLaren, J. E. Baker, N. L. Finnegan, and C. M. Loxton, *J. Vac. Sci. Technol., A* **10**, 468 (1992).

[23]M. J. P. Hopstaken, M. S. Gordon, D. Pfeiffer, D. K. Sadana, T. Topuria, P. M. Rice, C. Gerl, M. Richter, and C. Marchiori, *J. Vac. Sci. Technol. B* **28**, 1287 (2010).

[24]B. Lita, thesis, *University of Michigan* 2002

[25]E. S. Zech, A. S. Chang, A. J. Martin, J. C. Canniff, Y. H. Lin, J. M. Millunchick, and [26]R. S. Goldman, *Appl. Phys. Lett.* **103**, 082107 (2013)

[27]B. Wilsch, U. Jahn, B. Jenichen, J. Lahnemann, H. T. Grahn, H. Wang, and H. Yang, *Appl. Phys. Lett.* **102**, 052109 (2013)

Chapter 4

Influence of Substrate on InGaN/GaN Quantum Dot Formation and Properties

4.1 Overview

Quantum dots (QDs) are nanostructures with dimensions on the order of the carrier de Broglie wavelength. The density state, which is the number of energy states at each energy level, for a QD is predicted to have a delta function-like dependence on energy. QDs are typically surrounded by a larger bandgap material to enable carrier confinement within the nanostructures. Thus, QDs are promising for electrical and optical devices due to the spatial confinement of carriers at discrete energy levels. InGaN/GaN QDs are promising for longer-wavelength device applications due to their high mobility, high absorption coefficient, and direct wide bandgap.[1-3] InGaN/GaN QDs are commonly grown either on free-standing GaN substrates or GaN/sapphire substrates. However, the influence of starting substrate on the formation and electric properties has not yet been reported.

In this chapter, we compare the formation and properties of InGaN/GaN quantum dots grown by molecular beam epitaxy on GaN/sapphire and free-standing GaN substrates. Scanning tunneling microscopy reveals the formation of indium-rich nanostructures on GaN/sapphire and QDs of various sizes on free-standing GaN substrates. Furthermore,

local scanning tunneling spectroscopy measurements reveal substrate-dependent variation in the effective band gap energy values of InGaN QDs. We discuss the influences of threading dislocation, strain, and indium segregation on the formation and band structure of InGaN/GaN QDs.

This chapter opens with an introduction to QD nucleation, followed by a description of experimental methods. Next, we report the influence of starting substrate dot dimensions, density, and band gap. Finally, we investigate the band structure of InGaN QDs with various sizes. The chapter concludes with a summary. InGaN/GaN QD heterostructure growth was performed by T. Frost and A. Hazari inat the University of Michigan. HRXRD measurements were performed by J. Occena at the University of Michigan. This research is supported by the National Science Foundation through the Materials Research and Engineering Center at the University of Michigan, under grant No. DMR-1120923.

4.2 Background

In recent years, InGaN alloys have been successfully implemented in visible light emitters and detectors.[4-5] However, longer-wavelength devices require concentrated alloys for which the misfit strain for InGaN alloys may exceed 10%. Indeed, for high In fractions, the strain-induced piezoelectric polarization is expected to limit the e^--hole overlap and the resulting optical properties of quantum well structures.[5] Schematics of band structure for InGaN/GaN QW interfaces with and without piezoelectric polarization are shown in Fig. 4.1 (a) and (b), respectively. Recently, InGaN based quantum dots with minimal strain-

induced polarization, have been demonstrated for light emitters operating in the red emission range.[2,3]

Generally, QDs form when the surface energy of a growing thin film is larger than the sum of the surface and interface energies of the film and substrate, respectively. In this case, the atoms on the surface are more strongly attracted to each other than to the surface, forming misfit strain relaxing islands. In the simplest model, QD nucleation occurs preferentially at positions of local strain minima.[6] For multi-layers of QDs, as shown in Fig. 4.2 of Tersoff's model,[6] the strain field from the buried QDs reduces the local misfit at the surface, leading to vertical stacking of QDs and an increase in the regularity of the spacing between the QDs.[6] It is important to note that the Tersoff's model is limited by assuming nucleation to occur only at the strain-induced local minimum in the misfit. For example, experimental observation of adjacent InGaN QDs, with high x_{In}, coalescing on a strain relaxed surface have been reported.[7,8]

Different substrates are reported to have different threading dislocation densities. For example, free-standing GaN substrates, which were grown and separated from Si substrates, are reported to have a threading dislocation density of ~ 10^6 /cm^2.[9] On the other hand, GaN/sapphire substrates are reported to have a larger threading dislocation density of ~ 2 x 10^8 /cm^2.[10] Furthermore, GaN/AlN interfaces are reported to have a large threading dislocation density of ~ 5 x 10^{12} / cm^2.[11] It is important to notice this difference in the threading dislocation density due to the fact that residual stresss around threading dislocations are reported to provide nucleation sites for InGaN, InN, or GaN QD systems. In the case of InGaN/GaN QDs, conflicting trends of a constant or an increase in QD density with increasing number of QD SLs have been reported, depending on the starting

substrate, as shown in Fig. 4.3.[12-14] Furthermore, variations in the QD dimensions and their band gap energies for similar indium mole fractions have been reported, as shown in Table 4.1.[15-22]

4.3 Experimental Details

The samples were grown by molecular-beam epitaxy (MBE) using solid Ga and In sources, with an ultra-high purity N_2 plasma source. Single layer InGaN/GaN QD SL, consisting of 8 monolayers (MLs) InGaN quantum dots (QDs) and 12nm GaN capping layers, were grown on free-standing n^+ GaN (001) substrates, which are grown on and separated from Si substrates, with expected threading dislocation density ~ 10^6 /cm^2.[9] Single layer and three-layer InGaN/GaN QD SLs, with a target x_{In} of 0.4, were grown on n^+ GaN/sapphire, with reported threading dislocations density ~ 2 x 10^8 /cm^2.[10] For all cases, the GaN buffer layers were grown at a substrate temperature of 710 °C with a Ga flux of 2.2 x 10^{-7} Torr and N_2 flow rate / plasma power of 0.66 sccm / 350 W. The InGaN QDs were grown at a substrate temperature of 540 °C, with a Ga flux of 4 x 10^{-8} Torr, In flux of 9 x 10^{-8} Torr, and N_2 flow rate / plasma power of 1.33 sccm / 420 W. All layers, except the InGaN QDs, were n+ Si-doped at ~5 x 10^{18}/cm^3. We will refer to the single layer InGaN/GaN QD SL as "QD-GaN", the single layer InGaN/GaN QD SL as "QD-GaN/sapphire", and the three-layer InGaN/GaN QD SLs as "multi-QD-GaN/sapphire".

Furthermore, InGaN/GaN QD heterostructures for XSTM studies were grown with a 500 nm GaN capping layer on free-standing GaN substrates. However, due to the difficulty in obtaining an atomically flat cleave in the vicinity of InGaN QDs, only few

XSTM and STS data were collected, which are presented in Chapter 6.2.2 as a future work. We note that additional unintentionally-doped heterostructures, consisting of 7-layer stacks of QDs, were grown for photoluminescence (PL) measurements. PL measurement of heterostructures grown on GaN/sapphire substrate revealed an emission peak at 1.96 eV, while PL measurement of heterostructures grown on free-standing GaN substrate revealed an emission peak at 1.89 eV. High-resolution X-ray Diffraction (HRXRD) measurements were performed using $CuK_{\alpha 1}$ radiation monochromated by a four-reflection monochromator that employs Ge (220) reflections.

In preparation for plan-view STM, InGaN/GaN QD samples were transferred from the MBE chamber via a vacuum desiccator system (~ 10^{-2} Torr) to the STM chamber. During the transfers between the MBE or STM chambers to the mobile transfer system, the samples were exposed to air for less than a minute. Samples from the load lock of the MBE chamber were transferred to the vacuum desiccator system and pumped down immediately. Samples were then transferred from the vacuum desiccator to the STM sample holder in a laminar hood. Samples were stored in the nitrogen gas over-pressured load lock of the STM chamber, which was pumped down with a turbo pump.

Both scanning tunneling microscopy (STM) and STS were performed with commercially available W and Pt/Ir tips, which were cleaned in situ by electron bombardment. STS measurements were performed using the variable tip-sample separation method.[24,25] All images were obtained with a sample bias voltage of -3.5 V and constant tunneling current of 200 pA. We examined several XSTM images spanning > 1 μm^2 and acquired STS spectra in the vicinity of various InGaN nanostructures.

4.4 HRXRD data on InGaN/GaN QDs

The HRXRD data from (002) ω-2θ scans of QD-GaN, QD-GaN/sapphire, and multi-QD-GaN/sapphire, in comparison with Rocking Curve Analysis by Dynamical Simulation (RADS)[26] are shown in Fig. 4.4 (a), 4.4 (b), and 4.4 (c), respectively. For all cases, the XRD data are plotted as solid black lines and labeled "data", while the RADS results are plotted as red dashes and labeled as "sim". The GaN substrate peak position is arbitrarily set to $\Delta\theta = 0$ arcsec, thereby facilitating comparison of Bragg angle differences between the substrate and epilayers. For QD-GaN, the XRD spectra include InGaN QD peak at approximately $\Delta\omega \approx -0.02°$, as shown in Fig. 4.4 (a). Analysis of a series of $\Delta\omega$-2θ scans collected near the GaN (002) reflection suggests formation of fully relaxed $In_{0.4}Ga_{0.6}N$ QDs for QD-GaN. The predicted x_{In} agrees well with the target x_{In} for MBE growth. For QD-GaN/sapphire, the XRD spectra and RADS simulation, as shown in Fig. 4.4 (b), reveal an InGaN QD peak at $\Delta\theta \approx -0.02°$, suggesting the formation of fully relaxed $In_{0.43}Ga_{0.57}N$ QDs. The predicted x_{In} is slightly larger than the target x_{In} for MBE growth, most likely due to the formation of InN QDs, which will be discussed in Chapter 4.6. For multi-QD- GaN/sapphire, the XRD spectra, as shown in Fig. 4.4 (c), include InGaN QD peak at approximately $\Delta\theta \approx -0.16°$ and 1st order satellite peaks at approximately $\Delta\theta \approx -0.5°$ and 0.27°. Comparing the HRXRD data with RADS simulations, best agreement is found when an indium gradient is assumed, as an RADS input, for the first layer of InGaN QW, suggesting indium segregation between the QD and spacer layers. HRXRD data with RADS simulations also suggests formation of 0.57% compressively strained $In_{0.4}Ga_{0.6}N$ QDs. For both the QD- and multi-QD-GaN/sapphire, XRD spectra reveal a peak at

approximately $\Delta\theta = 0.70°$, corresponding to the mismatch between the thick GaN and $Al_{0.8}Ga_{0.2}N$ layers on sapphire.

4.5 Influence of Starting Substrate on Dot Dimensions, Density

Figure 4.5 shows large-scale STM images of (a) QD-GaN, (b) QD-GaN/sapphire, and (c) multi-QD-GaN/sapphire. Within each QD SL, bright (dark) regions corresponding to InGaN (GaN) are apparent. In Fig. 4.5 (a), large-scale STM image of a single layer on GaN reveal formation of nanostructures with a ~10 nm width, ~50 nm length, and ~ 6 nm height, resembling a quantum dash or two large adjacent InGaN QDs. Based on the STM image shown in Fig. 4.5 (a), the InGaN QD density is estimated to be 1.6×10^{10} /cm^2, using the dot size analysis described in Appendix B.

In contrast, the STM image of QD-GaN/sapphire reveals formation of InGaN QDs with a binomial size distribution, as shown in Fig. 4.5 (b). The larger (smaller) InGaN QDs have an average diameter of 21 nm (3 nm) and height of 3 nm (1.5 nm), respectively. The InGaN QD density is estimated to be 1.7×10^{11} /cm^2. As shown the STM image from multi-QD-GaN/sapphire, a significantly smaller average QD diameter (5 nm) and height (3 nm), with a dot density of 1.8×10^{12} /cm^2. It is interesting to note that the InGaN QDs from QD-GaN/sapphire have a smaller dimension compared to the case of QDs from QD-GaN. Due to the nucleation of smaller QDs with higher indium fraction, less indium incorporation into larger InGaN QDs most likely contributed to the smaller dimension compared to those from QD-GaN. Contrary to our results, an experimental study reports multi-layer GaN QDs on AlN with binomial height distribution, where the larger (smaller) QDs of average height

of 3.6 nm (1.6 nm) are nucleated near (away from) the threading dislocations.[14] It is most likely that the higher density of threading dislocations, reported to be 5 x 10^{12} /cm^2,[14] at the GaN/AlN interface provided a larger number of nucleation sites such that nearby QDs around threading dislocations merged to form a larger QD. Comparing the QD density from QD- and multi-QD-GaN/sapphire, a trend of increasing QD density with increasing number of InGaN/GaN QD SL layers agrees well with literature reports of similar and larger sized QDs.[6,12] The accumulation of strain from layers beneath most likely lead to nucleation of QD at the space above and between the existing QDs beneath, leading to a larger density and a smaller diameter of InGaN QDs.[22]

4.6 Influence of Starting Substrate on Band Gap

Figure 4.6 presents plots of normalized conductance versus sample voltage collected from the (a) QD-GaN, (b) QD-GaN/sapphire, and (c) multi-QD-GaN/sapphire. In all cases, the data was collected in the vicinity of the InGaN nanostructures. In all spectra, the sample voltage corresponds to the energy relative to the Fermi level. Indeed, the GaN spectra, shown as the solid-line spectra in Figs. 4.6 (a) – 6 (c), display well-defined band edges, with effective GaN band gap values of 3.4 ± 0.1 eV, similar to that of bulk GaN at room temperature.

The effective band gaps of the STS taken in the vicinity of the InGaN nanostructures are lower than those of GaN, consistent with literature reports of decreasing effective band gaps with increasing indium fraction due to indium-induced conduction band lowering. For the QD-GaN, STS reveals effective band gaps of 2.1 ± 0.1 eV, 2.8 ±

0.1 eV, and 3.2 ± 0.1 eV taken at the center, inner edge, and outer edge of the InGaN nanostructure, as indicated in Fig. 4.6(a). Interestingly, as shown in Fig. 4.7, the effective band gaps of the STS taken along the elongated direction of the nanostructure also reveal a variation in the band gap, suggesting that the nanostructure is indeed two adjacent QDs, similar to reported InGaN QDs with high x_{In}.[8,9] It is more likely that two QDs nucleated near each other and coalesced. The band gap value at the center of the QD agrees well with our 2.0 eV emission peak of PL measurement.

For the QD- and multi-QD- GaN/sapphire, STS revels effective band gaps of 2.5 ± 0.1 eV and 3.0 ± 0.1 eV at the center and edge of the InGaN QD, respectively. In addition, STS collected on small nanostructures of an average 3 nm diameter reveal an effective band gap of 1.2 ± 0.1 eV, suggesting that that these nanostructures are indium-rich with x_{In} ~ 0.8. The value of effective band gap energy at the QD center, 2.5 eV, is significantly larger than that of QDs from QD-GaN, 2.1 eV. Literature reports difficulty in the QD nucleation near a threading dislocation when the indium content is above 0.8, leading instead to the formation of indium clusters, while InN QDs are reported to nucleate near threading dislocations.[14,27] Experimental measurements on the InN QDs, contrary to the reported band gap of 0.66 eV for Wurtzite structure, reveals a band gap of 1.1 eV due to quantum confinement.[28] Furthermore, due to the formation of InN QDs near the threading dislocations, it is likely that there was less indium incorporation for InGaN QDs, leading to a smaller band gap energy value. Experimental reports on $In_{0.2}Ga_{0.8}N$ QDs of ~25 nm diameter and 6 nm height also reveal a smaller effective band gap of 2.7 eV for QDs from QD-GaN than the effective band gap of 2.4 eV for QDs from QD-GaN/Sapphire.[17,20]

For the multi-QD-GaN/sapphire, STS revels effective band gaps of 2.2 ± 0.1 eV and 3.2 ± 0.1 eV at the center and edge of the InGaN QD, respectively. Interestingly, at the center of the QD, the effective band gap of QDs is smaller for the multi-QD-GaN/sapphire in comparison to that of QD-GaN/sapphire. Due to the accumulation of strain from InGaN QDs buried below, a vertical stacking of QDs and an increase in the regularity of the spacing between the QDs lead to new nucleation sites with similar indium composition at the center. Furthermore, indium-rich nanostructures with band gap energy values ~1.2 eV were not observed, suggesting that the strain-field from buried QDs is dominant over the strain field around the threading dislocation for QD nucleation.

4.7 Band Alignment of InGaN/GaN QDs

We now discuss the effective valence and conduction band offsets in the vicinity of InGaN nanostructures. For QD-GaN, QD-GaN/sapphire, and multi-QD-GaN/sapphire, the effective conduction band offsets at InGaN/GaN QDs are 1.2 eV, 0.8 eV, and 1.1 eV, as shown in Figs. 4.6(a), 4.6(b), and 4.6(c), respectively. Furthermore, a gradient in the conduction band edge is observed, with the effective bandgap decreasing laterally toward the InGaN QD core, consistent with observations in InAs/GaAs systems.[29] It is most likely that significant In segregation in the center of the dot column resulted in a gradient in x_{In} across the InGaN QD. Since the band gap energy at the edge of the InGaN QD is smalled for QD-GaN/sapphire case, a minimum strain-induced indium segregation is suggested for InGaN QD nucleation in the presence of threading dislocations. In addition, the valence band edges of STS taken in the InGaN QD were independent of spatial position with values

similar to that of GaN. On the other hand, it is reported that incorporation of indium lowers the effective conduction band edge. Thus, an indium gradient within the InGaN QD is suggested, with higher x_{In} at the center of the QD. As a comparison, we used an reported In composition profile of a similar-sized QDs to estimate the conduction and valence band edges of an undoped, bulk-like InGaN alloy are plotted and shown as solid line in Figs. 4.7.[30-33] In the InGaN QD, the lowest confined electron and hole energy levels are expected to be higher in energy than the band edges of bulk InGaN. The higher (similar) energy values of the measured E_e (E_h) compared to the band edges of bulk InGaN indicates a carrier confinement of electrons for the large InGaN QDs.

4.8 Conclusions

In summary, we investigated the InGaN QD formation of various sizes and band gap energy values grown on different substrates by MBE. For QD-GaN, a combination of STM and STS reveals formation of randomly distributed QDs with a low dot density, most likely influenced by initial growth morphology. In the case of QD-GaN/sapphire, we report formation of InGaN and InN QDs with densities estimated to be at least one order of magnitude larger than that of QDs from QD-GaN. For multi-QD-GaN/sapphire, STM and STS reveal a high quantum dot density and regularly spaced QDs. However, InN QD nucleation is not observed for multi-QD-GaN/sapphire, suggesting that QD formation is dominantly driven by the strain field from the buried QDs rather than the threading dislocation. Furthermore, the effective band gap energy values at the center of the InGaN QD is lower for single layer on GaN/sapphire compared to the other cases due to indium-

rich nanostructure formation. STS collected across the InGaN QD reveal a gradient in the effective band gap energy values, decreasing laterally toward the QD center. Our work suggests that a wide variety of InGaN QD dimension, density, and band structure can be achieved by using different starting substrate and number of layers of InGaN QD stacks.

Nanostructure	Characterization/Theory	x_{In}	E_g
QW	cathodoluminescence spectroscopy	0.18	2.7 eV [19]
QW	PL	0.3	2.63 eV [15]
QW	PL	0.31	2.75 eV [22]
QW	PL	0.4	1.8 eV [18]
QD	Deformation potential	0.18	2.7 eV [20]
QD	PL	0.2	2.3 eV [16]
QD	PL	0.25	2.5 eV [17]
QD	PL	0.3	2.34 eV [23]
QD	Finite element method	0.4	2.55 eV [21]

Table 4.1: Table summarizing reported band gap energies of InGaN quantum wells (QWs) and quantum dots (QDs) of various x_{In}.[15-23] Photoluminescence is denoted as PL. Variations in the InGaN QD band gap energies for similar indium mole fractions and QD dimension have been reported. In general, the InGaN QDs grown on free-standing GaN substrates had smaller band gap energies compared to those grown on GaN/sapphire.

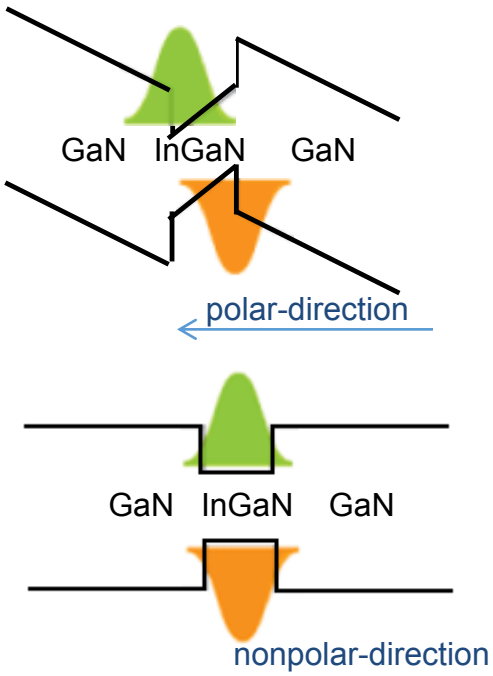

Fig. 4.1: Schematic band structure of GaN/InGaN/GaN interfaces (a) with and (b) without piezoelectric polarization. For InGaN/GaN interfaces with strong polarization, spatial separation of electron and hole wavefunctions are expected. For InGaN/GaN interfaces with no polarization, the electron and hole wavefunctions are spatially overlapped, leading to an increase in electron-hole recombination rate.[5]

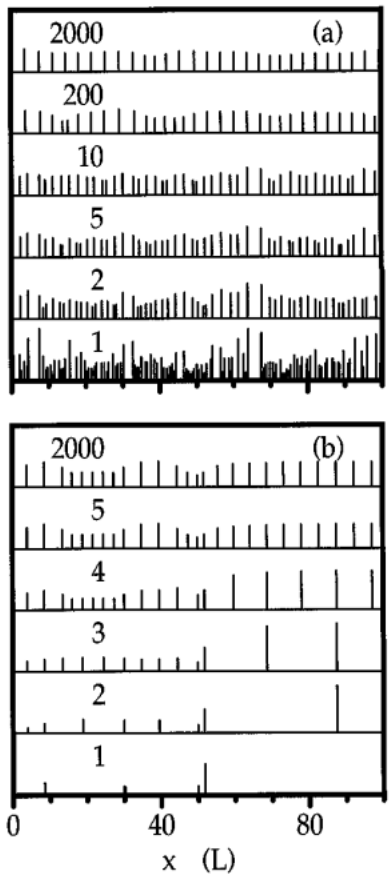

Fig. 4.2: Calculated island positions and sizes in multi-layer QDs. Unit L represents the QD spacer thickness. The number of QD layers are indicated within the figure. Heights of vertical lines represent the relative island volumes. Sequences begin with (a) closely spaced islands and (b) widely spaced islands.[6] The strain field from the buried QDs reduces the local misfit at the surface, leading to vertical stacking of QDs and an increase in the regularity of the spacing between the QDs.

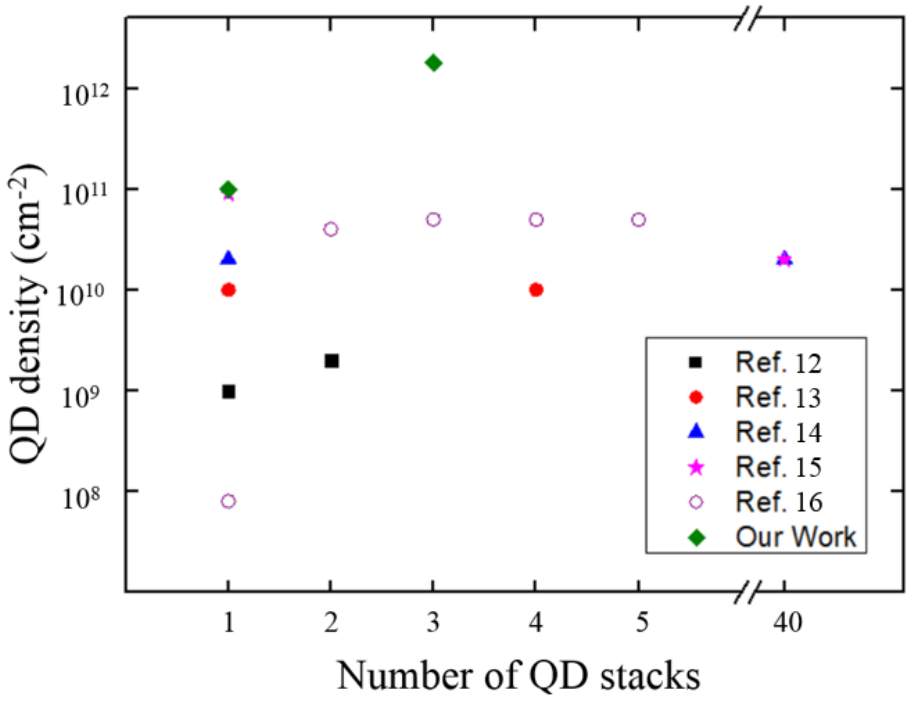

Fig. 4.3: Reported InGaN QD density as a function of number of QD stacks. Conflicting trends of a constant or an increase in QD density with increasing number of QD SLs have been reported, depending on the starting substrate.[12-16] Increase in the QD density with increasing number of QD stacks agrees with the Tersoff's model, which predicts dot nucleation due to strain field from the buried QDs.[12,15,16] On the other hand, few experimental reports present a constant QD density with increasing number of QD stacks, most likely due to QD nucleation by other sources, such as phase separation of indium and residual stress from threading dislocations.[13,14]

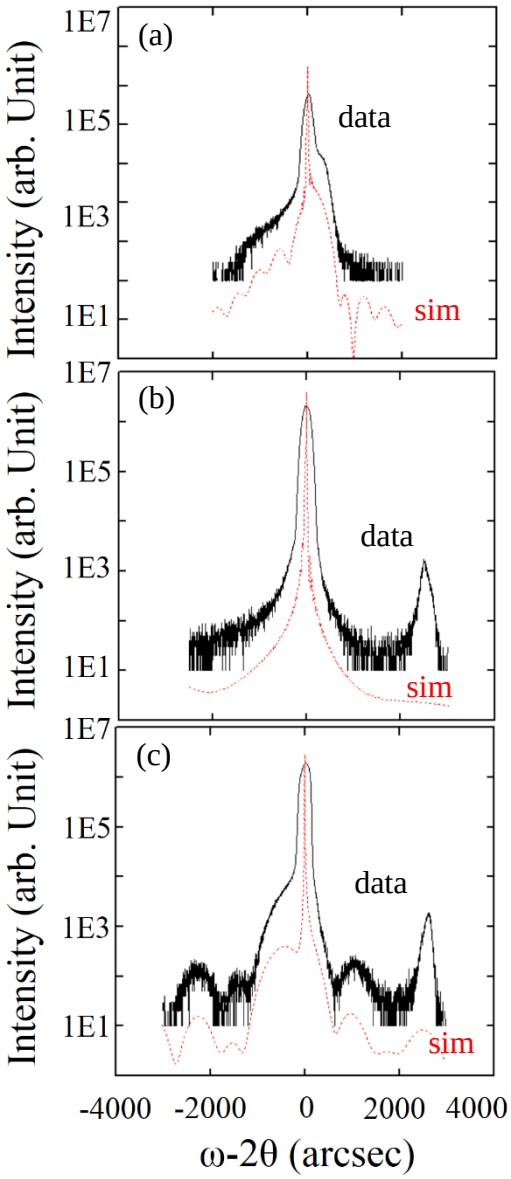

Fig. 4.4: Diffraction intensity plotted as a function of Δω for (a) QD-GaN, (b) QD-GaN/sapphire, and (c) multi-QD-GaN/sapphire collected near the GaN (002) reflection during X-ray diffraction measurements, in comparison with RADS simulations. For all cases, the measured XRD spectra are plotted as black line, labeled "data". RADS simulations are labeled as "sim", respectively.

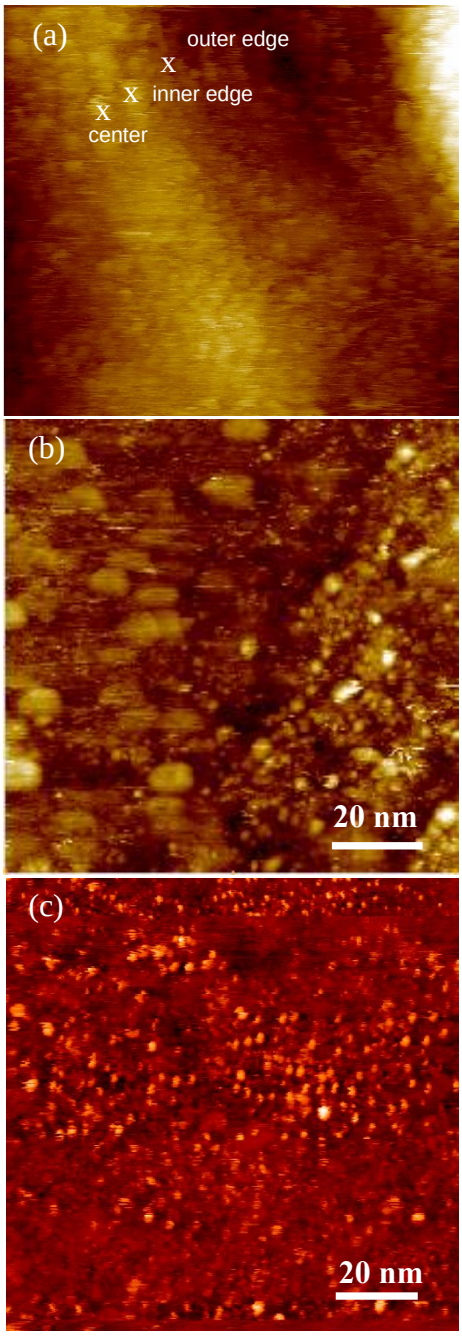

Fig. 4.5: Large-scale STM images of (a) QD-GaN, (b) QD-GaN/sapphire, and (c) multi-QD-GaN/sapphire. The images were acquired at a sample bias voltage of -3.5 V; the greyscale ranges displayed are (a) 15 nm, (b) 8 nm, and (c) 5 nm, respectively.

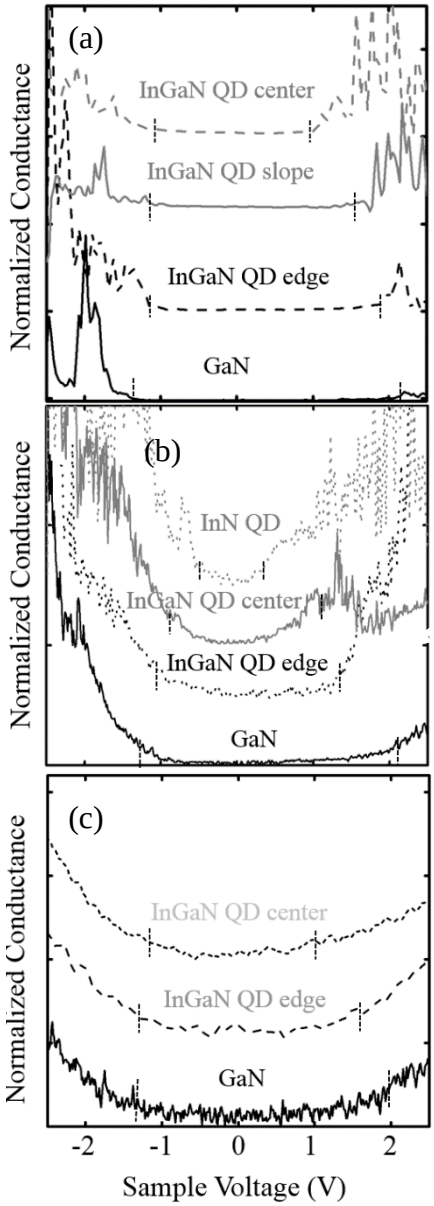

Fig. 4.6: Plots of normalized conductance versus sample bias voltage, collected from GaN and around InGaN QDs from (a) QD-GaN, (b) QD-GaN/sapphire, and (c) multi-QD-GaN/sapphire. STS reveals effective band gaps of 3.4 eV for GaN, which agrees well with the reported value. The effective band gaps at the center of the QD are significantly smaller than the band gaps at the edge of the QD. (b) For QD-GaN/sapphire, STS reveals an effective band gap of 1.2 eV around the InN QDs due to quantum confinement.

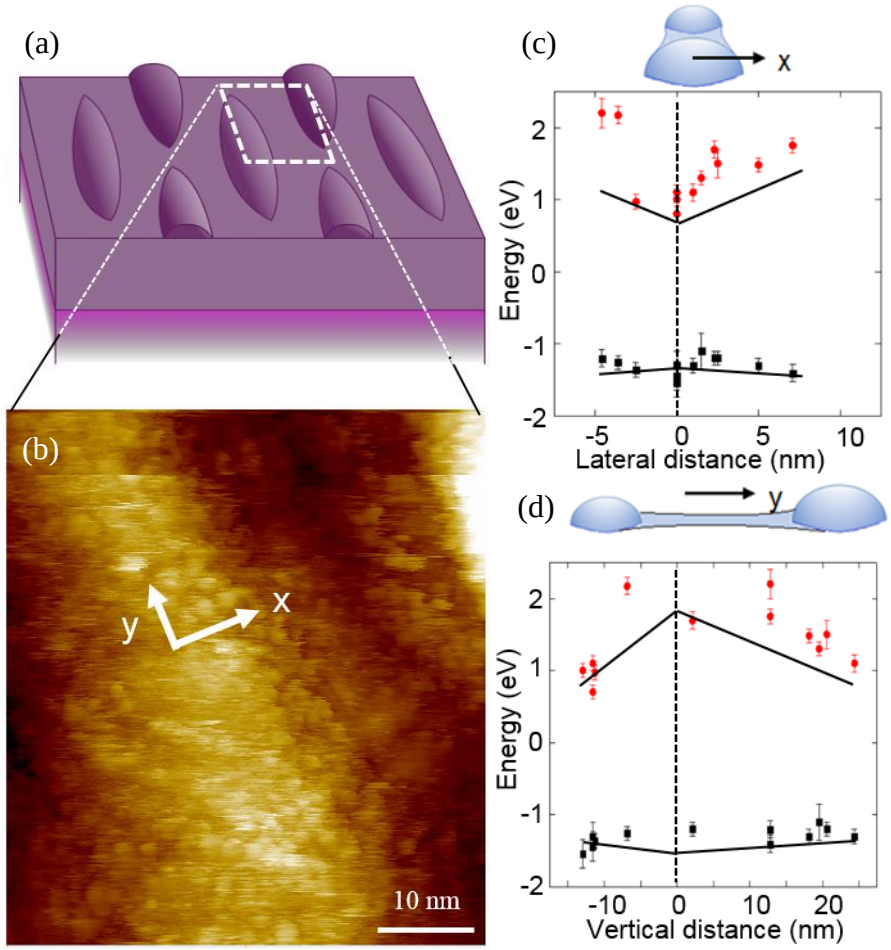

Fig. 4.7: (a) schematic and (b) STM image of QD-GaN surface. Plots of valence and conduction band edges versus (c) lateral and (d) vertical distances across the InGaN nanostructure, as indicated within the figure, are plotted as red and black dots, respectively. Across the lateral direction of the InGaN nanostructure, the valence band edge is similar to that of GaN, while a decreasing gradient in the conduction band edge towards the center of the dot is observed. In addition, a significant change in the conduction band edge across the vertical direction of the InGaN QD is observed, suggesting the nanostructure to be two adjacent large InGaN QDs.

4.9 References

[1]Y. Enya, Y. Yoshizumi, T. Kyono, K. Akita, M. Ueno, M. Adachi, T. Sumitomo, S. Tokuyama, T. Ikegami, K. Katayama, and T. Nakamura, *Appl. Phys. Exp.* **2**, 082101 (2009).

[2]T. Frost, A. Banerjee, S. Jahangir, and P. K. Bhattacharya, *Appl. Phys. Lett.* **104**, 081121 (2014).

[3]S. Jahangir, T. Frost, A. Hazari, L. F. Yan, E. Stark, T. LaMountain, J. M. Millunchick, B. S. Ooi, P. Bhattacharya, *Appl. Phys. Lett.* **106**, 071108 (2015).

[4]S. Nakamura, M. Senoh, N. Iwasa, and S. Nagahama, *Jpn. J. Appl. Phys.* **34**, L797 (1995).

[5]S. Nakamura, M. Senoh, S. Nagahama, N. Iwasa, T. Yamada, T. Motsushita, Y. Sugimoto, and H. Kuyoku, Appl. Phys. Lett. 69, 4056 (1996).

[6]J. Tersoff, C. Teicher, and M. G. Lagally, *Phys. Rev. Lett.* **76**, 1675 (1996).

[7]W. Zhao, L. Wang, W. Lv, L. Wang, J. Wang, Z. Hao, and Y. Luo, *Jap. J. of Appl. Phys* **50**, 065601 (2011).

[8]R. –C. Tu, C. –J. Tun, C. –C. Chuo, B. –C. Lee, C. –E. Tsai, T. –C. Wang, J. Chi, C. –P. Lee, and G. –C. Chi, *Jap. J. of Appl. Phys* **43**, L264 (2004).

[9]K. Kojima, Y. Tsukada, E. Furukawa, M. Saito, Y. Mikawa, S. Kubo, H. Ikeda, K. Fujito, A. Uedono, and S. F. Chichibu, *Appl. Phys. Exp.* **8**, 095501 (2015).

[10]S. D. Lester, F. A. Ponce, M. G. Craford, D. A. Steigerwald, *Appl. Phys. Lett.* **66**, 1249 (1995).

[11]Z. C. Feng, *"III-Nitride Devices and Nanoengineering", World Scientific Publishing Company* (2008).

[12]W.B. Lv, L. Wang, J. X. Wang, Z. B. Hao, , and Y. Luo, *Chin. Phys. Lett.* **28**, 128101 (2011).

[13]J. K. Rouviere, J. Simon, N. Pelekanos, B. Daudin, and G. Feuillet, *Appl. Phys. Lett.* **75**, 2632 (1999).

[14]T. D. Moustakas, T. Xu, C. Thomidis, A. Y. Nikiforov, L. Zhou, and D. J. Smith, *Phys. Stat. Sol. (a)* **205**, 2560 (2008).

[15]S. R. Meher, A. Subrahmanyam, and Mahaveer K. Jain, *J. Mater. Sci.* **48**, 1196 (2013).

[16]S. C. Davies, D. J. Mowbray, F. Ranalli, and T. Wang, *Appl. Phys. Lett.* **96**, 251904 (2010).

[17]M. Zhang, P. Bhattacharya, and W. Guo, *Appl. Phys. Lett.* **97**, 011103 (2010).

[18]M. Millot, Z. M. Geballe, K. M. Yu, W. Walukiewicz, and R. Jeanloz, *Appl. Phys. Lett.* **100**, 162103 (2012).

[19]B. Wilsch, U. Jahn, B. Jenichen, J. L€ahnemann, H. T. Grahn, H. Wang, and H. Yang, *Appl. Phys. Lett.* **102**, 052109 (2013).

[20]G. –L. Su, T. Frost, P. Bhattacharya, J. M. Dallesasse, and S. L. Chuang, *Opt. Soc. of Amer.* **22**, 19 (2014).

[21]W. –Y. Tsai, K. –B. Hong, and M. –K. Kuo, *Phys. Stat. Soli.* **B** 247, 7 (2010).

[22]H. K. Cho, J. Y. Lee, J. H. Song, P. W. Yu, G. M. Yang, and C. S. Kim, *J. of Appl. Phys.* **91**, 1104 (2002).

[23]J. Bai, Q. Wang, T. Wang, A. G. Cullis, and P. J. Parbrook, *J. of Appl. Phys.* **105**, 053505 (2009).

[24]B. Lita, *thesis*, *University of Michigan* 2002.

[25]E. S. Zech, A. S. Chang, A. J. Martin, J. C. Canniff, Y. H. Lin, J. M. Millunchick, and R. S. Goldman, *Appl. Phys. Lett.* **103**, 082107 (2013).

[26]Rocking Curve Analysis by Dynamical Simulation, *Bede Scientific, Inc*.

[27]J. G. Lozano, A. M. Sánchez, R. García, D. González, D. Araújo, S. Ruffenach, and O. Briot, *Appl. Phys. Lett.* **87**, 263104 (2005).

[28]Y. –R. Lyu and T. –E. Hsieh, *ECS J. of Sol. State Sci. and Technol.* **3**, R258 (2014).

[29]V. D. Dasika, A. V. Semichaevsky, J. P. Petropoulos, J. C. Dibbern, A. M. Dangelewicz, M. Holub, P. K. Bhattacharya, J. M. O. Zide, H. T. Johnson, and R. S. Goldman, *Appl. Phys. Lett.* **98**, 141907 (2011).

[30]T. -C. Wang, H. –C. Kuo, T. –C. Lu, C. –E. Tsai, M. –Y. Tsai, J. –T. Hsu, and J. –R. Yang, *Jpn. J. of Appl. Phys*. **45**, 2560 (2006).

[31]C. G. Van de Walle and J. Neugebauer, *Appl. Phys. Lett.* **70**, 19 (1997).

[32]Y. –K. Kuo, W. –W. Lin, and J. Lin, *Jpn. J. Appl. Phys.* **40,** 3157 (2001).

[33]S. Pereira, M. R. Correia, T. Monteiro, E. Pereira, E. Alves, A. D. Sequeira and N. Franco, *Appl. Phys. Lett.* **78**, 2137 (2001).

Chapter 5

Influence of Strain and Dislocation on the GaSb/GaAs Band Offsets

5.1 Overview

Advances in quantum dot (QD) devices will require an understanding of the influence of strain and dislocations on the band structure. The electronic properties of QDs in the presence of strain and dislocations is one of the least understood aspect of QD heterostructures. However, the strain and dislocation dependence of structural and electrical properties of a QD system is difficult to quantify with experimental methods, and thus should be investigated in combination with computational methods. This chapter begins with a brief review of prior work with conflicting reports of type I vs type II band alignments across GaSb/GaAs QD interface. Furthermore, literature reports of power-dependent PL blue shift in GaSb/GaAs heterostructures are present. HRXRD, XSTM, and STS are utilized for investigating the band alignment at GaSb/GaAs QDs grown on different GaAs surface terminations. Then, XSTM, APT, and PL experiments on SK and IMF GaSb QDs are summarized. The computational work for investigating the influence of mismatch, dislocation, dislocation charging on the band alignment at GaSb/GaAs interface is presented.

GaSb/GaAs QDs on different growth surfaces were grown by A. Martin in Prof. Millunchick's group at the University of Michigan. SK and IMF GaSb QDs were grown by S. Clark in Prof. G. Balakrishnan's group at the University of New Mexico. XTEM, XSTM, and STS experiments on GaSb/GaAs QDs on different surface termination was performed by a previous group members, J. Canniff and E. Zech, and the author of this dissertation. APT and PL measurements of SK and IMF GaSb QDs were performed by E. Zech at the University of Michigan and M. Luengo-Kovac in Prof. G. Balakrishnan's group at the University of New Mexico. Finally, calculations of band structure of GaSb/GaAs QD interfaces were performed by B. McGuigan in Prof. H. Johnson's group at the University of Illinois. This work is supported by the U.S. Department of Energy, Office of Science, Office of Basic Energy Sciences, under Grant No. DE-FG02-06EF46339 and in part by in part by the National Science Foundation through the Materials Research Science and Engineering Center at the University of Michigan through Grant DMR-1120923.

5.2 Background

GaSb/GaAs nanostructured systems have attracted interest over the years due to their potential applications in storage and memory devices. These uses arise from the more commonly assumed type-II energy band alignment observed in such systems, where electron and hole carriers are spatially separated in the GaSb regions resulting in a lowered recombination of such carriers or, equivalently, long exciton lifetimes.[1, 2] These systems have also been demonstrated to be relevant to optoelectronics with applications in devices such as infrared emitters and intermediate band solar cells (IBSC's).[3-5] Conventional

Model Solid Theory, which relates the average atomic electrostatic potential to the vacuum level, predicts a type-I band alignment for unstrained GaSb/GaAs hetero-structures. On the other hand, type I band offsets have been experimentally demonstrated for GaAsSb/GaAs quantum wells, while type II band offsets are often reported for GaSb/GaAs QDs.[4–11] In addition, band edge calculations have predicted type I (type II) offsets for unstrained (strained) GaSb/GaAs QDs. Furthermore, it has been suggested that the Sb-rich (2x8) [As-rich (2x4)] reconstruction is needed for the nucleation of strain-free [strained] GaSb QDs with [without] misfit dislocations.[15,16]

5.3 Type I and Type II GaSb/GaAs Interfaces: Predictions and Power-Dependent PL

Band edge calculations of idealized (a) type I and (b) type II interfaces were carried out by the author using a 1D Poisson/Schrödinger solver, which will be discussed in more detail in Appendix E, and are presented in Fig. 5.1.[17-19] In Fig. 5.1, the calculated band edges, ground state energies of confined carriers, are plotted as solid lines, and the ground state wavefunctions are plotted as dashed lines for partial (blue) or full (green) ionization of the shallow dopant states. For type I interfaces, when the shallow dopant states are fully ionized, the electron and hole ground state energies both shift upward, resulting in increased (decreased) electron (hole) confinement energies. For type II interfaces, when the shallow dopant states are fully ionized, the electron (hole) ground state energies shifts upward (downward), resulting in increased confinement energies of electrons and holes, i.e. capacitive charging. The radiative photon energy for a type I interface, corresponding

to the energy separation between the confined state energies, is essentially independent of the illumination intensity. On the other hand, for a type II band alignment, increasing illumination intensity leads to an increase in the carrier concentration and a larger energy separation between the electron and hole ground states. Furthermore, electric field due to the accumulated, spatially separated charges leads to band bending. Due to both capacitive charging and band bending, at type II band alignment, the radiative photon energy is expected to increase with increasing illumination intensity.

Typically, for negligible (non-negligible) power-dependent blue-shift in PL radiative photon energy, type I (type II) band alignments are reported.[17-21] For a type II band alignment, it has been reported that the radiative photon energy follows a power law dependence on the illumination intensity, i.e. $\Delta E \propto I_{incident}^{n}$, where $I_{incident}$ is illumination intensity and n is a power factor.[22] In Fig. 5.2, the reported power-dependent shifts in radiative photon energies are plotted for various GaSb quantum dot (QD) or quantum well (QW) systems grown on GaAs substrates.[17-33] Furthermore, both axes of PL energy shift and laser power are plotted in loagrithimic scales, such that the slopes of the reported data points represent the power factor n values. The black dotted horizontal line in the plot indicates power-dependent energy shifts of 10 meV. The solid green, solid blue, and opened black data points correspond to power dependent PL blue-shift studies of GaAsSb quantum wells, strained GaSb quantum dots, and unstrained GaSb quantum dots, respectively. Furthermore, the reported literatures attribute band bending, capacitive charging, and both band bending and capacitive charging as the cause for the power dependent PL blue-shift, which are plotted as circles, squares, and triangles, repectively.

It has been predicted that the illumination-induced band-bending follows the power law of $\Delta E \propto I_{incident}^{n}$ with $n \approx 1/3$, while the illumination-induced capacitive charging follows the power law with $n \approx 1/2$, suggesting that the dominant mechanism of illumination-intensity-induced energy shift is capacitive charging.[22] On the other hand, a more recent experimental study reports that the illumination-induced band bending follows the power law at two different regimes; $n \approx 1/2$ at low illumination intensities and $n \approx 1/4$ at high illumination intensities. For the case of high illumination intensities, the penetration of the wavefunction into the potential barrier is slightly increased, leading to a slight decrease in the net charge, and reduced band bending, with $n \approx 1/4$. For illumination-induced state filling, althought n is predicted to be close to 1, experimental data to support this linearity between illumination intensity and PL blue shift is not apparently available. Contrary to the predicted n values for band bending and capacitive charging,[22,34] the n values of the reported power-dependent shifts in radiative photon energies varies from 0.1 to 1.1,[17-21] independent of the attributed mechanism for illumination-induced energy shift. Furthermore, in a study of influence of growth conditions of a type II heterostructure on the power exponent n, illumination-induced energy shifts have been attributed to capacitive charging.[22] Contrary to the predicted n value of 0.5 for capacitive charging, a range of low n values of $0.1 < n < 0.3$ has been reported.[22] Due to a disagreement between the predicted and observed n values for band bending and capacitive charging, other mechanisms are needed to be considered.

Interestingly, for power-dependent energy shifts in excess of 10 meV, linear least-squares fit to the logarithms of the energy shift vs. laser power with a range of slope values of $n > 0.25$ holds for strain-relaxed GaSb QDs, while a range of $0 < n < 0.25$ holds for

strained GaSb QDs and QWs. Indeed, it is likely that the local strain at the GaSb/GaAs interfaces substantially perturbs the electron wave function, leading to differences in the free-carrier-concentration-dependence (and the power-dependence) of the photon energy. Therefore, a systematic study of influence of local strain on the band structure is needed, which can be obtained by a nano-scale characterization of both atomic and band structures.

5.4 Experimental Methods

5.4.1 MBE Growth

To investigate the influence of strain and dislocation on the band alignment of GaSb/GaAs, GaSb QDs were grown on different surface termination and by different growth methods, respectively.

For examining the influence of misfit dislocation on the GaSb/GaAs QD band alignment, samples were grown by molecular-beam epitaxy (MBE) using solid Ga, Al, As_4, and Sb_4 sources by Prof. G. Balakrishnan's group at Univ. of New Mexico. 3-period GaSb/GaAs superlattices (SLs), consisting of 3.0 (MLs) GaSb and 20nm GaAs capping layers, separated by 200 nm GaAs between SLs, were grown on an n^+ GaAs (001) substrate. The GaSb QDs are grown at a substrate temperature of 500 °C, a growth rate of 0.3 ML/ s, and III/V ratios of 1:10 and 1:1 for the interfacial misfit (IMF) and Stranski–Krastanov (SK) growth modes, respectively. GaSb QDs grown by IMF and SK modes will be referred as "IMF GaSb QDs" and "SK GaSb QDs", respectively.[15,16]

Another GaSb/GaAs QD heterostructure was grown by A. J. Martin at the University of Michigan in Prof. Millenchick's group using using a growth rate of 0.3 μm/h and a Sb/Ga beam equivalent pressure ratio of 2.0. The "As-terminated" QD SLs were grown on a (2x4) GaAs surface, while the "Sb-terminated" QD SLs were grown on a (2x8) GaAs surface prepared by Sb flux exposure during cooling from 580 ^{o}C to 460 ^{o}C, forming nominally 1.0 ML of GaSb.[35,36] An additional 1.0 ML GaSb was deposited at 460 ^{o}C, such that the total deposited thickness of GaSb was nominally 2.0 ML. Layers containing 2.3 MLs GaSb, grown at 460 ^{o}C on a (2x4) GaAs surface, are termed the "As-terminated" QD SLs. For the GaSb/GaAs QD samples, all layers, except the GaSb layers, were Si-doped at ~ 6x10 /cm^3.

5.4.2 XSTM, XTEM, and APT on GaSb/GaAs Band Alignment

We examined several high resolution XSTM and transmission electron microscopy (TEM) images spanning > 0.5 μm^2 and acquired STS spectra from both Sb- and As-terminated GaSb/GaAs QD SLs. For TEM studies, cross-sectional specimens were prepared using conventional mechanical thinning followed by argon-ion milling at 77 K. TEM and electron diffraction were carried out in JEOL 3011 and JEOL 2010F TEMs, operating at 300 kV and 200 kV, respectively. All TEM work was performed by a previous group member, J. Canniff.

Atom probe tomography (APT) experiments were performed to obtain a 3D compositional profile of the SK and IMF GaSb QDs. To prepare samples for APT, we use focused-ion-beam (FIB) milling in a Helios SEM system to fabricate a conical section of

sample, as described in Chapter 2.5. The APT tips are mounted on Si posts and contain the layers of interest. The atomic arrangements within SK and IMF GaSb QDs were then collected in a commercial CAMECA LEAP 4000X Si system using Voltage pulses. Ions are collected with a data collection settings of detection rate of 0.5 %, pulse rate of 120 kHz, and an evaporation field of 18 V/nm.

5.5 Influence of Strain and Dislocations on GaSb/GaAs Quantum Dots

5.5.1 GaSb/GaAs QDs Band Alignment near Misfit Dislocations

The microstructure in the vicinity of the GaSb/GaAs QD SLs and defect structures are investigated via XTEM.[36] Figs. 5.3 (a) and (b) present the bright-field <110> zone axis large-scale XTEM images of Sb- and As- terminated GaSb/GaAs QD SLs, respectively. Although the XTEM images reveal different dimensions of GaSb QDs, with a smaller QD diameter for Sb-terminated, misfit dislocations are observed for both surface terminations. Shown in Figs. 5.3 (c) and 5.3 (d), the high magnification XTEM images of the Sb-terminated and As-terminated QDs reveal misfit dislocations in the vicinity of the GaSb QDs, which are labeled as "M". Furthermore, the presence of coherent and semi-coherent clusters, labeled as "C" and "S" respectively, suggests that the Sb-terminated and As-terminated GaSb QDs are both partially strain relaxed.

XSTM images of the Sb-terminated and As-terminated GaSb QDs are shown in Figs. 5.4 (a) and 5.4 (b).[36] Within each QD SL, bright (dark) regions corresponding to GaSb (GaAs) are apparent. Most of the GaSb QDs appear as 20 to 30 nm clustered regions of

GaAsSb within the GaSb wetting layer (WL), as indicated by the black arrows in Figs. 5.4 (a) and 5.4 (b). As shown in the XSTM images of the GaSb/GaAs QD SLs, the QDs are clustered with inhomogeneous Sb compositions, independent of surface termination. Interestingly, for uncapped QDs grown under similar conditions, plan-view atomic force microscopy (AFM) suggests the formation of 30 to 50 nm QDs.[35] Thus, it is likely that the QD clustering is driven by a local strain induced by the GaAs capping process. For example, the local strain would provide a driving force for Sb mass transport away from the QD.[37–40]

In Figs. 5.5, the normalized conductance versus sample bias voltage is plotted for the edge and the core of clustered GaSb QDs grown on the (a) Sb-terminated and (b) As-terminated GaAs surfaces, both in comparison with a region of clean GaAs.[36] The sample voltage corresponds to the energy relative to the Fermi level. The GaAs spectra, shown as the solid line spectra in Fig. 5.5, display well-defined band edges, with bandgap values of 1.52±0.10 eV and 1.55±0.10 eV. STS measurements on the Sb- terminated GaSb QD, shown in Fig. 5.5 (a), reveal energy values lower than those of the GaAs band edges, suggesting a type I band offset, consistent with strain-free band edge calculations.[12–14] Similar trends are apparent for the As-terminated clustered QD in Fig. 5.5 (b), except the effective bandgaps are lower, with values of 0.70±0.10 eV (0.54±0.10 eV) at the QD edge (core). Thus, for both the Sb-terminated and As-terminated GaSb QDs, formation of misfit dislocations and partial strain relaxation resulted in a type I band alignment.

5.5.2 IMF and SK GaSb/GaAs QDs Band Alignment

To further consider the influence of the strain, dislocation, and dislocation charging dependence of GaSb/GaAs band alignment, 3D compositional profile in the vicinity of GaSb QDs are collected via XSTM. Furthermore, Figs. 5.6 (a) and (b) show the XSTM images of SK and IMF GaSb QD samples, respectively. However, we were able to only find GaSb wetting layers, indicating failure of nucleation of SK GaSb QDs. The IMF GaSb QDs are present near the line labeled as 4 ML GaSb. In addition, Fig. 5.7(a) shows a constant-current high magnification XSTM image in the vicinity of a IMF GaSb QD, with a 1.23 nm tip height color range displayed, such that the bright and dark regions correspond to the GaSb QD and GaAs matrix, respectively.

Cross-sectional scanning tunneling microscopy (X-STM) data is used as input into a continuum model as a composition profile of GaSb/GaAs QDs. To calculate the 3D distribution of elastic misfit strain, the 3D composition profile is interpolated onto a finite element mesh with periodic boundary conditions determined by the average QD separation in similarly grown samples, ~50 nm. The 3D composition profile is calculated following the procedure presented in Appendix B. We calculate 3D profiles of the effective masses, permittivities, elastic constants, and deformation potentials, assuming linear interpolations of the values for the binary compounds GaAs and GaSb shown in Table I. In addition, using isotropic linear elastic edge dislocation theory,[1] we compute the 3D strain distribution due to 5.5 nm spaced edge dislocations at the bottom and top interfaces between the quantum dot and matrix, a configuration that has been reported for GaAs capped InSb and InAs QDs with a similar ~7% misfit.[2,3] The removal of atomic planes in the GaSb QDs is represented by the dislocation loops with the associated in-plan

hydrostatic strain contours. The net in-plane hydrostatic strain contours, including both misfit and dislocation-induced strain. We utilized the net strain 3D distribution to calculate rigid shifts in the VB and CB edges via the corresponding 3D profile of deformation potentials.

To consider the effects of dislocation charging, we treat Ga dangling bonds along the dislocation core as electron acceptors. We assume two dangling bonds per lattice site, each with occupancy, *sf*, such that the total line charge is $|sf(2q/a_{GaSb})|$. We then compute the form of the electrostatic potential, *V(r)*, using Poisson's Equation:

$$\nabla^2 V(r) = -\frac{\rho(r)}{\varepsilon_0 \varepsilon_r(r)} \quad (1)$$

where $\rho(r)$ is the spatially varying space charge, ε_0 is the permittivity of free space, and ε_r (r) is a spatially varying permittivity assumed to follow the rule of mixtures. Since the total charge in the system must be zero,[1] a space charge density, ρ_{sc}, with equal magnitude and opposite sign is induced, according to:

$$\rho_{sc} = -\left|\frac{sf(2qL_{cores})}{a_{GaSb}V}\right| \quad (2)$$

Where L_{cores} is the added length of the two dislocation core centerlines, and *V* is the total volume of the system. Ultimately, the space charge induces a 3-D electrostatic potential, which is added as a rigid shift to the band offset.

Finally, to estimate the confinement induced by the spatially varying band edge profiles, we solve the steady-state Schrödinger equation in the effective mass approximation, equivalent to the **k·p** approach in a single band formulation. This simple approach is conveniently formulated using the finite element method and allows for an estimate of the energy levels and confinement of carriers,[3] and thus the effective local band

alignment type.

The conduction band (CB) and valence band (VB) edge profiles calculated along the red-dotted lines, i.e. paths (1)-(4), in Fig. 5.7 (b), are shown in Fig. 5.8 for the cases of (a) unstrained, (b) misfit strain, and (c)-(e) both misfit and dislocation strain with various degrees of dislocation charging: dangling bond site occupancy (d) sf=0.1 and (e) sf=0.4.

For the unstrained case in Fig. 5.8 (a), a weak type I alignment is observed for paths across the QD center (paths 1 and 2), with minimal variations in band-edges across the paths above and below the QD (paths 3 and 4). The CB offset (CBO) and VB offset (VBO), with values of 0.06 eV and 0.67 eV, are consistent with those predicted by Model Solid theory.[14] In Fig. 58 (b), with the introduction of lattice misfit strain, a type II alignment is observed along paths 1 and 2, with minimal changes to the CBO and VBO along paths 3 and 4. However, the strained CBO of 0.2 eV is slightly higher than the experimentally measured value of 0.1 eV.[6,7]

In Figs. 5.8 (c)-5.8 (e), the influence of dislocation strain and charging on GaSb/GaAs QD band-edge profiles across paths 1-4 in Fig. 5.8 (b) are considered. For path 1, the dislocation-induced strain-fields reduce the energy of the GaSb CB edge in the vicinity of the dislocation cores, resulting in a local type I offset. For path 2, the GaSb CB edge is slightly higher in energy, leading to a lower average CBO of 0.1eV, consistent with experimental values reported in the literature.[10,11,37] For paths 3 and 4, in the vicinity of the dislocation cores, the CB edge is raised while the VB edge is lowered.

In Figs. 5.8 (d) and 5.8 (e), the influence of dislocation charging with dangling bond site occupancies sf=0.1 and sf=0.4, are shown. For sf=0.1 in Fig. 5.7(d), the CB and VB profiles along paths 1-4 are very similar to the corresponding values for the calculations

with misfit and dislocations strain in Fig. 5.8 (c). With dislocation charging increased to sf=0.4, both the CB and VB edges are reduced in the vicinity of the dislocation cores. Since this additional electrostatic potential equally displaces the CB and VB edges, the classification of band alignment type in 1D is not obvious. In addition, band bending due to the charged dislocation cores induces complex potential profiles that may increase or decrease the spatial overlap of electron or hole states based on the spatially varying effective mass. For the higher site occupancy, sf=0.4, the average band alignment is apparently type II. To confirm this observation, we consider 3D solutions to the Schrödinger equation.

Fig. 5.9 (a) and (c) shows the reconstructed APT data of IMF GaSb QDs. The Ga atoms and Sb atoms are displayed as blue dots, and an isosurface of $x_{Sb} > 0.2$ is plotted as yellow spheres. The 3D composition profile is input into a finite element mesh, as shown in Fig. 5.9 (b) and (d). Using reconstructed APT data as an input for 3D composition profile, and the resulting normalized charge density isosurfaces for various conduction and valence band states is shown in Fig. 5.10. For IMF QDs, the (a) conduction and (b) valence band edges are plotted as blue dots. The charge densities show hole confinement in regions of high Sb concentration and electron confinement in regions of high As concentration. This spatial separation of electron and hole charge densities is consistent with a type-II band aligned system. For SK QDs, the (c) conduction and (d) valence band edges are plotted as well blue dots. Due to the failure of nucleation of GaSB QDs, our results only present the case of a charge distribution around Sb wetting layer. Surprisingly, electron and hole spatial separation was also observed.

Finally, PL measurements were taken on SK and IMF GaSb QD samples, which are shown in Fig. 5.11 (a) and (b), respectively. For the SK GaSb QD sample, no emission peak from the GaSb wetting layer was observed. Instead, we observe only an emission peak from GaAs. For the IMF GaSb QD sample, a strong emission peak from GaSb QDs are observed at 1.33 eV at room temperature.

5.6 Conclusions

In summary, we investigate the influence of strain and dislocations on band alignments in GaSb/GaAs QD systems. A combination of XTEM, XSTM and STS reveal presence of misfit dislocations around both coherent and semi-coherent clustered QDs, independent of Sb- vs. As-termination of the GaAs surface. STS collected across the QD/GaAs interfaces reveals type I band offsets, consistent with the expected band offsets for unstrained GaSb/GaAs systems.[12–14] Furthermore, using composition profiles from XSTM images and reconstructed APT data from IMF GaSb/GaAs QDs as input into a continuum model, we examine the effects of misfit strain, dislocation strain, and dislocation charging on CB and VB edge profiles. For an unstrained GaSb/GaAs QD, a weak type I band alignment is predicted. With the addition of misfit strain, a transition to a type II band alignment is observed. However, the inclusion of additional effects such as dislocation strain and/or dislocation charging lead to local restorations of the type I and/or type II alignment. Therefore, variations in QD morphologies and dislocation positions/orientations may be used to tune the coexistence of local type I and type II band alignments.

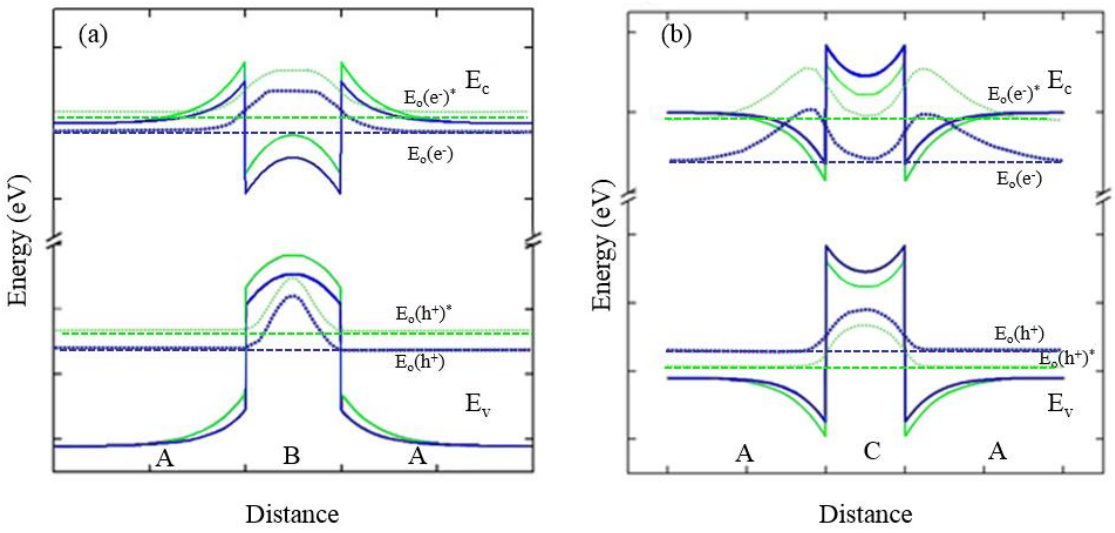

Fig. 5.1: Plots of the calculated band edges (solid lines), ground state energies of confined carriers (dashed lines), and corresponding wave functions (dotted lines) for partial (blue) and full (green) dopant ionization. (a) For type I band alignment, the upward shift of electron and hole ground state energies does not alter the energy separation between the ground state energies. (b) For type II band alignment, the upward (downward) shift of electron (hole) ground state energy leads to an increase in energy separation between the electron and hole ground states. Band edge calculations were carried out by the author using a 1D Poisson/Schrödinger solver.[17-19]

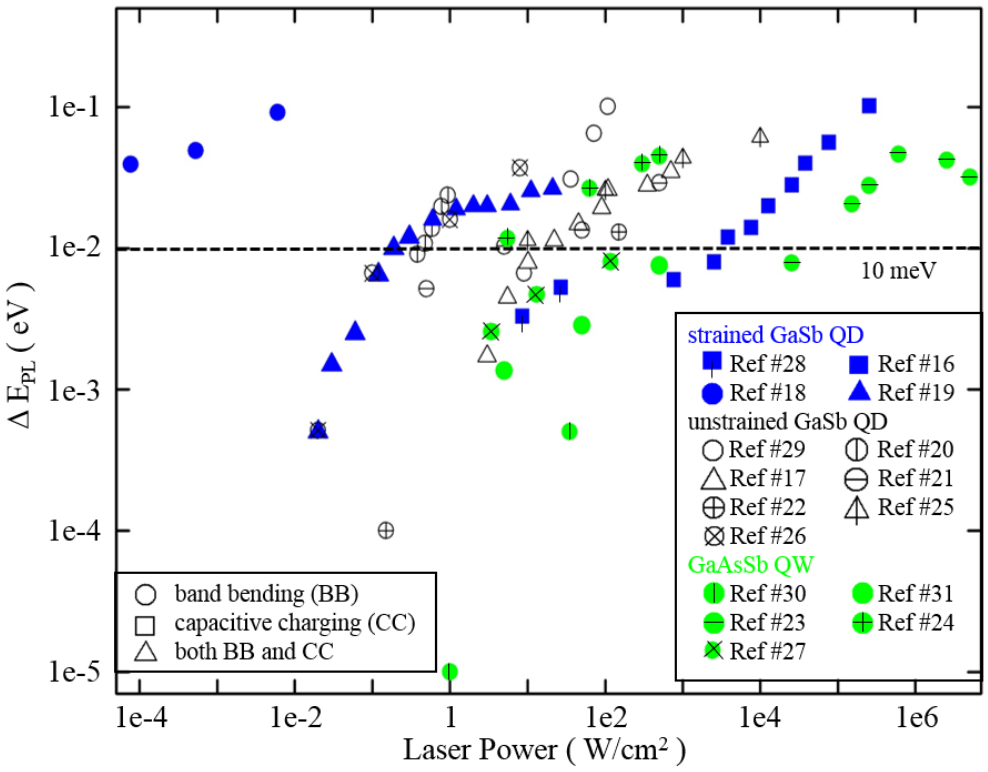

Fig. 5.2: Logarithm of the PL energy shift vs. the logarithm of the laser power for various GaSb/GaAs quantum structures.[17-31] The solid green, solid blue, and opened black data points correspond to GaAsSb quantum wells, strained GaSb quantum dots, and unstrained GaSb quantum dots, respectively. Furthermore, band bending, capacitive charging, and both band bending and capacitive charging are claimed to be the cause of the power dependent PL blue-shift, which are plotted as circles, squares, and triangles, respectively.

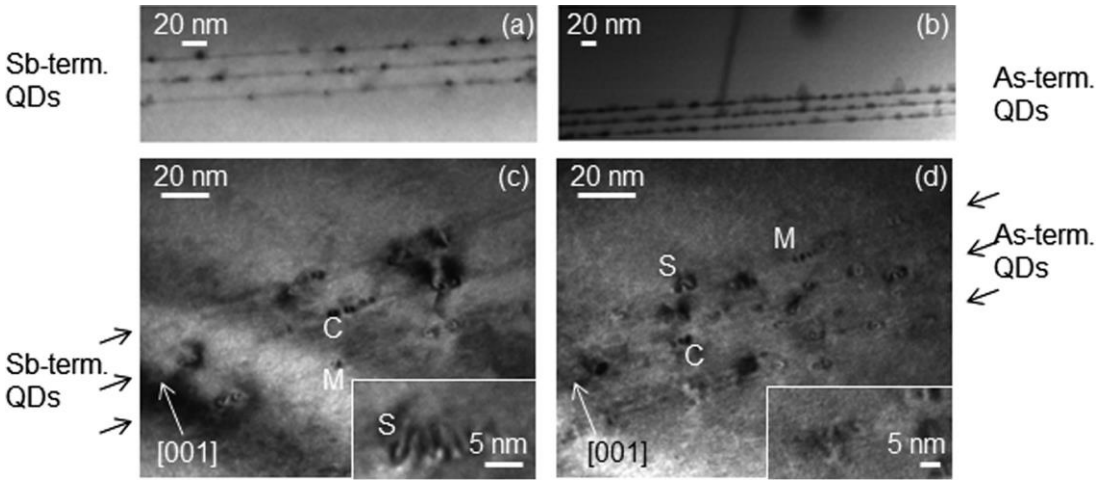

Fig. 5.3: Bright-field <110> zone-axis TEM images, which contain GaSb/GaAs QD SLs grown on (a) Sb-terminated and (b) As-terminated GaAs surfaces; [220] 2-beam bright field TEM images of clustered GaSb QDs grown on (c) Sb-terminated and (d) As-terminated GaAs surfaces.[36] The high magnification insets reveal semi-coherent clusters in the vicinity of the GaSb QDs. Misfit dislocations ("M"), coherent clusters ("C"), and semi-coherent ("S") clusters are indicated in (c) and (d).

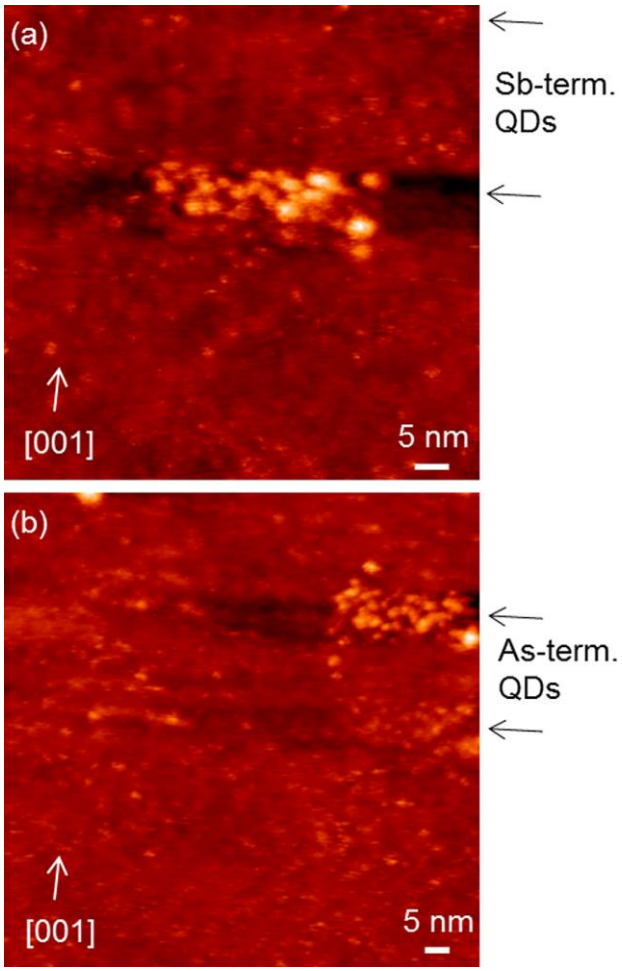

Fig. 5.4: High-magnification XSTM topographic images of GaSb/GaAs QD SLs grown on (a) Sb-terminated and (b) As-terminated GaAs surfaces.[36] The images were obtained at a sample bias voltage of ±2.4 V; the greyscale ranges displayed are (a) 0.4nm, and (b) 0.5 nm.

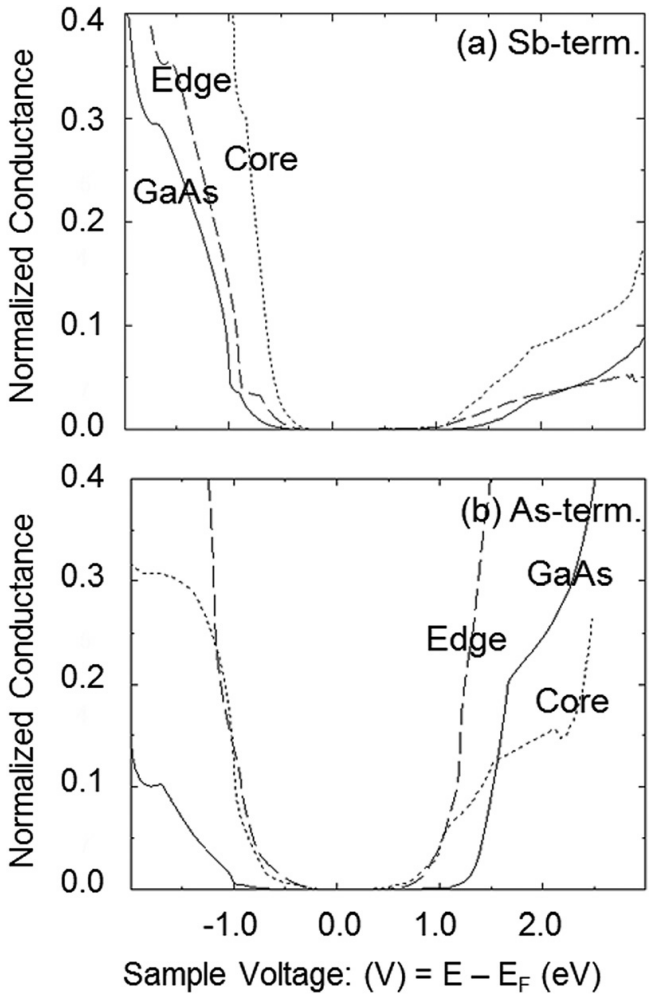

Fig. 5.5: Plots of normalized conductance versus sample bias voltage, collected from the GaAs (solid line), the GaSb/GaAs QD edge (dashed line), and the GaSb/GaAs QD core (dotted line), grown on (a) Sb-terminated and (b) As-terminated GaAs surfaces.[36] The sample voltages correspond to the energy relative to the Fermi level.

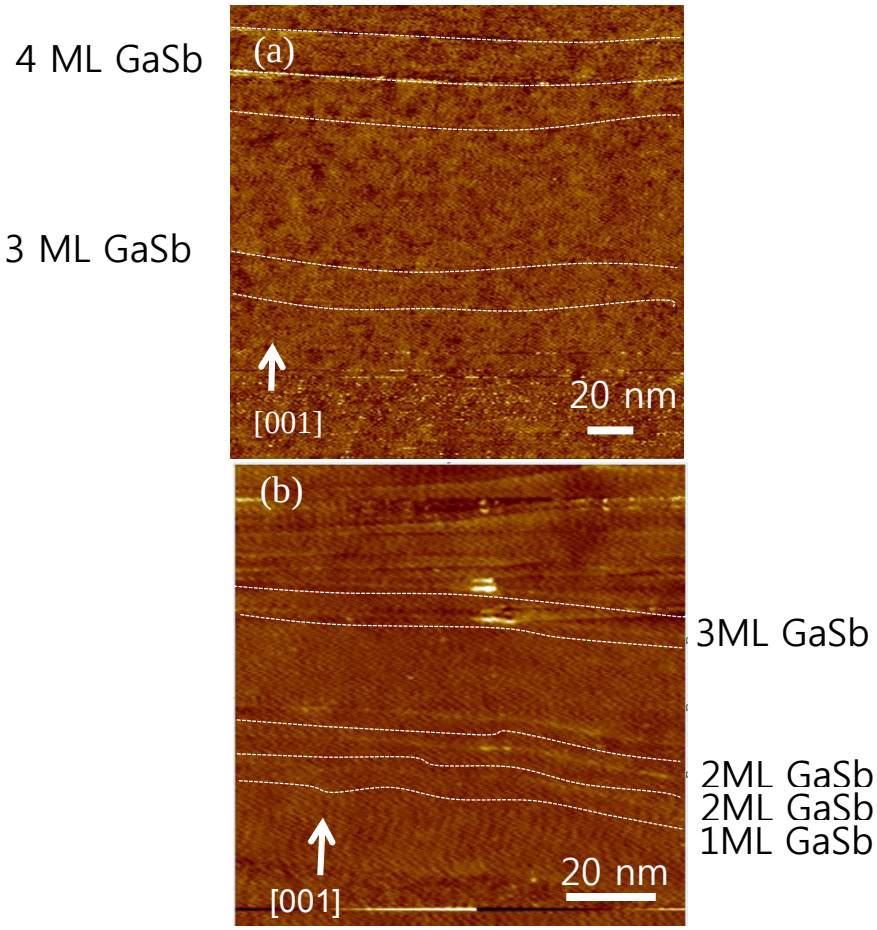

Fig. 5.6: XSTM image of (a) SK and (b) IMF GaSb QD samples. The SK QDs were not nucleated and only Sb wetting layers are present. The IMF QDs are clearly observed near the line labeled as 3ML GaSb.

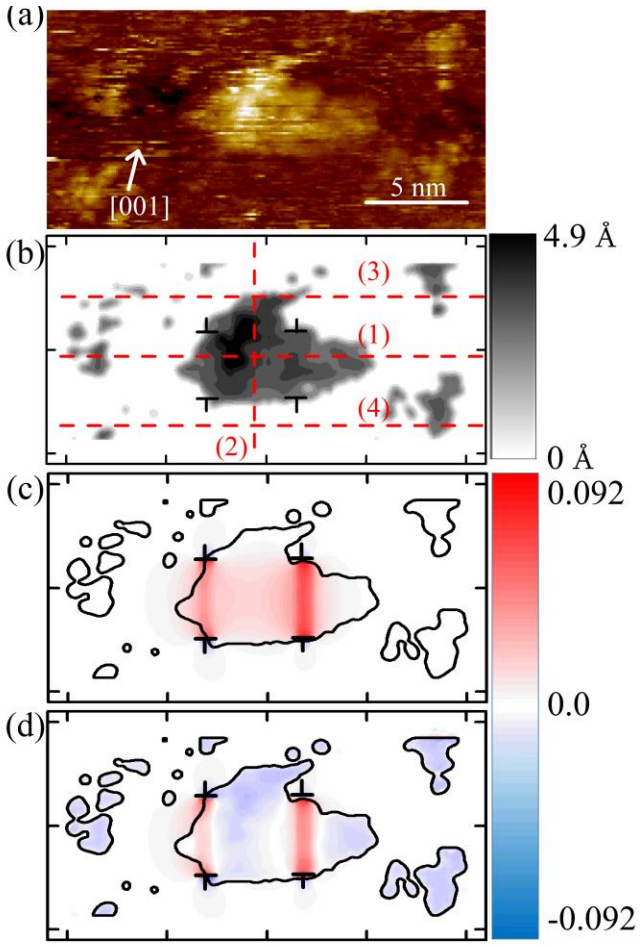

Fig. 5.7: (a) cross-sectional scanning tunneling microscopy (XSTM) image, acquired in the vicinity of a GaSb/GaAs quantum dot (QD) using a constant tunneling current of 0.25 nA and a sample bias -2.6 V. The tip height color-scale range displayed is 1.23 nm, with bright and dark regions corresponding to GaSb QD and the GaAs matrix, respectively. Pixels with tip height up to 4.9 ± 0.5 Å above the GaAs background in (a) are displayed in (b) with bright and dark-gray scales corresponding to increasing GaSb fractions, xSb. The removal of atomic planes in the GaSb QDs is represented by the dislocation core symbols in (b), and the associated in-plane hydrostatic strain contours are shown in (c). The net in-plane hydrostatic strain contours, including both the misfit and dislocation-induced strain, are shown in (d). The red dotted lines in (b) indicate paths along which band structure profiles will be presented.

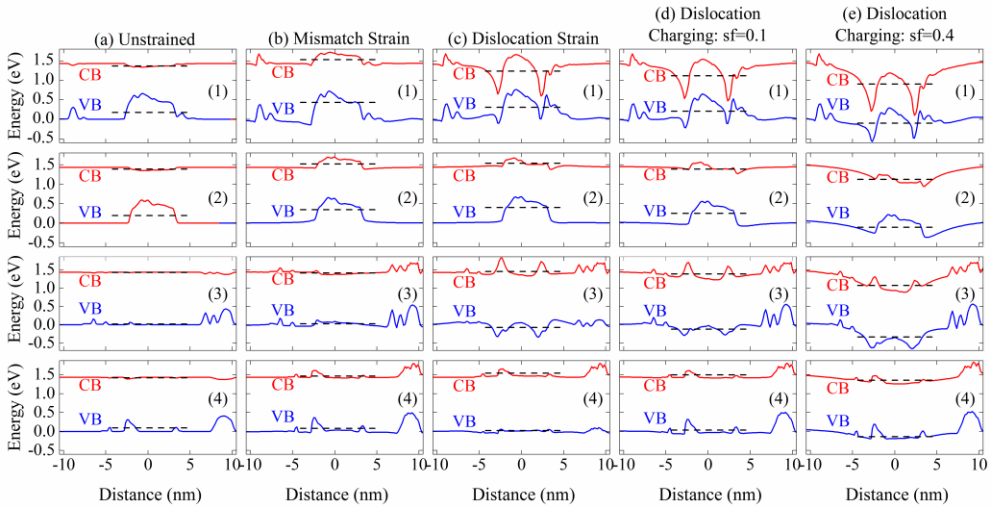

Fig. 5.8: Band profiles for the cases of (a) unstrained, (b) lattice mismatch strain, (c) dislocation strain, (d) dislocation charging of sf=0.1, and (e) dislocation charging of sf=0.4 across paths 1 – 4 from Fig. 1(b). The black dotted lines denote volume-averaged band energies across the QD., with the GaAs matrix band energies at 1.43 eV (CB) and 0 eV (VB) as reference levels. For (a) the unstrained case, a weak type-I alignment is observed for paths across the QD center (paths 1 and 2), with smaller band-edge variations across paths above and below the QD (paths 3 and 4). In (b), with the introduction of misfit strain, the CB along paths 1 and 2 is raised, leading to type II band alignment; meanwhile, negligible changes to both CB and VB are observed along paths 3 and 4. In (c), with the inclusion of both misfit and dislocation strain, the band alignment is again type I across paths 1 and 2, with minimal change along paths 3 and 4. In (d), for sf=0.1, the CB and VB values are similar to those in (c). Finally, in (e), for sf=0.4, both CB and VB are lowered across paths 1-4, resulting in type II band alignments.

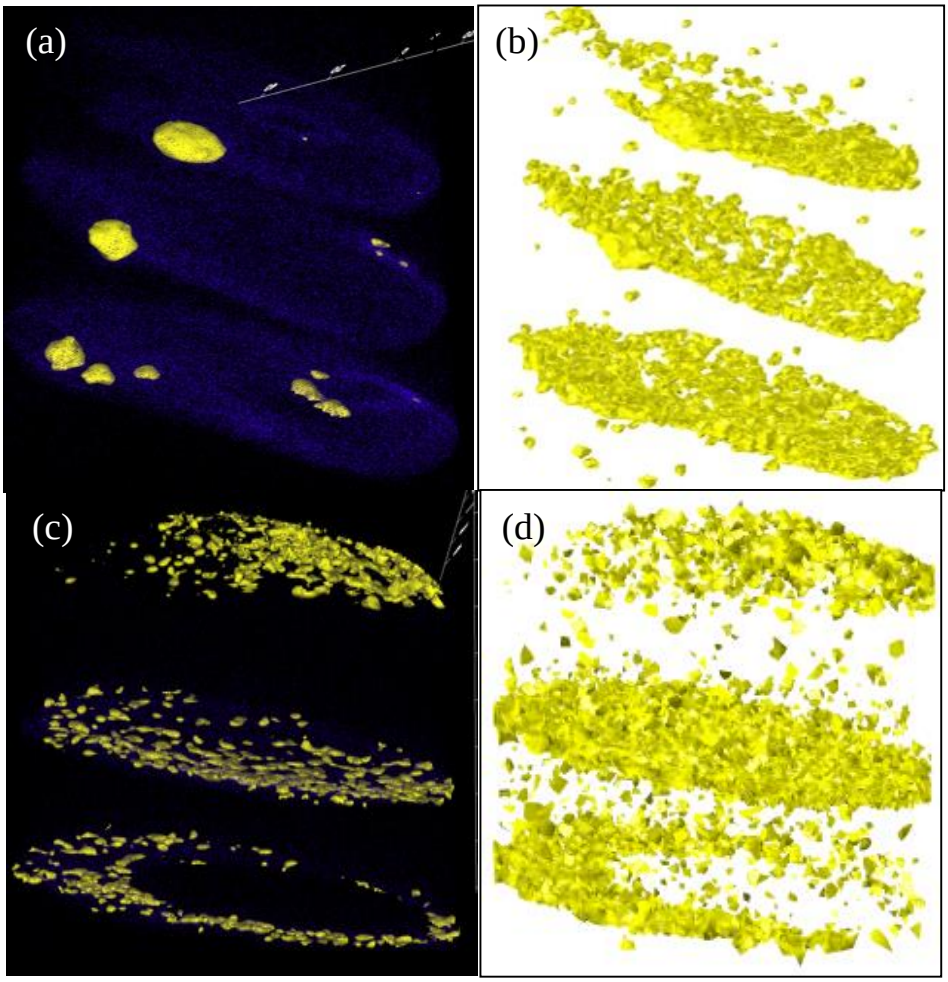

Fig. 5.9: (a) Reconstruction of APT data and (b) the interpolated 3D composition profile of IMF GaSb QDs. Isosurface plots detailing Sb concentrations > 20% are indicated as yellow spheres.

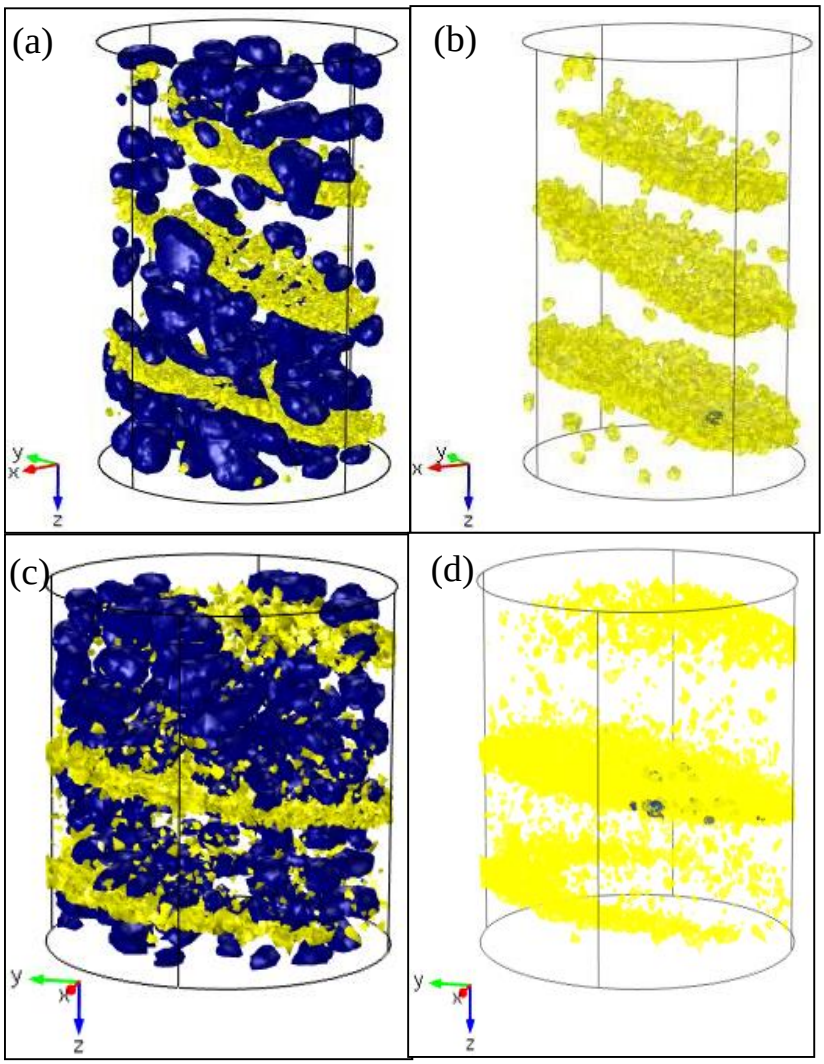

Fig. 5.10: (a),(c) Conduction band and (b),(d) Valence band charge density isosurfaces (Blue) detailing electron/hole confinement for IMF and SK grown sample, respectively. The isosurface for Sb concentration >20% is shown for reference (Yellow). Spatial separation of electrons and holes suggest a type II band alignment for SK QDs.

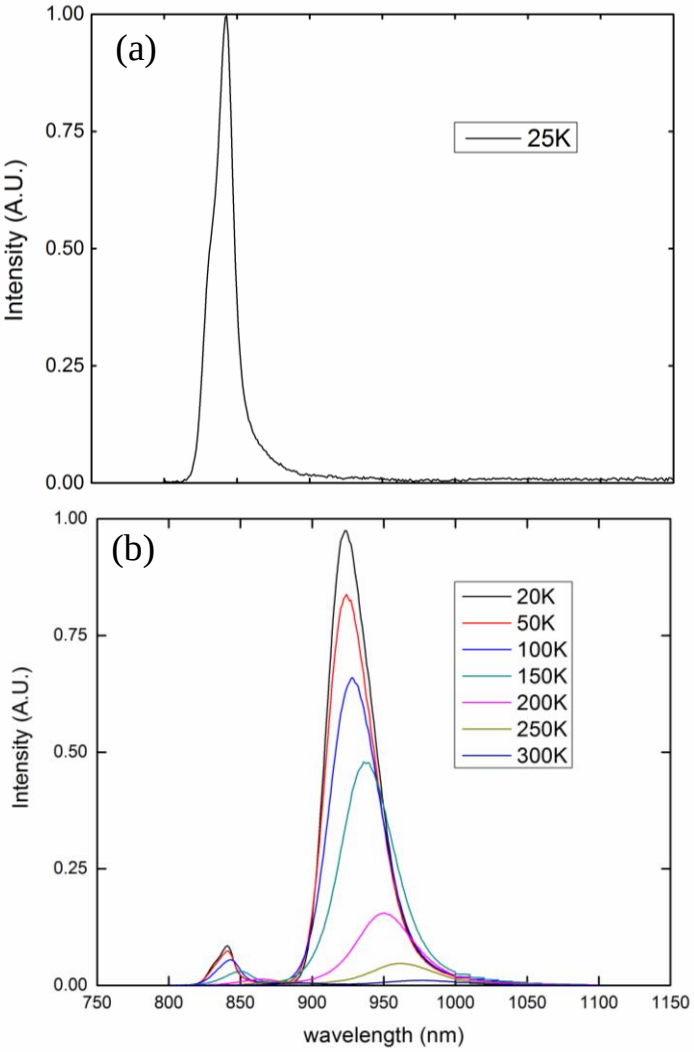

Fig. 5.11: Temperature dependent photoluminescence data from (a) SK and (b) IMF GaSb QD samples. For the SK GaSb QD sample, only photoemission from GaAs was observed. For the IMF GaSb QD sample, GaSb peaks were observed at 1.35 eV.

5.7 References

[1]J.-B. Wang, S. R. Johnson, S. A. Chaparro, D. Ding, Y. Cao, Y. G. Sadofyev, Y.-H. Zhang, J. A. Gupta, and C. Z. Guo, *Phys. Rev. B* **70**, 195339 (2004).

[2]J. Wu, W. Shan, and W. Walukiewicz, *Semicond. Sci. Technol.* **17**, 860 (2002).

[3]M. B. Thomas, W. M. Coderre, and J. C. Woolley, *Phys. Status Solidi A* **2**, K141 (1970).

[4]T. S. Wang, J. T. Tsai, K. I Lin, J. S. Hwang, H. H. Lin, and L. C. Chou, *Mater. Sci. Eng., B* **147**, 131 (2008).

[5]J. Tatebayashi, B. Liang, D. A. Bussian, H. Htoon, S. Huang, G. Balakrishnan, V. Klimov, L. R. Dawson, and D. L. Huffaker, *IEEE Trans. Nanotechnol.* **8**, 269 (2009).

[6]B. Liang, A. Lin, N. Pavarelli, C. Reyner, J. Tatebayashi, K. Nunna, J. He, T. J. Ochalski, G. Huyet, and D. L. Huffaker, *Nanotechnology* **20**, 455604 (2009).

[7]N. N. Ledentsov, J. B€ohrer, M. Beer, F. Heinrichsdorff, M. Grundmann, D. Bimberg, S. V. Ivanov, B. Ya. Meltser, S. V. Shaposhnikov, I. N. Yassievich, N. N. Faleev, P. S. Kop'ev, and Z. I. Alferov, *Phys. Rev. B* **52**, 14058 (1995).

[8]R. J. Young, E. P. Smakman, A. M. Sanchez, P. Hodgson, P. M. Koenraad, and M. Hayne, *Appl. Phys. Lett.* **100**, 082104 (2012).

[9]K. Suzuki, R. A. Hogg, and Y. Arakawa, *J. Appl. Phys.* **85**, 8349 (1999).

[10]M. E. Rubin, H. R. Blank, M. A. Chin, H. Kroemer, and V. Narayanamurti, *Appl. Phys. Lett.* **70**, 1590 (1997).

[11]R. Timm, H. Eisele, A. Lenz, L. Ivanova, V. Vosseb€urger, T. Warming, D. Bimberg, I. Farrer, D. A. Ritchie, and M. Deahne, *Nano Lett.* **10**, 3972 (2010).

[12]M. Hayne, J. Maes, S. Bersier, V. V. Moschalkov, A. Schliwa, L. Meuller-Kirsch, C. Kapteyn, R. Heitz, and D. Bimberg, *Appl. Phys. Lett.* **82**, 4355 (2003).

[13]W. Walukiewicz, *Physica B* **302**, 123 (2001).

[14]C. G. Van de Walle and J. Neugebauer, *Nature* **423**, 626 (2003).

[15]S. Huang, G. Balakrishnan, and D. L. Huffaker, *J. Appl. Phys.* **105**, 103104 (2009).

[16]G. Balakrishnan, J. Tatebayashi, A. Khoshakhlagh, S. H. Huang, A. Jallipalli, L. R. Dawson, and D. L. Huffaker, *Appl. Phys. Lett.* **89**, 161104 (2006).

[17]G. L. Snider, I. -H. Tan, and E. L. Hu, *J. of Applied Physics* **68**, 2849 (1990).

[18]I. -H. Tan, G. L. Snider, and E. L. Hu, *J. of Applied Physics* **68**, 4071 (1990).

[19]1D Poission- Schrödinger solver [Computer software], retrieved from http://www3.nd.edu/~gsnider/, (2011).

[17]J. Tatebayashi, B. Liang, D. Bussian, H. Htoon, S. Huang, G. Blakrishnan, V. Klimov, L. R. Dawson and D. L. Huffaker, *IEEE Transactions on Nanotechnology* **8**, 269 (2009).

[18]C. Tseng, S. Mai, W. Lin, S. Wu, B. Yu, S. Chen, S. Lin, J. Shyue, and M. Wu, *IEEE J. Quant. Elec.* **47**, 335 (2011).

[19]B. Liang, A. Lin, N. Pavarelli, C. Reyner, J. Tatebayashi, K. Nunnna, J. He, T. Ochalski, G. Huyet and D. L. Hufffaker, *Nanotechnology* **20**, 455604 (2009).

[20] J. Wang, S. Johnson, S. Chaparro, D. Ding, Y. Cao, Y. Sadofyez, Y. Zhang, J. Gupta and C. Guo, *Phys. Rev. B* **70**, 195339 (2004).

[21]J. He, F. Bao and J. Zhang, *Appl. Phys. Lett.* **100**, 171914 (2012).

[22]P. D. Hodgson, R. J. Young, M. Ahmad Kamarudin, P. J. Carrington, A. Krier, Q. D. Zhuang, E. P. Smakman, P. M. Koenraad, and M. Hayne, *J. Appl. Phys.* **114**, 073519 (2013)

[23]L. Muller-Kirsch, A. Schliwa, O. Stier, R. Heitz, H. Kirmse, W. Neumann, and D. Bimberg, *Phys. Rev. B* **85**, 035432 (2012).

[24]N. Ledentsov, J. Bohrer, M. Beer, F. Heinrichsdorff, M. Grundmann, D. Bimberg, S. Ivanova, B. Meltser, S. Shaposhnikov, I. Yassievich, N. Faleev, P. Kop'ev, Z. Alferov, *Phys. Rev. B* **52**, 14058 (1995).

[25]P. Sitarek, H. P. Hsu, Y. S. Huang, J. M. Lin, H. H. Lin and K. K. Tiong, *J. Appl. Phys.* **105**, 123523 (2009)

[26]S. V. Morozov, D. I. Kryzhkov, A. N. Yablonsky, V. Antonov, D. I. Kuritsin, D. M. Gaponova, Yu. G. Sadofyev, N. Samal, V. I. Gavrilenko, and Z. F. Krasilnik, *J. Appl. Phys.* **113**, 163107 (2013)

[27]M. Dinu, J. E. Cunningham, F. Quochi, and J. Shah, *J. Appl. Phys*. **94**, 1506 (2003);

[28] E. Machado-Charry, P. Boulanger, L. Genovese, N. Mousseau, and P. Pochet, *Applied Physics Letters* **101**, 132405 (2012).

[29] M. Tytus, J. Krasnyj, W. Jacak, A. Chuchmala, W. Donderowicz and L. Jacak, *Journal of Physics: C* **104**, 012011 (2008).

[30]. Genovese, B. Videau, M. Ospici, T. Deutsch, S. Goedecker, J.-F. Mehaut, *Comptes Rendus Mecanique* **339**, 149-164 (2011).

[31] F. Hatami, N. N. Ledentsov, M. Grundmann, J. Böhrer and F. Heinrichsdorff, M. Beer, D. Bimberg, S. S. Ruvimov, P. Werner, U. Gösele, J. Heydenreich, U. Richter, S. V. Ivanov, B. Ya. Meltser, P. S. Kop'ev and Zh. I. Alferov, *Appl. Phys. Lett.* **67**, 656 (1995).

[32]J. Tatebayashi, B. Liang, R. Laghumavarapu, D. Bussian, H. Htoon, V. Klimov, G. Balakrishnan, L. Dawson and D. Huffaker, *Nanotechnology* **19**, 295704 (2008).

[33]J. Tatebayashi, A. Khoshakhlagh, S. Huang, L. Dawson, G. Balakrishnan, D. Huffaker, D. Bussian, H. Htoon and V. Klimov, *Appl. Phys. Lett.* **90**, 261115 (2007).

[34]F. Hatami, N. N. Ledentsov, M. Grundmann, J. Böhrer and F. Heinrichsdorff, M. Beer, D. Bimberg, S. S. Ruvimov, P. Werner, U. Gösele, J. Heydenreich, U. Richter, S. V. Ivanov, B. Ya. Meltser, P. S. Kop'ev and Zh. I. Alferov, *Appl. Phys. Lett.* **67**, 656 (1995).

[35]A. J. Martin, T.W. Saucer, K. Sun, S. J. Kim, G. Ran, G. Rodriguez, X. Pan, V. Sih, and J. M.Millunchick, *J. Vac. Sci. Technol. B* **30**, 02B112 (2012).

[36]E. S. Zech, A. S. Chang, A. J. Martin, J. C. Canniff, Y. H. Lin, J. M. Millunchick, and R. S. Goldman, *Appl. Phys. Lett.* **103**, 082107 (2013).

[37]E. P. Smakman, J. K. Garleff, R. J. Young, M. Hayne, P. Rambabu, and P. M. Koenraad, *Appl. Phys. Lett.* **100**, 142116 (2012).

[38]R. Timm, A. Lenz, H. Eisele, L. Ivanova, M. D€ae, G. Balakrishnan, D. L. Huffaker, I. Farrer, and D. A. Ritchie, *J. Vac. Sci. Technol. B* **26**, 1492 (2008).

[39]G. A. M. Beltra, E. A. Marquis, A. G. Taboada, J. M. Ripalda, J. M. Garcia, and S. I. Molina, *Ultramicroscopy* **111**, 1073 (2011).

[40]A. J. Martin, J. Hwang, E. A. Marquis, E. Smakman, T. W. Saucer, G. V. Rodriguez, A. H. Hunter, V. Sih, P. M. Koenraad, J. D. Phillips, and J. M. Millunchick, *Appl. Phys. Lett.* **102**, 113103 (2013).

Chapter 6

Summary and Suggestions for Future Work

6.1 Summary

For semiconductor heterostructures, the identification of the precise band offsets at semiconductor interfaces are crucially important for successful development of electronic and optoelectronic devices. However, issues at the interfaces, such as strain or defects, yet needs to be investigated for precise band tuning of semiconductor heterostructures. In this dissertation, the influence of Sb incorporation on the InGaAs(Sb)N/GaAs band alignment is investigated. Furthermore, the influence of starting substrate on InGaN/GaN QD formation and properties is examined by QD density, dimension, and band gaps of different InGaN QDs on free-standing GaN or GaN/AlN/sapphire substrates. Furthermore, the origins of type I to type II transition in GaSb/GaAs QD band alignment is investigated. In the following sections, a brief summary of the results from these studies will be presented.

6.1.1 Influence of Sb Incorporation on InGaAs(Sb)N/GaAs Band Alignment

We investigated the influence of Sb incorporation on InGaAs(Sb)N/GaAs band alignment. A combination of XSTM and SIMS reveals InGaAs(Sb)N layers with

compositions of InGaAsN and InGaAsSbN. STS collected across the InGaAsN/GaAs interface suggests a type II band offset, presumably due to low indium concentration and minimal strain-induced splitting of the valence band. In addition, STS reveals a type I band-offset at InGaAsSbN/GaAs interface. The Sb-induced variation in band alignment is significantly larger than predicted values, suggesting the possibility of both VBO and CBO tuning at InGaAs(Sb)N/GaAs interfaces, with minimal Sb incorporation.

6.1.2 Influence of Substrate on InGaN/GaN Quantum Dot Formation and Properties

We investigated the InGaN QD formation of various sizes and band gap energy values grown on different substrates by MBE. For single layer InGaN QDs on a free-standing GaN substrate, a combination of STM and STS reveals formation of InGaN QDs with a low dot density, most likely following the initial growth morphology. In the case of single layer InGaN QDs grown on GaN/sapphire substrate, we report formation of large and ultra-small InGaN QDs with densities estimated to be at least one order of magnitude larger than that of QDs grown on the free-standing GaN substrate. For multi-layer InGaN QDs grown on GaN/sapphire, STM and STS reveal a high quantum dot density and regularly spaced QDs. However, ultra-small QDs are not observed for multi-layer on GaN/sapphire, suggesting that QD formation is predominantly driven by the strain field from the buried QDs rather than the residual stress around the threading dislocation. Furthermore, the effective band gap energy values at the center of the InGaN QD is lower for single layer on GaN/sapphire compared to the other cases due to indium-rich

nanostructure formation. STS collected across the InGaN QD reveal a gradient in the effective band gap energy values, decreasing laterally toward the QD center. Our work suggests that a wide variety of InGaN QD dimension, density, and band structure can be achieved by using different starting substrate and number of layers of InGaN QD stacks.

6.1.3 Influence of Strain, Dislocation, and Dislocation Charging on the GaSb/GaAs Band Alignment

We have investigated the influence of strain and dislocations on band alignments in GaSb/GaAs QD systems. A combination of XTEM, XSTM and STS reveal the presence of misfit dislocations in the both coherent and semi-coherent clustered QDs, independent of Sb- vs. As-termination of the GaAs surface. STS collected across the QD/GaAs interfaces reveals type I band offsets for both Sb- and As- terminated GaSb. Furthermore, using composition profiles from XSTM images as input into a continuum model, we examine the effects of misfit strain, dislocation strain, and dislocation charging on CB and VB edge profiles. For an unstrained GaSb/GaAs QD, a weak type I band alignment is predicted. With the addition of misfit strain, a transition to a type II band alignment is observed. However, the inclusion of additional effects such as dislocation strain and/or dislocation charging lead to local restorations of the type I and/or type II alignment. Therefore, variations in QD morphologies and dislocation positions/orientations may be used to tune the coexistence of local type I and type II band alignments. The reconstructed APT data of SK and IMF GaSb/GaAs QDs is input as a 3D composition profile, and the

sptial distribution of carrier charges were calculated, revealing a type II band alignment for both cases.

6.2 Suggestions for Future Work

In the following sections, suggestions for future work are described.

6.2.1 High Resolution XTEM of GaSb/GaAs Quantum Dots

In our GaSb/GaAs QD computational work, we have predicted the influence of misfit dislocations on the band alignment. We report that the dislocation-induced strain-fields reduce the energy of the GaSb CB edge in the vicinity of the dislocation cores, resulting in a local type I offset. Using cross-sectional high-resolution transmission electron microscopy (HRTEM), InSb QDs grown on and capped with GaAs are shown to include dislocations at the top and bottom interfaces between InSb QD and GaAs.[1] In addition, using Peak Pairs analysis[2] on the HRTEM image of InSb QDs for local strain map calculations, an average lattice mismatch of ~7% between GaAs and In(GaAs)Sb QDs is reported, similar to the 7% lattice mismatch between GaSb QD and GaAs; thus, we expect dislocation-induced strain relaxation of GaSb/GaAs QDs via dislocation loops.[3,4] However, to our knowledge, such a configuration has not been reported exerpimentally for GaAs/GaSb. Therefore, an experimental validation of dislocation cores at the bottom and top GaSb/GaAs QD interfaces is needed, which may be provided via high resolution XTEM studies. XTEM samples were thinned down and mounted on Cu rings, where ion

milling was used to create a hole in the middle of the sample. Further ion milling damage must be made to the XTEM sample to thin down the sample thickness in the vicinity of QD.

6.2.2 XSTM on Multi-layer InGaN/GaN QDs

XSTM multi-layer InGaN/GaN QD samples were grown on a free-standing GaN substrate with a similar growth condition as described in section 4.3, but with seven superlattice layers of InGaN/GaN QDs and a thick 500 nm GaN capping layer. Six samples were grown in Vecco Gen 2 and Veeco Gen 930. Using the lapping and scribing tool in LNF at the University of Michigan described in Chapters 2.6.2 and 2.6.3, approximately 30 XSTM samples were prepared and cleaved in an ultra-high vacuum, and the exposed surface was investigated.

Figure 6.1 shows XSTM images of InGaN/GaN QDs grown in (a) Vecco Gen 2 and (b) Veeco Gen 930, grown by T. Frost at Univ. of Michigan. Both XSTM images clearly show the InGaN QDs and the GaN matrices. Furthermore, a vertical stacking of InGaN QDs are apparent, as discussed in section 4.2. Fig. 6.2 presents STS measurements taken on the InGaN QD and GaN. The STS data suggests a band gap energy of 3.4 ± 0.2 eV for GaN and 1.5 ± 0.2 eV for InGaN QD. However, the STS spectrum is noisy due to unstable tip-surface interaction during the collection of the STS data. Further XSTM and STS experiments on multi-layer InGaN/GaN QDs may provide insight on the influence of vertical stacking on the band structure of InGaN QDs, as a clear change in electronic

structure of InGaN QDs were observed between single and multi-layer InGaN QDs on GaN/AlGaN/sapphire substrate.

6.2.3 Si Dopant and Indium Distribution within InAs QDs

Self-assembled semiconductor quantum dots (QDs) are promising materials for optoelectronic devices, including solar cells, lasers, photodetectors, light emitting diodes, and thermoelectric generators.[1-8] Due to limitations of existing local probe techniques,[9] studies on the carrier concentration in the vicinity of a QD system is challenging. Using capacitance-voltage measurements on InAs/GaAs QD heterostructures, a carrier depletion near the InAs QDs has been reported.[10–12] Due to the fact that carrier depletion is reported for InAs coverage beyond 3 monolayers, it is often speculated that the strain relaxation-induced defects act as carrier traps.[13-15] However, the spatial distribution of carriers within a single QD and on the wetting layer has yet not been reported.

A recent publication from a member of the group, J. Walrath, presents a study of nanoscale probing of thermoelectric properties of Si doped InAs/GaAs QD.[15] In the work, a reduced carrier concentration within the InAs QD was suggested. The findings are in a good agreement with the "self-purification" model,[13] which describes that dopant incorporation on the QD surface is energetically favored over its incorporation at the QD center. Thus, atom probe tomography was utilized for examining the Si dopant distribution.

Preliminary work on APT experiments on InAs/GaAs QDs have been performed both by the author of the dissertation and a member of the group, J. Walrath. A commercial CAMECA LEAP 4000X Si system was used to obtain the APT results presented in this

thesis. Ions were collected from prepared sample tips both in laser and voltage mode with settings of detection rate of 0.5 %, pulse rate of 120 kHz, and an evaporation field of 15 V/nm. Shown in Fig. 6.3 is the reconstructed APT data of the InAs/GaAs QDs collected in laser mode. Indium atoms are plotted as blue dots and isosurfaces of $x_{In} > 0.1$ are plotted as yellow dots. Our data reveals a higher density of Si atoms within the InAs QDs compared to that of the GaAs spacers, contrary to our SThem findings.[15] Furthermore, the InAs wetting layers had the highest density of Si atoms. It is likelt that a fraction of Si atoms within the InAs QDs are electronically inactive. Figure 6.4 shows the reconstructure APT data of the InAs/GaAs QDs collected in voltage mode. However, further statistical analysis is needed for the data set.

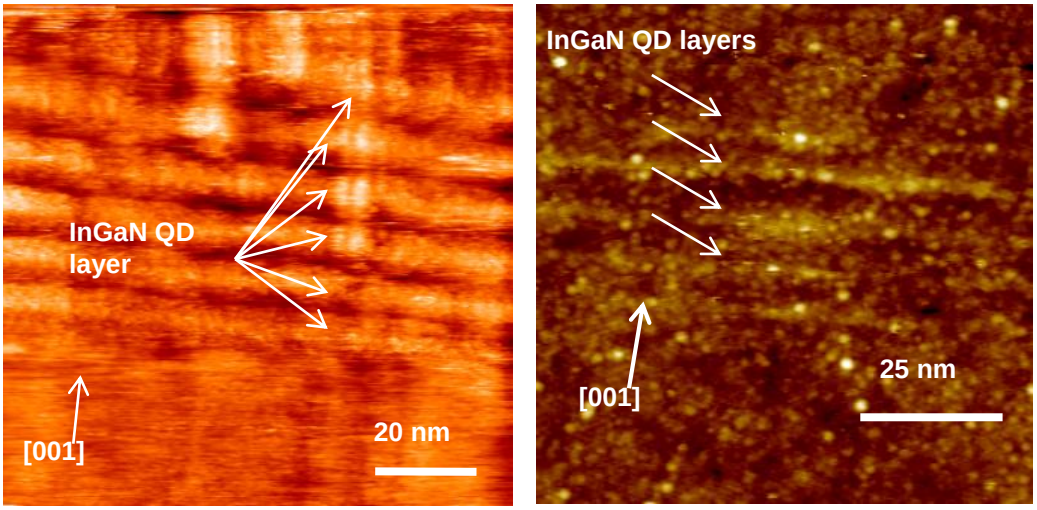

Fig. 6.1: Cross-sectional scanning tunneling microscopy (XSTM) image of $In_{0.24}Ga_{0.76}N$ / GaN QDs, grown in (a) Vecco Gen 2 and (b) Veeco Gen 930 by T. Frost in Prof. Bhattacharya's group at the University of Michigan.

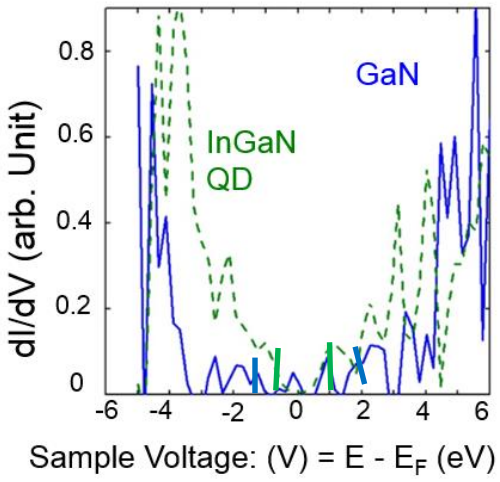

Fig. 6.2: STS measurement on InGaN QD and GaN matrix. The STS data suggests a band gap of 3.4 eV for GaN and 1.5 eV for InGaN QD.

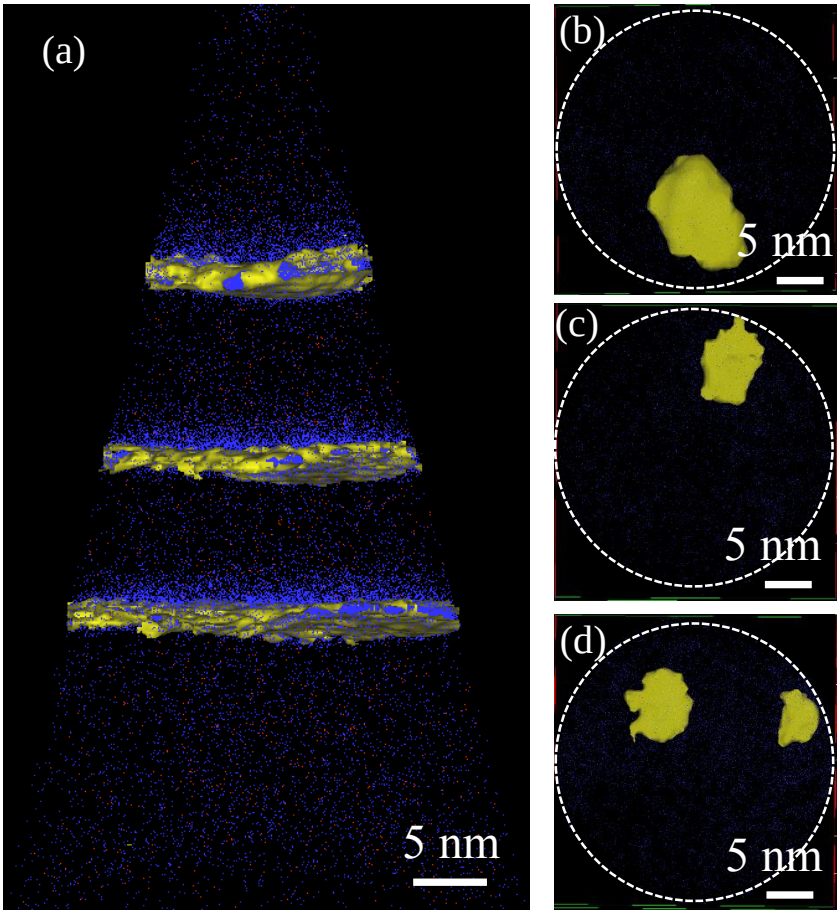

Fig. 6.3: (a) Reconstructed atom probe tomography data of InAs/GaAs QDs collected in Laser mode. Indium atoms are plotted as blue dots and isosurfaces of $x_{In} > 0.1$ are plotted as yellow dots. A cross-section of the reconstructed data of (a) top, (b) middle, and (c) bottom InAs QD layer. Isosurfaces of $x_{In} > 0.1$, plotted as yellow dots, reveal the InAs QDs of ~ 6 nm diameter.

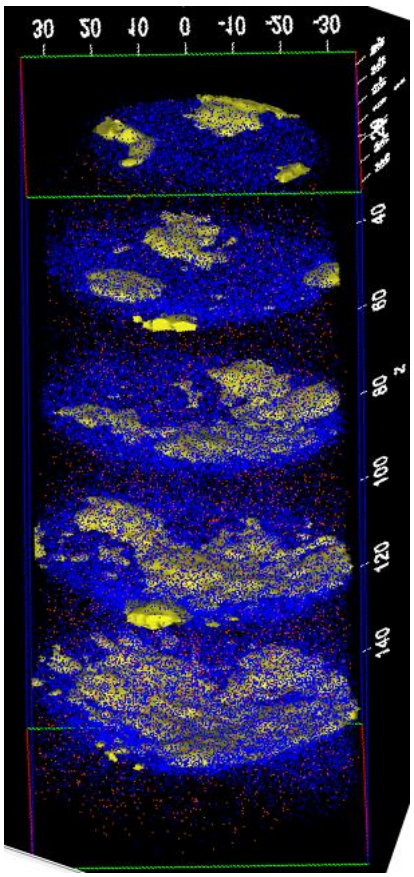

Fig. 6.4: Reconstructed atom probe tomography data of InAs/GaAs QDs collected in Voltage mode. Indium atoms are plotted as blue dots and isosurfaces of $x_{In} > 0.1$ are plotted as yellow dots.

6.3 References

[1]A. Marti, E. Antolin, C. R. Stanley, C. D. Farmer, N. Lopez, P. Diaz, E. Canovas, P. G. Linares, and A. Luque, *Phys. Rev. Lett.* **97**, 247701 (2006).

[2]S. Huang, A. V. Semichaevsky, L. Webster, H. T. Johnson, and R. S. Goldman, *J. Appl. Phys.* **110**, 073105 (2011).

[3]L. Huffaker, G. Park, Z. Zou, O. B. Shchekin, and D. G. Deppe, *Appl. Phys. Lett.* **73**, 2564 (1998).

[4]J. Phillips, K. Kamath, and P. Bhattacharya, *Appl. Phys. Lett.* **72**, 2020 (1998).

[5]Z. Y. Zhao, C. Yi, K. R. Lantz, and A. D. Stiff-Roberts, *Appl. Phys. Lett.* **90**, 233511 (2007).

[6]N. M. Park, T. S. Kim, and S. J. Park, *Appl. Phys. Lett.* **78**, 2575 (2001).

[7]J. X. Chen, A. Markus, A. Fiore, U. Oesterle, R. P. Stanley, J. F. Carlin, R. Houdre, M. Ilegems, L. Lazzarini, L. Nasi, M. T. Todaro, E. Piscopiello, R. Cingolani, M. Catalano, J. Katcki, and J. Ratajczak, *J. Appl. Phys.* **91**, 6710 (2002).

[8]G. D. Mahan and J. O. Sofo, *Proc. Natl. Acad. Sci. U. S. A.* **93**, 7436 (1996).

[9]P. De Wolf, R. Stephenson, T. Trenkler, T. Clarysse, T. Hantschel, and W. Vandervorst, *J. Vac. Sci. Technol., B* **18**, 361 (2000).

[10]J. S. Wang, J. F. Chen, J. L. Huang, P. Y. Wang, and X. J. Guo, *Appl. Phys. Lett.* **77**, 3027 (2000).

[11]J. F. Chen, R. S. Hsiao, Y. P. Chen, J. S. Wang, and J. Y. Chi, *Appl. Phys. Lett.* **87**, 141911 (2005).

[12]J. C. Rimada, M. Prezioso, L. Nasi, E. Gombia, R. Mosca, G. Trevisi, L. Seravalli, P. Frigeri, C. Bocchi, and S. Franchi, *Mater. Sci. Eng., B* **165**, 111 (2009).

[13]P. Frigeri, L. Nasi, M. Prezioso, L. Seravalli, G. Trevisi, E. Gombia, R. Mosca, F. Germini, C. Bocchi, and S. Franchi, *J. Appl. Phys.* **102**, 083506 (2007).

[14]E. Gombia, R. Mosca, S. Franchi, P. Frigeri, and C. Ghezzi, *Mater. Sci. Eng., C* **26**, 867 (2006).

[15]J. C. Walrath, Yen-Hsiang Lin, S. Huang, and R. S. Goldman, *Appl. Phys. Lett.* **106**, 192101 (2015)

APPENDICES

Appendix A

Scanning Tunneling Spectroscopy Data Analysis

In this appendix, the analysis procedures for the scanning tunneling spectroscopy data discussed throughout this dissertation are described. The normalization of STS data and the algorithm for determining the band edges are described in this section. All of the work is based on earlier works A. Cummel, M. Beck, and R. M. Feenstra.[1,2,3]

A.1 Normalization Procedure

$\frac{\overline{I}}{V} = \frac{1}{2\Delta V}\int_{-\infty}^{\infty}\left\{I(V')/V'\right\}e^{\frac{-\left|V'-V\right|}{\Delta V}}dV'$The STS data, i.e. the tunneling current (I) and the conductance (dI/dV), are collected with a variable-separation STS method, as described in Section 2.7. Due to the fact that I/V may approach to zero faster than dI/dV, the normalized conductance, [dI/dV]/[I/V], may diverge. Therefore, the I(V) curve is broadened by convoluting it with a Gaussian function:[3,4]

(A.1)

$\frac{dI/dV}{\overline{I/V}}$with a typical value of ΔV = 1 Volt. The normalization of the conductance is performed by:

(A.2)

During the calculation of normalized conductance, a magnitude and an offset is subtracted and divided. The magnitude and offset values are obtained by collecting a STS spectrum with a constant separation STS method. The offset is obtained by computing the derivative of the current spectrum, I(V), and subtracting it by the conductance. In addition, the magnitude is obtained by computing the derivative of the currnet spectrum and dividing it by the conductance minus the offset.

The band edge determination of STS spectrum on InGaAs(Sb)N was performed by a simple method. First, the normalized conductance from GaAs was was subtracted by a fixed conductance level such that the minimum normalized conductance was 0. Then, a typical normalized conductance value, *h*, was found, where the voltages corresponding to *h* yielded a band gap of 2.4 eV. The STS spectrum on InGaAs(Sb)N was also revealed, and the voltage value corresponding to the previously found *h* were considered to be the band edges.

For GaSb/GaAs QD and InGaN/GaN QD experiments, data points at the edges of the spectrum were removed. The remaining conductance data were fit with a linear least-squares fit. The removal of edge points of the data was repeated until the fitted line had a lower slope and offset than user defined values. The standard deviation of the remaining data was calculated, and was used as a band edge criterion. Any conductance larger than the standard deviation was considered "conductive". The voltage values corresponding to the "conductive" conductance spectrum are considered to be in the band, and the valence band (conduction band) was determined to be the maximum (minimum) voltage value below (above) the Fermi energy, which is V = 0 in our STS data.

A.2 Normalization Code

The normalization code was re-written in Matlab such that a user can perform the above steps with a fast feed-back on the results. This is important during STS measurements, when the tip may "drift" away from the layers of interest.

The first matlab code, "ConstantSeparation_Offset_Mag", calculates the offset and magnitude from a constant-separation STS spectrum.

```
function [] = ConstantSeparation()

i=1;
list = dir('*.txt');
n = length(list);

   I_data = importdata(list(2*i,1).name);
   DIDV_data = importdata(list(2*i-1,1).name);
   %Save the variables in vectors
   v = (I_data(:,1));
   I = (I_data(:,2));
   didv = (DIDV_data(:,2));
   dofI = [];

 for i = 2:length(v)
    dofI = [ dofI; (I(i)-I(i-1))/(v(i)-v(i-1)) ];
 end
 off = -dofI(length(v)/2+1)+didv(length(v)/2)
 disp('offset = ');
 disp(off );

 dofI_corrected = dofI - off;
 mag = didv(length(v)/2) / dofI(length(v)/2+1);
 disp('magnitude = ');
 disp(mag);
```

The second matlab code, "Normalization_Alex_Chang_VS_STS", computes the band edges for the user.

```
function [] = Normalization_Alex_Chang()


%This code is written by Alex Chang, Goldman's Group at University of
%Michigan. This code is based on previous work of M. Beck.


%Generate a list of data files that are in the directory.
list = dir('*.txt'); n = length(list);
%i is the numbering system of the list of data files. Start off with the
%first file, and the user will be enabled to choose when the program is
%run.
i = 1;


%import the voltage values and the I(V) and dI/dV readings
iv = importdata(list(2*i).name); aux = importdata(list(2*i-1).name);

%Save the variables in vectors
v = (iv(:,1)); I = (iv(:,2))*1e9; didv = (aux(:,2));

%All of our STS data are collected by varying the applied Bias voltage from
%negative to positive and from positive to negative.
%Separate the two sets of vectors into both forward (from negative bias
%to positive bias).

%When Bias Voltage varies from negative to positive, then positive to
%negative
if v(1)<0
   length_halving = length(didv)/2;
   I_forward = I(1:length_halving);
   I_backward = I(2*length_halving:-1:length_halving+1);

   didv_forward = didv(1:length_halving);
   didv_backward = didv(2*length_halving:-1:length_halving+1);

   v_forward = v(1:length_halving);
   v_backward = v(2*length_halving:-1:length_halving+1);
%When Bias Voltage varies from positive to negative, then negative to
%positive
else
   length_halving = length(didv)/2;
   I_forward = I(length_halving:-1:1);
   I_backward = I(length_halving+1:2*length_halving);
```

```
   didv_forward = didv(length_halving:-1:1);
   didv_backward = didv(length_halving+1:2*length_halving);

   v_forward = v(length_halving:-1:1);
   v_backward = v(length_halving+1:2*length_halving);
end

v_forward = v; I_forward = I; didv_forward = didv;

% GUI Part

%   Creates the figure
S.fh = figure('units','pixels',...
            'position',[100 10 1150 680],...
            'menubar','none',...
            'name','Normalization Code',...
            'numbertitle','off',...
            'resize','off');

%   Creates borders around slider sets
%   Must be done before other code in order to keep these in background
S.b1 = uicontrol('style','edit',...
              'unit', 'pix',...
              'enable', 'inactive',...
              'position', [5 10 310 150],...
              'backgroundc', get(S.fh,'color'));
S.b2 = uicontrol('style','edit',...
              'unit', 'pix',...
              'enable', 'inactive',...
              'position', [5 170 310 150],...
              'backgroundc', get(S.fh,'color'));
S.b3 = uicontrol('style','edit',...
              'unit', 'pix',...
              'enable', 'inactive',...
              'position', [5 330 310 150],...
              'backgroundc', get(S.fh,'color'));
S.b4 = uicontrol('style','edit',...
              'unit', 'pix',...
              'enable', 'inactive',...
              'position', [5 490 310 150],...
              'backgroundc', get(S.fh,'color'));
S.b5 = uicontrol('style','edit',...
              'unit', 'pix',...
              'enable', 'inactive',...
              'position', [325 10 310 150],...
              'backgroundc', get(S.fh,'color'));
```

```
S.b6 = uicontrol('style','edit',...
            'unit', 'pix',...
            'enable', 'inactive',...
            'position', [325 170 310 150],...
            'backgroundc', get(S.fh,'color'));
S.b7 = uicontrol('style','edit',...
            'unit', 'pix',...
            'enable', 'inactive',...
            'position', [325 330 310 150],...
            'backgroundc', get(S.fh,'color'));
S.b8 = uicontrol('style','edit',...
            'unit', 'pix',...
            'enable', 'inactive',...
            'position', [325 490 310 150],...
            'backgroundc', get(S.fh,'color'));

%   Sets axes object
S.ax = axes('units','pixels',...
        'position',[650 50 480 250]);
S.ax2 = axes('units','pixels',...
        'position',[650 310 480 250]);


%   Sets text boxes above states properties
S.Convolution1 = uicontrol('style','text',...
            'unit','pix',...
            'position',[10 130 250 20],...
            'fontsize',13,...
            'BackgroundColor',[.8 .8 .8],...
            'string','Convolution-Gaussian Parameters');
S.Convolution2 = uicontrol('style','text',...
            'unit','pix',...
            'position',[10 290 250 20],...
            'fontsize',13,...
            'BackgroundColor',[.8 .8 .8],...
            'string','Convolution-Gaussian Parameters');
…..

%   Code for the popup menu
S.pp = uicontrol('style','pop',...
            'unit','pix',...
            'position',[10 520 280 20],...
            'backgroundc',get(S.fh,'color'),...
            'fontsize',10,'fontweight','bold',...
            'string',{'Forward Scan';'Backward Scan'},...
            'value',1);
```

```
pp_string = [];
for j= 1:n/2;
   pp_string = [pp_string j];
end

…..

%   Delta-V : Width of Gaussian Curve
S.sl = uicontrol('style','slide',...z
               'unit','pix',...
               'position',[35 20 100 20],...
               'min',0,'max',5,'val',0.5);
S.ed(1) = uicontrol('style','edit',...
                 'unit','pix',...
                 'position',[15 20 20 20],...
                 'fontsize',10,...
                 'string','0');   % Displays the min.
S.ed(2) = uicontrol('style','edit',...
                 'unit','pix',...
                 'position',[15 50 140 20],...
                 'fontsize',10,...
                 'string','0.5');  % Displays the value.
S.ed(3) = uicontrol('style','edit',...
                 'unit','pix',...
                 'position',[135 20 20 20],...
                 'fontsize',10,...
                 'string','5');    % Displays the max.
S.tex = uicontrol('style','text',...
               'unit','pix',...
               'position',[15 70 140 40],...
               'fontsize',10,...
               'BackgroundColor',[.8 .8 .8],...
               'string','Delta V - Gaussian Width');

…

% push botton that enables the user to save data
S.pb = uicontrol('style','push',...
               'units','pixels',...
               'position',[330 50 120 30],...
               'fontsize',10,...
               'string','Press to Save data',...
               'callback',{@pb_call,S});

% push botton that enables the user to update plots
S.pb2 = uicontrol('style','push',...
```

```
            'units','pixels',...
            'position',[330 10 150 30],...
            'fontsize',10,...
            'string','Press to Update Plots',...
            'callback',{@pb_call1,S});


 % END SLIDER DEFINTIONS


%   Gets values from sliders
S.plot1 = get(S.sl,{'min','value','max'}); S.plot2 = get(S.sl2,{'min','value','max'});
S.plot3 = get(S.sl3,{'min','value','max'}); S.plot4 = get(S.sl4,{'min','value','max'});
S.plot5 = get(S.sl5,{'min','value','max'}); S.plot6 = get(S.sl6,{'min','value','max'});
S.plot7 = get(S.sl7,{'min','value','max'}); S.plot8 = get(S.sl8,{'min','value','max'});
S.plot9 = get(S.sl9,{'min','value','max'}); S.plot10 = get(S.sl10,{'min','value','max'});

plot(S.ax2,v_forward,I_forward);

datacursormode on
v_noise_min = S.plot5{2}; v_noise_max = S.plot6{2};
x_phys_noise = []; y_val1_noise = [];
% Search for the points that correspond to this range
for i = 1: length(v_forward)
   if(v_forward(i) >= v_noise_min && v_forward(i) <= v_noise_max )
      x_phys_noise = [x_phys_noise, v_forward(i)];
      y_val1_noise = [y_val1_noise, I_forward(i)];
   end
end
% Find the average offset.
offset = sum(y_val1_noise) / length(y_val1_noise);
I_forward = I_forward - offset;

% Evaluate the standard deviation of the I(V) values. Delete points that
% are within two stnadard deviation. Replace them with 0.
y_val1_noise = y_val1_noise - offset;
sum_standard_deviation = 0;
for i = 1:length(y_val1_noise)
   sum_standard_deviation = sum_standard_deviation + y_val1_noise(i)^2;
end
standard_deviation = sqrt(sum_standard_deviation / length(y_val1_noise) );
for i = 1:length(I_forward)
   if(abs(I_forward(i))<= standard_deviation)
      I_forward(i) = 0;
   end
```

```
end

% Find the first and last recurrance of zero, and delete all points
% inbetween by replacing them into zero.
for i = 1:length(I_forward)
   if(I_forward(i) == 0)
      x_min_pts_delete = i;
      break;
   end
end
for i = length(I_forward):-1:1
   if(I_forward(i) == 0)
      x_max_pts_delete = i;
      break;
   end
end
for i = x_min_pts_delete:x_max_pts_delete
   I_forward(i) = 0;
end

% Now we want to take in account of the broadening effect. Following the
% equation from Vaishno's thesis at page 34, convolution is conducted.

% Inpute the delta_z value from the user.
delta_V = S.plot1{2}; min_v = S.plot3{2}; max_v=S.plot4{2}; dv=S.plot2{2};

% Give a range for voltage that will be used in the convolution.
v_convolution = min_v:dv: max_v; IoverV_normalized = [];

% Compute the convolution with the given paramters inputted by the user.
for j = 1:length(v_convolution)
   summation = 0;
   for i = 1: length(v_forward)
      summation = summation + (I_forward(i)/v_forward(i))*exp(-1*abs(v_forward(i)-
v_convolution(j))/delta_V)*dv;
   end
   summation = summation / (2*delta_V);

   IoverV_normalized = [IoverV_normalized, summation];
end

IoverV_normalized = IoverV_normalized/(0.1*(max(IoverV_normalized)-
min(IoverV_normalized)));

useful_v = [];
useful_i = [];
```

```
for i=1:length(v_forward)
   for j = 1:length(v_convolution)-1
      if v_convolution(j) <=v_forward(i) && v_convolution(j+1) > v_forward(i)
         useful_v = [useful_v; v_convolution(j)];
         useful_i = [useful_i; IoverV_normalized(j)];
      end
   end
end

normalized_forward = didv_forward./useful_i; x= useful_v; y= normalized_forward;
plot(S.ax,x,y);

datacursormode on

%band edge determination process.
v_noise_min = S.plot7{2}; v_noise_max = S.plot8{2};
x_phys_noise = []; y_val1_noise = [];

for i = 1: length(useful_v)
   if (useful_v(i) >= v_noise_min && useful_v(i) <= v_noise_max )
      x_phys_noise = [ x_phys_noise, useful_v(i) ];
      y_val1_noise = [y_val1_noise, normalized_forward(i) ];
   end
end

criteria_s = S.plot9{2}; criteria_h = S.plot10{2}; flag = 0;
while flag ==0

   P = polyfit(x_phys_noise, y_val1_noise, 1);

   if P(1) < criteria_s && P(2) < criteria_h
      flag =1;
   end

   if length(y_val1_noise)<2
      set(S.text26, 'string', 'Band Edge determining criteria failed. Use a larger criteria');
      break;
   end

   if flag == 0
      y_val1_noise = y_val1_noise(2:length(y_val1_noise)-1);
      x_phys_noise = x_phys_noise(2:length(x_phys_noise)-1);
   end
end
```

```
offset = sum(y_val1_noise) / length(y_val1_noise);
y_val1_noise = y_val1_noise - offset; sum_standard_deviation = 0;
for i = 1:length(y_val1_noise)
   sum_standard_deviation = sum_standard_deviation + y_val1_noise(i)^2;
end
standard_deviation = sqrt(sum_standard_deviation / length(y_val1_noise) );
standard_deviation_double = 2* standard_deviation;

normalized_forward = normalized_forward - offset;

data_within_band = [];
for i=1:length(normalized_forward)
   if(abs(normalized_forward(i)) <= standard_deviation)
      data_within_band = [data_within_band , useful_v(i)];
   end
end
VBE = min(data_within_band);
CBE = max(data_within_band);
set(S.text16, 'string', num2str(VBE));
set(S.text17, 'string', num2str(CBE));
set(S.text18, 'string', num2str(CBE-VBE));

data_within_band_double = [];
for i=1:length(normalized_forward)
   if(abs(normalized_forward(i)) <= standard_deviation_double)
      data_within_band_double = [data_within_band_double , useful_v(i)];
   end
end
VBE2 = min(data_within_band_double);
CBE2 = max(data_within_band_double);

set(S.text22, 'string', num2str(abs(VBE-VBE2)));
set(S.text23, 'string', num2str(abs(CBE-CBE2)));
set(S.text24, 'string', num2str(abs(CBE-CBE2+VBE-VBE2)));


%   Updates plot after slider change
set([S.ed(:);S.sl],'call',{@sl_call,S});        % Shared Callback.
set([S.ed2(:);S.sl2],'call',{@sl_call2,S});     % Shared Callback.
set([S.ed3(:);S.sl3],'call',{@sl_call3,S});     % Shared Callback.
set([S.ed4(:);S.sl4],'call',{@sl_call4,S});     % Shared Callback.
set([S.ed5(:);S.sl5],'call',{@sl_call5,S});     % Shared Callback.
set([S.ed6(:);S.sl6],'call',{@sl_call6,S});     % Shared Callback.
set([S.ed7(:);S.sl7],'call',{@sl_call7,S});     % Shared Callback.
set([S.ed8(:);S.sl8],'call',{@sl_call8,S});     % Shared Callback.
```

```
set([S.ed9(:);S.sl9],'call',{@sl_call9,S});      % Shared Callback.
set([S.ed10(:);S.sl10],'call',{@sl_call10,S});      % Shared Callback.

%   Callback function for saving plot picture
function [] = fm_call(varargin)
   % Callback for the figure menu.
      N = inputdlg('Enter a file name.','FileName'); % Get a name.
      F = getframe(S.fh,get(S.ax,'OuterPosition') + [80 30 -190 -58]);  % Only want to get
axes.
      FMT = S.FMT{varargin{1}==S.fm};  % User's format choice.
      imwrite(F.cdata,[N{1},'.',FMT],FMT)  % Write the image.
end

end


function [] = sl_call(varargin)
   % Callback for the edit box and slider.
   [h,S] = varargin{[1,3]};  % Get calling handle and structure.
   SL = get(S.sl,{'min','value','max'});  % Get the slider's info.
   E = str2double(get(h,'string'));  % Numerical edit string.

   switch h  % Who called?
      case S.ed(1)
         if E <= SL{2}
            set(S.sl,'min',E)  % E is less than current value.
            Updateplot(S)
         elseif E < SL{3}
            set(S.sl,'val',E,'min',E) % E is less than max value.
            set(S.ed(2),'string',E) % Set the current display.
            Updateplot(S)
         else
            set(h,'string',SL{1}) % Reset the value.
            Updateplot(S)
         end
      case S.ed(2)
         if E >= SL{1} && E <= SL{3}
            set(S.sl,'value',E)  % E falls within range of slider.
            Updateplot(S)
         else
            set(h,'string',SL{2}) % User tried to set slider out of range.
            Updateplot(S)
         end
      case S.ed(3)
         if E >= SL{2}
            set(S.sl,'max',E)  % E is less than current value.
```

```
            Updateplot(S)
        elseif E > SL{1}
            set(S.sl,'val',E,'max',E) % E is less than max value.
            set(S.ed(2),'string',E) % Set the current display.
            Updateplot(S)
        else
            set(h,'string',SL{3}) % Reset the value.
            Updateplot(S)
        end
    case S.sl
        set(S.ed(2),'string',SL{2}) % Set edit to current slider
        Updateplot(S)
    otherwise
        % Do nothing
  end
end

…

%   Base function to update the plot as sliders change
function[] = Updateplot(varargin)
   [S] = varargin{[1]};
   global i;
   S.plot1 = get(S.sl,{'min','value','max'});
   S.plot2 = get(S.sl2,{'min','value','max'});
   S.plot3 = get(S.sl3,{'min','value','max'});
   S.plot4 = get(S.sl4,{'min','value','max'});
   S.plot5 = get(S.sl5,{'min','value','max'});
   S.plot6 = get(S.sl6,{'min','value','max'});
   S.plot7 = get(S.sl7,{'min','value','max'});
   S.plot8 = get(S.sl8,{'min','value','max'});
   S.plot9 = get(S.sl9,{'min','value','max'});
   S.plot10 = get(S.sl10,{'min','value','max'});

   % P = 1 if forward   P = 2 if backward
   P = get(S.pp,'value');
   %P2 = i
   P2 = get(S.pp2,'value');

i = P2;
list = dir('*.txt');
n = length(list);

%import the voltage values and the I(V) and dI/dV readings
iv = importdata(list(2*i).name);
aux = importdata(list(2*i-1).name);
```

```
%Save the variables in vectors
v = (iv(:,1));
I = (iv(:,2))*1e9;
didv = (aux(:,2));

%All of our STS data are collected by varying the applied Bias voltage from
%negative to positive and from positive to negative.
%Separate the two sets of vectors into both forward (from negative bias
%to positive bias).

%When Bias Voltage varies from negative to positive, then positive to
%negative
if v(1)<0
   length_halving = length(didv)/2;     I_forward = I(1:length_halving);
   I_backward = I(2*length_halving:-1:length_halving+1);

   didv_forward = didv(1:length_halving);
   didv_backward = didv(2*length_halving:-1:length_halving+1);

   v_forward = v(1:length_halving);
   v_backward = v(2*length_halving:-1:length_halving+1);
%When Bias Voltage varies from positive to negative, then negative to
%positive
else
   length_halving = length(didv)/2;     I_forward = I(length_halving:-1:1);
   I_backward = I(length_halving+1:2*length_halving);

   didv_forward = didv(length_halving:-1:1);
   didv_backward = didv(length_halving+1:2*length_halving);

   v_forward = v(length_halving:-1:1);
   v_backward = v(length_halving+1:2*length_halving);
end

%Separate the vectors into forward and backward
length_halving = length(didv)/2; I_forward = I(1:length_halving);
I_backward = I(length_halving+1:2*length_halving);

didv_forward = didv(1:length_halving);
didv_backward = didv(length_halving+1:length_halving*2);

v_forward = v(1:length_halving);
v_backward = v(length_halving+1:2*length_halving);

if v_forward(1) >0
```

```
   temp = v_backward;     v_backward = v_forward;     v_forward = temp;
   temp2 = didv_backward;     didv_backward = didv_forward;     didv_forward = temp2;
   temp3 = I_backward;     I_backward = I_forward;     I_forward = temp3;
end

if P == 2
   I_forward = I_backward;    v_forward = v_backward;    didv_forward = didv_backward;
end


v_forward = v; I_forward = I; didv_forward = didv; offset = 2.4106; magnitude = 3.9745;
didv_forward = (didv_forward-offset)/magnitude;

plot(S.ax2,v_forward,I_forward);

datacursormode on
v_noise_min = S.plot5{2}; v_noise_max = S.plot6{2};
x_phys_noise = []; y_val1_noise = [];

% Search for the points that correspond to this range
for i = 1: length(v_forward)
   if(v_forward(i) >= v_noise_min && v_forward(i) <= v_noise_max )
      x_phys_noise = [x_phys_noise, v_forward(i)];
      y_val1_noise = [y_val1_noise, I_forward(i)];
   end
end
% Find the average offset.
offset = sum(y_val1_noise) / length(y_val1_noise);
I_forward = I_forward - offset;

% Evaluate the standard deviation of the I(V) values. Delete points that
% are within two stnadard deviation. Replace them with 0.
y_val1_noise = y_val1_noise - offset;
sum_standard_deviation = 0;
for i = 1:length(y_val1_noise)
   sum_standard_deviation = sum_standard_deviation + y_val1_noise(i)^2;
end
standard_deviation = sqrt(sum_standard_deviation / length(y_val1_noise) );
for i = 1:length(I_forward)
   if(abs(I_forward(i))<= standard_deviation)
      I_forward(i) = 0;
   end
end

% Find the first and last recurrance of zero, and delete all points
% inbetween by replacing them into zero.
```

```
for i = 1:length(I_forward)
   if(I_forward(i) == 0)
      x_min_pts_delete = i;
      break;
   end
end
for i = length(I_forward):-1:1
   if(I_forward(i) == 0)
      x_max_pts_delete = i;
      break;
   end
end
for i = x_min_pts_delete:x_max_pts_delete
   I_forward(i) = 0;
end

% Now we want to take in account of the broadening effect. Following the
% equation from Vaishno's thesis at page 34, convolution is conducted.

% Inpute the delta_z value from the user.
delta_V = S.plot1{2}; min_v = S.plot3{2}; max_v=S.plot4{2}; dv=S.plot2{2};

% Give a range for voltage that will be used in the convolution.
v_convolution = min_v:dv: max_v;
IoverV_normalized = [];

% Compute the convolution with the given paramters inputted by the user.
for j = 1:length(v_convolution)

   summation = 0;
   for i = 1: length(v_forward)
      summation = summation + (I_forward(i)/v_forward(i))*exp(-1*abs(v_forward(i)-
v_convolution(j))/delta_V)*dv;
   end
   summation = summation / (2*delta_V);

   IoverV_normalized = [IoverV_normalized, summation];
end

IoverV_normalized = IoverV_normalized/(0.1*(max(IoverV_normalized)-
min(IoverV_normalized)));

useful_v = [];
useful_i = [];

for i=1:length(v_forward)
```

```
    for j = 1:length(v_convolution)-1
        if v_convolution(j) <=v_forward(i) && v_convolution(j+1) > v_forward(i)
            useful_v = [useful_v; v_convolution(j)];
            useful_i = [useful_i; IoverV_normalized(j)];
        end
    end
end

normalized_forward = didv_forward./useful_i;
x= useful_v; y= normalized_forward; plot(S.ax,x,y);

datacursormode on

%band edge determination process.
v_noise_min = S.plot7{2}; v_noise_max = S.plot8{2};
x_phys_noise = []; y_val1_noise = [];

for i = 1: length(useful_v)
    if (useful_v(i) >= v_noise_min && useful_v(i) <= v_noise_max )
        x_phys_noise = [ x_phys_noise, useful_v(i) ];
        y_val1_noise = [y_val1_noise, normalized_forward(i) ];
    end
end

criteria_s = S.plot9{2}; criteria_h = S.plot10{2};
flag = 0;
set(S.text26, 'string', 'Band Edge determining criteria worked')
while flag ==0

    P = polyfit(x_phys_noise, y_val1_noise, 1);

    if P(1) < criteria_s && P(2) < criteria_h
        flag =1;
    end

    if length(y_val1_noise)<2
        set(S.text26, 'string', 'Band Edge determining criteria failed. Use a larger criteria');
        break;
    end

    if flag == 0
        y_val1_noise = y_val1_noise(2:length(y_val1_noise)-1);
        x_phys_noise = x_phys_noise(2:length(x_phys_noise)-1);
    end
end
```

```
offset = sum(y_val1_noise) / length(y_val1_noise);
y_val1_noise = y_val1_noise - offset;
sum_standard_deviation = 0;
for i = 1:length(y_val1_noise)
   sum_standard_deviation = sum_standard_deviation + y_val1_noise(i)^2;
end
standard_deviation = sqrt(sum_standard_deviation / length(y_val1_noise) );
standard_deviation_double = 2* standard_deviation;

normalized_forward = normalized_forward - offset;

data_out_band = [];
for i=1:length(normalized_forward)
   if(abs(normalized_forward(i)) >= standard_deviation)
      data_out_band = [data_out_band , useful_v(i)];
   end
end
disp(data_out_band)
data_out_pos = [];
data_out_neg = [];
for k = 1:length(data_out_band)
  if data_out_band(k) >0
     data_out_pos = [ data_out_pos , data_out_band(k)];
  else
     data_out_neg = [ data_out_neg , data_out_band(k)];
  end
end

CBE = min(data_out_pos); VBE = max(data_out_neg);
set(S.text16, 'string', num2str(VBE));
set(S.text17, 'string', num2str(CBE));
set(S.text18, 'string', num2str(CBE-VBE));

data_out_band_double = [];
for i=1:length(normalized_forward)
   if(abs(normalized_forward(i)) >= standard_deviation_double)
      data_out_band_double = [data_out_band_double , useful_v(i)];
   end
end

data_out_pos = []; data_out_neg = [];
for k = 1:length(data_out_band_double)
  if data_out_band_double(k) <0
     data_out_pos = [ data_out_pos , data_out_band_double(k)];
  else
```

```
      data_out_neg = [ data_out_neg , data_out_band_double(k)];
   end
end

CBE2 = min(data_out_pos); VBE2 = max(data_out_neg);

set(S.text22, 'string', num2str(abs(VBE-VBE2)));
set(S.text23, 'string', num2str(abs(CBE-CBE2)));
set(S.text24, 'string', num2str(abs(CBE-CBE2+VBE-VBE2)));

end

function [] = pb_call(varargin)
% Callback for the pushbutton.

    S = varargin{3};  % Get the structure.
    global i;
    S.plot1 = get(S.sl,{'min','value','max'});
    S.plot2 = get(S.sl2,{'min','value','max'});
    S.plot3 = get(S.sl3,{'min','value','max'});
    S.plot4 = get(S.sl4,{'min','value','max'});
    S.plot5 = get(S.sl5,{'min','value','max'});
    S.plot6 = get(S.sl6,{'min','value','max'});
    S.plot7 = get(S.sl7,{'min','value','max'});
    S.plot8 = get(S.sl8,{'min','value','max'});
    S.plot9 = get(S.sl9,{'min','value','max'});
    S.plot10 = get(S.sl10,{'min','value','max'});

    % P = 1 if forward   P = 2 if backward
    P = get(S.pp,'value');     %P2 = i
    P2 = get(S.pp2,'value');      i = P2;
list = dir('*.txt'); n = length(list);

%import the voltage values and the I(V) and dI/dV readings
iv = importdata(list(2*i).name); aux = importdata(list(2*i-1).name);

%Save the variables in vectors
v = (iv(:,1)); I = (iv(:,2))*1e9; didv = (aux(:,2));

%All of our STS data are collected by varying the applied Bias voltage from
%negative to positive and from positive to negative.
%Separate the two sets of vectors into both forward (from negative bias
%to positive bias).

%When Bias Voltage varies from negative to positive, then positive to
%negative
```

```
if v(1)<0
   length_halving = length(didv)/2;
   I_forward = I(1:length_halving);
   I_backward = I(2*length_halving:-1:length_halving+1);

   didv_forward = didv(1:length_halving);
   didv_backward = didv(2*length_halving:-1:length_halving+1);

   v_forward = v(1:length_halving);
   v_backward = v(2*length_halving:-1:length_halving+1);
%When Bias Voltage varies from positive to negative, then negative to
%positive
else
   length_halving = length(didv)/2;
   I_forward = I(length_halving:-1:1);
   I_backward = I(length_halving+1:2*length_halving);

   didv_forward = didv(length_halving:-1:1);
   didv_backward = didv(length_halving+1:2*length_halving);

   v_forward = v(length_halving:-1:1);
   v_backward = v(length_halving+1:2*length_halving);
end


%Separate the vectors into forward and backward
length_halving = length(didv)/2; I_forward = I(1:length_halving);
I_backward = I(length_halving+1:2*length_halving);

didv_forward = didv(1:length_halving);
didv_backward = didv(length_halving+1:length_halving*2);

v_forward = v(1:length_halving);
v_backward = v(length_halving+1:2*length_halving);


if v_forward(1) >0
   temp = v_backward;     v_backward = v_forward;     v_forward = temp;
   temp2 = didv_backward;     didv_backward = didv_forward;     didv_forward = temp2;
   temp3 = I_backward;     I_backward = I_forward;     I_forward = temp3;
end

if P == 2
   I_forward = I_backward;     v_forward = v_backward;
   didv_forward = didv_backward;
end
```

```
plot(S.ax2,v_forward,I_forward);

datacursormode on
v_noise_min = S.plot5{2}; v_noise_max = S.plot6{2};
x_phys_noise = []; y_val1_noise = [];
% Search for the points that correspond to this range
for i = 1: length(v_forward)
   if(v_forward(i) >= v_noise_min && v_forward(i) <= v_noise_max )
      x_phys_noise = [x_phys_noise, v_forward(i)];
      y_val1_noise = [y_val1_noise, I_forward(i)];
   end
end
% Find the average offset.
offset = sum(y_val1_noise) / length(y_val1_noise);
I_forward = I_forward - offset;

% Evaluate the standard deviation of the I(V) values. Delete points that
% are within two stnadard deviation. Replace them with 0.
y_val1_noise = y_val1_noise - offset;
sum_standard_deviation = 0;
for i = 1:length(y_val1_noise)
   sum_standard_deviation = sum_standard_deviation + y_val1_noise(i)^2;
end
standard_deviation = sqrt(sum_standard_deviation / length(y_val1_noise) );
for i = 1:length(I_forward)
   if(abs(I_forward(i))<= standard_deviation)
      I_forward(i) = 0;
   end
end

% Find the first and last recurrance of zero, and delete all points
% inbetween by replacing them into zero.
for i = 1:length(I_forward)
   if(I_forward(i) == 0)
      x_min_pts_delete = i;
      break;
   end
end
for i = length(I_forward):-1:1
   if(I_forward(i) == 0)
      x_max_pts_delete = i;
      break;
   end
end
```

```
for i = x_min_pts_delete:x_max_pts_delete
   I_forward(i) = 0;
end

% Now we want to take in account of the broadening effect. Following the
% equation from Vaishno's thesis at page 34, convolution is conducted.

% Inpute the delta_z value from the user.
delta_V = S.plot1{2}; min_v = S.plot3{2}; max_v=S.plot4{2}; dv=S.plot2{2};

% Give a range for voltage that will be used in the convolution.
v_convolution = min_v:dv: max_v; IoverV_normalized = [];

% Compute the convolution with the given paramters inputted by the user.
for j = 1:length(v_convolution)

   summation = 0;
   for i = 1: length(v_forward)
      summation = summation + (I_forward(i)/v_forward(i))*exp(-1*abs(v_forward(i)-
v_convolution(j))/delta_V)*dv;
   end
   summation = summation / (2*delta_V);

   IoverV_normalized = [IoverV_normalized, summation];
end

IoverV_normalized = IoverV_normalized/(0.1*(max(IoverV_normalized)-
min(IoverV_normalized)));

useful_v = [];
useful_i = [];

for i=1:length(v_forward)
   for j = 1:length(v_convolution)-1
      if v_convolution(j) <=v_forward(i) && v_convolution(j+1) > v_forward(i)
         useful_v = [useful_v; v_convolution(j)];
         useful_i = [useful_i; IoverV_normalized(j)];
      end
   end
end

normalized_forward = didv_forward./useful_i;

x= useful_v;
y= normalized_forward;
%%%%%%%%%%%%%%%%%%%%%%%%%%%%%%%%%%%%%%%%%%%%%%%%%%%%%%%%%%%%%%%%%%%%%%%%%%%%
```

```
i = P2;
list_temp = dir;
check = 0;
for k=1:length(list_temp)
    if strcmp('results',list_temp(k,1).name)
        check = check + 1;
    else
        check = check+ 0;
    end
end
if check == 0
    mkdir('results');
end
cd results;

if P == 1
    n = length(list(2*i).name);
    fid = fopen([list(2*i).name(1:n-16), '_normalized_forward.txt'],'w+');
    for k = 1:length(x)
        fprintf(fid, '%6.4f     %6.4f\n', x(k), y(k));
    end
    fclose(fid);

    string_confirm = [list(2*i).name(1:n-16), '_normalized_forward : Saved!'];
    set(S.text25, 'string' , string_confirm);

else
      n = length(list(2*i).name);
    fid = fopen([list(2*i).name(1:n-16), '_normalized_backward.txt'],'w+');
    for k = 1:length(x)
        fprintf(fid, '%6.4f     %6.4f\n', x(k), y(k));
    end
    fclose(fid);

    string_confirm = [list(2*i).name(1:n-16), '_normalized_backward : Saved!'];
    set(S.text25, 'string' , string_confirm);

end

cd ..

end
```

Appendix B

Quantum Dot Size Analysis

Here, we present the procedures for quantifying the sizes of QDs from plan-view STM images. Particle and Pore Analysis module in Scanning Probe Image Processor (SPIP) was used to perform the analyses. The "Advanced Threshold" detection method was used for QD identification. The root mean square of the height values within the image was calculated, and any region above 5 times the root mean square from the background level was considered as QDs. The average diameter and height of identified QDs were exported from the software. The average diameters and heights of InGaN QDs from Chapter 4 were obtained by this method.[5]

In Chapter 5, a composition profile is interpolated from a XSTM image of GaSb/GaAs QD into the continuum model. The composition profile was extrapolated by the following procedures: Fig. 5.5(a) shows a XSTM image with a 1.23 nm tip height color range. The bright and dark regions of the XSTM image correspond to GaSb and GaAs, respectively. In Fig. 5.1(b), pixels with tip height up to 4.9 ± 0.5 Å above the GaAs background are displayed in a grayscale format, with the brighter and darker shades of gray corresponding to lower and higher tip heights, respectively. Pixels with tip heights from the GaAs background (brightest) to 4.9 ± 0.5 Å above the GaAs background (darkest) are

normalized and attributed to x_{Sb} ranging from 0 to 1. Any regions with pixels height of 4.9 ± 0.5 Å above the GaAs background were considered GaSb.[5]

Appendix C

Materials Parameters

This appendix lists a variety of materials parameters used in this dissertation. Table C.1 lists the material parameters of the GaAs and GaSb used in Chapters 5 of this dissertation.[7-12] Table C.2 lists the material parameters used for the RADS simulation.[13] Table C.3 lists the material parameters used for STS analysis.

Material	Symbol	GaSb	GaAs
Electron Effective Mass[7]	m_e/m_o^*	0.041	0.067
Hole Effective Mass[8]	m_h/m_o^*	0.40	0.47
Bandgap (eV)[9]	E_g	0.770	1.43
Valence Band Offset (eV)[8]	ΔE_v	--0.67--	
Deformation Potential Constants (eV) [10]	a_c	-7.5	7.17
	a_v	-0.8	-1.16
Lattice Constant (Å)[11]	a_{lc}	6.0959	5.65325
Young's Modulus (GPa)[12]	E	63.1	85.9

$$\boldsymbol{m_o^* = 9.11 * 10^{-31} kg}$$

Table C.1: Material parameters of the GaAs and GaSb used for the computational work in Chapter 5.

Material	Unit cell length a (Å)		Unit cell length c (Å)	Poisson's ratio, ν	Density (g/cm^3)
GaAs	5.654		5.654	0.312	5.316
InAs	6.058		6.058	0.352	5.66
GaN (hexagonal)	3.189		5.185	0.203	6.081
InN (hexagonal)	3.55		5.76	0.32	6.88
GaSb	6.0954		6.0954	0.313	5.619
GaN (cubic)	4.52		4.52	0.342	6.691

Table C.2: Material parameters of the Semiconductor compounds used in RADS.[13]

Material	Band Gap (eV)	Unit cell length a (Å)	Unit cell length c (Å)
GaAs	1.43	5.654	5.654
GaSb	0.68	6.0954	6.0954
InAs	0.36	6.058	6.058
GaN (Wurtzite)	4.3	3.189	5.185
InN (Wurtzite)	0.66	3.55	5.76

Table C.3: Material parameters of the Semiconductor compounds used for STS analysis.[13-16]

Appendix D

Rocking Curve Analysis by Dynamical Simulation

Rocking curve analysis by dyanamic simulation (RADS) is a tool that simulates and analyzes high-resolution X-ray diffraction (HRXRD) data of epitaxial films grown on single crystal substrates. The simulation is based on dynamic diffraction theory, which assumes that the diffraction intensity is proportional to the magnitude of the structure factor.[13] In this section, the procedures are described for performing RADS and analyzing the strain and composition of the results.

The nominal values of the thickness and composition of semiconductor heterostructure layers are input into RADS. Ternary, quarternary, or quinternary semiconductor alloys are incorporated into the materials database using Vegard's law. An older version of the RADS software are accessible near the BEDE HRXRD at the University of Michigan. However, the software is capable of simulating XRD spetrums of cubic crystal systems. A trial version of a newer version of RADS from Jordan Valley was acquired, which had the capability to simulate XRD spectrums of Wurtzite crystal system. The older and the newer versions of the RADS uses the same dynamic diffraction theory. RADS simulations for the InGaAs(Sb)N/GaAs QW heterostructures were performed on the older version of the software, while the simulations for the InGaN/GaN QD heterostructures was performed on the trial version by Jordan Valley.

A RADS simulation is performed, and the resulting XRD simulation is compared to the HRXRD data. In order to align the simulated XRD peaks to those of HRXRD peaks, composition of individual layers is varied. Furthermore, graded composition within the layers introduced to find a better match between simulation and data for the cases of QD systems. The linearly graded composition was added by entering ZR(ramp,x_{start},x_{end}) into the composition input field, where x_{start} and x_{end} are the starting and ending composition at the bottom and top of the layer, respectively. An increase in lattice parameter due to composition changes lead to a shift resulting in a larger ω or 2θ. The composition of individual layers is varied until a good agreement between the simulation data is found. In addition, the thickness of each layers is varied to find a better match.

The strain in the epilayers is calculated using the software Peak Split. The wavelength of the X-ray, monochromator reflection plane, substrate reflection plane, composition of epilayer, and the peak separation between the substrate and the epilayer peaks are inputted into the software. Using Bragg's equation, $n\lambda = 2d\sin(\theta_B)$, and allowed crystallographic indicies of different crystal structures, the the mismatch strain between two crystal structures, $\varepsilon = (a_s - a_f)/a_f$ is calculated.

Furthermore, the HRXRD data revealed sharp peaks for the InGaN QDs grown on GaN/sapphire substrates at $\Delta\theta = 0.70°$. It was suggested that an AlGaN layer was in between the GaN and sapphire substrates, and the composition of the AlGaN layer was estimated by the following procedure. The lattice constants of GaN and AlN were given as GaN(a) = 3.189 Å, GaN(c) = 5.186 Å, AlN(a) = 3.11 Å, AlN(c) = 4.98 Å. During the HRXRD measurements, the GaN (002) peak was centered on $\omega = 17.48^o$. Since the angular

separation between the GaN (002) substrate and the unknown peaks was 0.7^{o}, degrees), the Bragg's angle was calculated to be

$2\theta+\Delta\theta = 35^{o} + 0.7^{o} = 35.7^{o}$. $\theta = 35.7/2 = 17.85^{o}$.

The Bragg's equation, $\lambda = 2\ d\ \sin(17.85^{o})$ was set up. The source of the X-ray is a CuK (α^{1}), which has a wavelength of 0.154 nm; thus, $d = 0.154\text{ nm} / (2\sin(17.85^{o})) = 0.251$ nm. The d spacing for hexagonal crystal structures are given as

$d^{-2} = (4/3)(h^2 + hk + k^2)/a^2 + l^2/c^2$.

Since h=0 and k=0, l=2, $(0.251\text{ nm})^{-2} = 0 + 2^2/c^2$. Thus, c = 0.502 nm. Using the lattice constants of GaN and AlN with Vegard's law, x c(AlN) + (1-x) c(GaN) = 0.502, which solves as x= 0.8. Thus, an $Al_{0.8}Ga_{0.2}N$ layer was suggested to be present in between the GaN and sapphire substrates.

Appendix E

Materials Database for Poisson-Shrodinger Calculations

To predict the wavefunctions of fully or partially ionized electron and holes at Type I and Type II band alignments, a 1D Poisson-Shrodinger calculation is performed via a free-ware program written by G. Snider at University of Nitre Dame.[17-19] Below are the material database used in the program.

	GaSb	GaAs	InAs
Energy gap (eV)	+0.726E+00	+0.142E+01	+3.720E-01
Band offset	+0.200E+00	+0.000E+00	-6.490E-01
Rel. dielectric constant	+0.157E+02	+0.131E+02	+1.450E+01
electron effective mass	+0.41E-01	+0.670E-01	+2.300E-02
conduction band valley degeneracy	+0.100E+01	+0.100E+01	+1.000E+00
heavy hole effective mass	+0.4E+00	+0.480E+00	+4.000E-01
light hole effective mass	+0.41E-01	+0.820E-01	+8.000E-02
donor ionization energy	+0.100E-03	+0.600E-02	+1.500E+00
acceptor ionization	+0.100E-01	+0.300E-01	+5.000E-02
deep donor ionization	+0.600E+00	+0.600E+00	+5.000E-02
deep acceptor ionization	+0.700E+00	+0.700E+00	+1.000E-01
donor concentration	+0.000E+00	+0.000E+00	+0.000E+00
acceptor concentration	+0.000E+00	+0.000E+00	+0.000E+00
deep donor concentration	+0.000E+00	+0.000E+00	+0.000E+00

deep acceptor concentration	+0.000E+00	+0.000E+00	+0.000E+00
electron mobility	+0.850E+04	+0.850E+04	+1.000E+04
hole mobility	+0.400E+03	+0.400E+03	+5.000E+02
electron lifetime	+0.100E-11	+0.100E-11	+1.000E-10
hole lifetime	+0.100E-11	+0.100E-11	+1.000E-10
polarization	+0.000E+00	+0.000E+00	+0.000E+00

Table E.1: Material parameters of GaAs, GaSb, and InAs used for the 1D Poisson-Shrodinger calculation.

For Type I band alignment, an input code as following was used:

```
# A single quantum well.  Quantized states are found automatically.
surface slope=0          v1
InAs    t=100   x=0.5   Nd=1e18
InAs_GaAs     t=100   x=0.5   Nd=1e18
GaAs   t=100   x=0.5   Nd=1e18
substrate
fullyionized
#v1 0.0 -1.0 -0.5
v1 0.0
schrodingerstart=-1000
schrodingerstop=3000
temp=300K
dy=10
```

For Type II band alignment, an input code as following was used:

```
# A single quantum well.  Quantized states are found automatically.
surface slope=0          v1
GaSb_GaAs    t=100   Na=1e19
GaAs   t=100   Nd=1e17
GaSb_GaAs    t=100   Na=1e19
substrate
fullyionized
#v1 0.0 -1.0 -0.5
v1 0.0
schrodingerstart=-1000
schrodingerstop=3000
temp=300K
dy=10
```

Appendix F

List of Samples

This appendix summarizes the samples discussed in this dissertation. Three groups of samples were examined using characterization tools described in Chapter 2. A summary of (1) InGaAs(Sb)N/GaAs quantum well, (2) InGaN/GaN quantum dot, and (3) GaSB/GaAs quantum dot heterostructures are presented.

Sample #	In/(In+ Ga)	DMHy/ TBAs	Sb/(Sb+As)	Substrate	Annealed	$T_{substrate}$ (^{o}C)	$P_{reactor}$ (Torr)
TS2012 0313-23	0.0205	7.51	-	p^{+} GaAs (001)	No	525	100
TS2012 0306-16	0.0067	15.32	0.0886	p^{+} GaAs (001)	No	525	150
TS2012 0312-12	0.0067	15.32	0.0886	p^{+} GaAs (001)	Yes	525	150

Table F.1: InGaAs(Sb)N /GaAs quantum well samples

Sample	Substrate	Size	Polish #	Date	Experimental Result
N1979	Sumitomo	2mmx10mm	1	4/6/2013	Layers found, STS
F310	Ammono	2mmx10mm	1	1/13/2014	Layers found
F310	Ammono	2mmx10mm	2	1/20/2014	Cleaved at jaws
F310	Ammono	2mmx9mm	3	3/20/2014	Cleaved at jaws
F310	Ammono	2mmx10mm	4	4/102014	No Layers found
F310	Ammono	2mmx10mm	5	4/14/2014	No Layers found
F310	Ammono	2mmx10mm	6	4/20/2014	No Layers found
F310	Ammono	2mmx5mm	7	5/14/2014	No Layers found
F402	Ammono	2mmx10mm	2	7/18/2014	No Layers found
F402	Ammono	2mmx10mm	3	8/6/2014	Cleaved at jaws
F402	Ammono	2mmx10mm	4	11/21/2014	No Layers found
F520	Ammono	2mmx10mm	1	12/18/2014	Cleaved at jaws
F520	Ammono	2mmx10mm	2	12/20/2014	Cleaved at jaws
F520	Ammono	2mmx9mm	3	1/15/2015	Cleaved at jaws
F520	Ammono	2mmx9mm	4	1/27/2015	Cleaved at jaws
F520	Ammono	2mmx8mm	5	1/31/2015	No Layers found
F520	Ammono	2mmx9mm	6	2/10/2015	Cleaved at jaws
F561	Ammono	2mmx10mm	1	3/30/2015	No Layers found
F561	Ammono	2mmx8mm	2	4/4/2015	Cleaved at jaws
F561	Ammono	2mmx8mm	3	4/5/2015	Cleaved at jaws
F561	Ammono	2mmx10mm	4	4/6/2015	Cleaved at jaws
F561	Ammono	2mmx10mm	5	4/7/2015	cleaved at jaws

Table F.2: InGaN /GaN quantum dot XSTM sample cleavage history.

	substrate	Ga flux (Torr)	In flux (Torr)	$T_{substrate}$	N_2 flow rate (sccm)	plasma power	# of QD layer
F624	Free-standing GaN	4E-8	9E-8	540 °C	1.33	420 W	1
F629	GaN/AlN/ sapphire	4E-8	9E-8	540 °C	1.33	420 W	1
F630	GaN/AlN/ sapphire	4E-8	9E-8	540 °C	1.33	420 W	3

Table F.3: InGaN /GaN quantum dot plan-view STM samples.

	Surface grown on	III/V ratio	Growth rate	$T_{substrate}$	Sb deposition	QDs formed?
As-terminated	GaAs (2X4)	2	0.3 μm/ h	460 °C	1 ML	Yes
Sb-terminated	GaAs (2X8)	2	0.3 μm/ h	460 °C	2 ML	Yes
SK	GaAs (2X4)	1	0.3 ML/ s	500 °C	1~4 ML	No
IMF	GaAs (2X4)	10	0.3 ML/ s	500 °C	1~4 ML	Yes

Table F.4: GaSb/GaAs quantum dot XSTM samples.

References

[1]B. Lita, Ph.D. Thesis, University of Michigan, 2002.

[2]M. Reason, Ph.D. Thesis, University of Michigan, 2006.

[3]R. M Feenstra, *Phys. Rev. B* **50**, 4561 (1994).

[4]P. Martensson and R. M. Feenstra, *Phys. Rev. B* **39**, 7744 (1989).

[5]S. Huang, Ph.D. Thesis, University of Michigan, 2015.

[6]V. D. Dasika, R.S. Goldman, J.D. Song, W.J. Choi, I.K. Han, J.I. Lee, J. Appl. Phys. **106**, 14315 (2009). [6]B. Shin, B. Lita, R. S. Goldman, J. D. Phillips, and P. K. Bhattacharya, applied Physics Letters **81**, 1423 (2002).

[7] F. J. Blatt, Modern physics. (McGraw-Hill Book Company, Incorporated, 1992).

[8] N. Ledentsov, J. Bohrer, M. Beer, F. Heinrichsdorff, M. Grundmann, D. Bimberg, S. Ivanova, B. Meltser, S. Shaposhnikov, I. Yassievich, N. Faleev, P. Kop'ev, Z. Alferov, *Phys. Rev. B* **52**, 14058 (1995).

[9]C. Kittel, Introduction to Solid State Physics, 6th ed. (John Wiley & Sons, Inc., New York, 1986).

[10]E. T. Yu, J. O. McCaldin and T. C. McGill, *Solid State Phys.* **46**, 1 (1992).

[11]I. Vurgaftman, J. R. Meyer and L. R. Ram-Mohan, *J. of Appl. Phys.* **89**, 5815-5875 (2001).

[12]S. Adachi, Physical Properties of III-V Semiconductor Compounds, *Wiley-VCH Verlag GmbH & Co. KGaA*, 17-47 (2005).

[13]Rocking Curve Analysis by Dynamical Simulation, *Bede Scientific, Inc*.

[14]Semiconductor Band Gaps, retrieved from http://hyperphysics.phy-astr.gsu.edu/hbase/tables/semgap.html.

[15]Semiconductors on NSM, retrieved from http://www.ioffe.ru/SVA/NSM/Semicond/.

[16]Y. –R. Lyu and T. –E. Hsieh, *ECS J. of Sol. State Sci. and Technol.* **3**, R258 (2014).

[17]G. L. Snider, I. -H. Tan, and E. L. Hu, *J. of Applied Physics* **68**, 2849 (1990).

[18]I. -H. Tan, G. L. Snider, and E. L. Hu, *J. of Applied Physics* **68**, 4071 (1990).

[19]1D Poission- Schrödinger solver [Computer software], retrieved from http://www3.nd.edu/~gsnider/, (2011).